AD-A144 197 DESIGN STUDY OF ION ANTI-CONTAMINATION SYSTEM(U) UTAH 1/2
STATE UNIV LOGAN SPACE DYNAMICS LABS W K WONG
07 MAR 84 SDL/84-014 AFGL-TR-84-0086 F19628-83-C-0056
UNCLASSIFIED F/G 20/6 NL

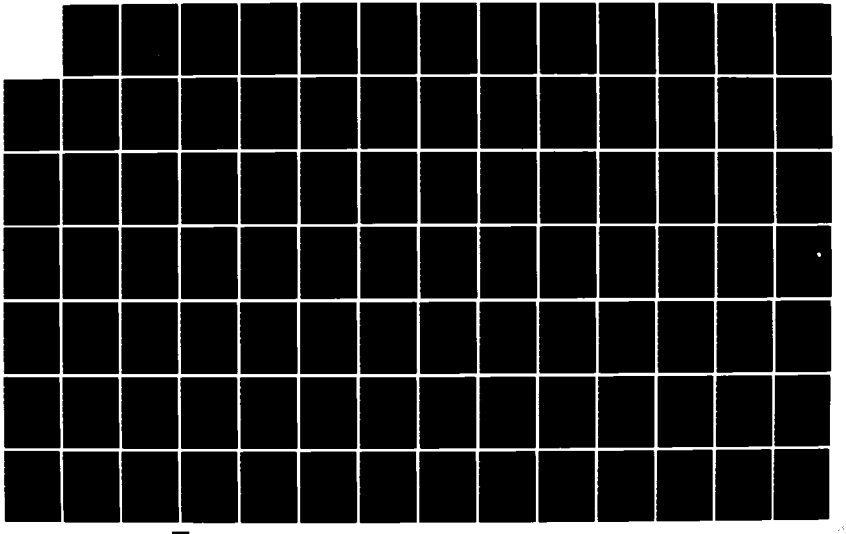

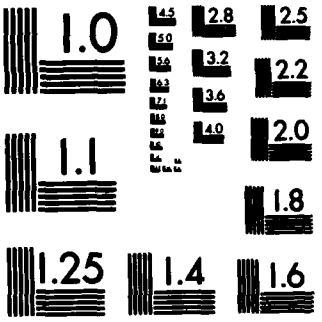

(12)

AFGL-TR-84-0086

DESIGN STUDY OF ION ANTI-CONTAMINATION SYSTEM

W. K. Wong

Space Dynamics Laboratories
Utah State University
Logan, UT 84322

Scientific Report No. 2

7 March 1984

Approved for Public Release; Distribution Unlimited

AIR FORCE GEOPHYSICS LABORATORY,
AIR FORCE SYSTEMS COMMAND
UNITED STATES AIR FORCE
HANSCOM AIR FORCE BASE
MASSACHUSETTS 01731

This report has been reviewed by the ESD Public Affairs Office (PA) and is releasable to the National Technical Information Service (NTIS).

This technical report has been reviewed and is approved for publication

FRANCIS X. ROBERT
Contract Manager

RANDALL E. MURPHY
Branch Chief

FOR THE COMMANDER

RANDALL E. MURPHY
Acting Director
Infrared Technology Division

Qualified requestors may obtain additional copies from the Defense Technical Information Center. All others should apply to the National Technical Information Service.

If your address has changed, or if you wish to be removed from the mailing list, or if the addressee is no longer employed by your organization, please notify AFGL/DAA Hanscom AFB, MA 01731. This will assist us in maintaining a current mailing list.

Do not return copies of this report unless contractual obligations or notices on a specific document requires that it be returned.

413923

Unclassified

SECURITY CLASSIFICATION OF THIS PAGE

REPORT DOCUMENTATION PAGE

1a. REPORT SECURITY CLASSIFICATION: Unclassified	1b. RESTRICTIVE MARKINGS: None
2a. SECURITY CLASSIFICATION AUTHORITY	3. DISTRIBUTION/AVAILABILITY OF REPORT: Approved for Public Release; Distribution Unlimited
2b. DECLASSIFICATION/DOWNGRADING SCHEDULE	
4. PERFORMING ORGANIZATION REPORT NUMBER(S): SDL/84-014	5. MONITORING ORGANIZATION REPORT NUMBER(S): AFGL-TR-84-0086
6a. NAME OF PERFORMING ORGANIZATION: SSG, Inc. / 6b. OFFICE SYMBOL (If applicable):	7a. NAME OF MONITORING ORGANIZATION: Contract and Grant Office, Utah State University
6c. ADDRESS (City, State and ZIP Code): 150 Bear Hill Road, Waltham MA 02154	7b. ADDRESS (City, State and ZIP Code): UMC 41, Logan UT 84322
8a. NAME OF FUNDING/SPONSORING ORGANIZATION: Air Force Geophysics Lab / 8b. OFFICE SYMBOL (If applicable): LSP	9. PROCUREMENT INSTRUMENT IDENTIFICATION NUMBER: F19628-83-C-0056
8c. ADDRESS (City, State and ZIP Code): Hanscom AFB, MA 01731, Monitor/Francis X. Robert	10. SOURCE OF FUNDING NOS. — PROGRAM ELEMENT NO.: 62101F; PROJECT NO.: 7670; TASK NO.: 10; WORK UNIT NO.: AK
11. TITLE (Include Security Classification): Design Study of Ion Anti-Contamination (ovr)	
12. PERSONAL AUTHOR(S): Wong, W. K.	
13a. TYPE OF REPORT: Scientific No. 2 / 13b. TIME COVERED: FROM 7/1/83 TO 11/30/83	14. DATE OF REPORT (Yr., Mo., Day): 1984 March 7 / 15. PAGE COUNT: 113
16. SUPPLEMENTARY NOTATION: The work reported herein was perfromed under subcontract 84-001 to Space Dynamics Laboratories, Utah State University.	
17. COSATI CODES — FIELD / GROUP / SUB. GR.	18. SUBJECT TERMS (Continue on reverse if necessary and identify by block number): Infrared sensors; Oxygen cryodeposit

19. ABSTRACT (Continue on reverse if necessary and identify by block number)

Cryogenically-cooled, high straylight rejection, infrared sensors are currently planned for use in space surveillance applications. An investigative study was made to determine the optical contamination problem of these sensor(s) during a four-year mission duration and the feasibility of designing an anti-contamination system that can be adapted to these sensor(s). The optical contamination problem is the increase in optical scatter of the telescope primary mirror due to cryodeposits of atomic oxygen (external) and water vapor (self-generated), and particulate contamination (self-generated). At sensor altitude of 1,000 Km the atomic oxygen cryodeposit on the mirror, accumulated over four years of mission life, may be a factor of 100 higher than what is considered manageable. Therefore, the required transmission efficiency of an IACS is approximately one percent. (Continued on reverse.)

20. DISTRIBUTION/AVAILABILITY OF ABSTRACT: UNCLASSIFIED/UNLIMITED ☒ SAME AS RPT. ☐ OTIC USERS ☐	21. ABSTRACT SECURITY CLASSIFICATION: Unclassified
22a. NAME OF RESPONSIBLE INDIVIDUAL: Francis X. Robert, Contract Monitor	22b. TELEPHONE NUMBER (Include Area Code): 617.861-3630 / 22c. OFFICE SYMBOL: LSP

DD FORM 1473, 83 APR — EDITION OF 1 JAN 73 IS OBSOLETE.

SECURITY CLASSIFICATION OF THIS PAGE

11. System (UNCLASSIFIED)

19. The theory and commercial designs of ion pumps was examined and these principles were applied to the conceptual design of ion anti-contamination devides. A number of device configurations were presented and analyzed. Their applicability to this contamination problem is reported.

FOREWORD

This report is prepared by SSG, Inc., at Waltham, Massachusetts, for work performed under USU Subcontract No. 084-001, which was funded under prime funding from DOD/USAF/AFGL Contract No. F19628-83-C-0056.

Technical direction of this program was given by Lt. Robert Kline of the USAF, Space Technology Center at Albuquerque, New Mexico. The technical monitor of this subcontract is Dr. Doran J. Baker of Utah State University. The principal investigator at SSG was W. K. Wong. The experimental plan for measuring IR radiation was developed jointly between SSG and PSI. Visidyne provided some assistance in the analysis of the ion pumping physics.

The work presented here was performed between July and November of 1983.

TABLE OF CONTENTS

Section			Page
1.0	EXECUTIVE SUMMARY		1
	1.1	Introduction and Summary	1
	1.2	Summary of Remaining Sections	3
2.0	DEFINITION OF THE OPTICAL CONTAMINATION PROBLEM		7
	2.1	Scope of the Contamination Problem Being Addressed	7
	2.2	Evidence for Problem of Mirror Contamination	8
	2.3	Optical Parameter Impacts	8
	2.4	Figure of Merit for Optical Contamination	8
	2.5	Contamination Due to Particulate Sources	11
	2.5.1	Particulate Contamination on Clean Bench	11
	2.5.2	Polydispersed Particle-Scattering Data Agrees with Mie Scatter Theory	13
	2.5.3	Monodispersed Particle Scattering at 10.6 um	17
	2.5.4	Sensor OFVR Data Before and After Particulate Contamination	17
	2.5.5	Mechanism of Particulate Contamination of Mirrors	21
	2.6	Contamination Effects Due to Gaseous Cryodeposits	22
	2.6.2	Sensor Gaseous Contamination Problem	27
	2.6.2.1	Cryopumping of Ambient Species	27
	2.6.2.2	Spacecraft Generated Gaseous Contamination	37
	2.7	Summary of Containment Environment	41

3.0 IACS DESIGN ISSUES AND CANDIDATE CONFIGURATIONS 45

3.1 Ion Pumping Mechanisms 45
3.2 Effectiveness of Ion Pumping in the Optical Path 49
3.3 Interaction Length and Forebaffle Conductance 51
3.4 IACS Candidate Configurations 51
3.4.1 Circular Aperture Pump (Config. 1) 57
3.4.2 Rectangular Aperture Pump (Config. 2) 60
3.4.3 Circular Aperture Peripheral Pump (Config. 3) 66
3.4.4 RF Ion Getter Pump (Config. 4) 71
3.4.5 Particulate Pump (Config. 5) 76
3.5 Magnetic Field 78
3.6 High Voltage Engineering Considerations 83

4.0 EFFECTIVENESS EXPERIMENT CONCEPTUAL DESIGN 86

5.0 IR RADIATION ANALYSIS 90

6.0 EXPERIMENTAL PLAN FOR MEASURING IR RADIATION LEVEL 100

APPENDIX A: Key Theory and Development of Ion Pump 104

REFERENCES 108

1.0 EXECUTIVE SUMMARY

1.1 Introduction and Summary

Cryogenically-cooled, high straylight rejection, infrared sensors are currently planned for use in space surveillance and earth limb emission measurements for a multi-year mission. Initial laboratory data indicated that cryodepost thickness of the order of 2 to 5 microns are sufficient to degrade mirror performance to below acceptable levels. A search of the literature and our experience with cryogenic sensors indicated that the major sources of contamination (either atmospheric constituent species or spacecraft outgassing) have to flow through the telescope entrance aperture.

The concept of an ion anti-contamination system (IACS) is based on generation of an electron plasma within a telescope baffle to ionize the incoming contaminant gas molecules through electron impact and uses a static electric field to direct the resultant ions to a collector. The ideal IACS is a low-power device with no moving parts so that is has inherently long operating life. It should be operated without significant interference with the sensor or thermal loads on the cryogenics. It should have attenuation levels of at least 10^{-2} to 10^{-4}.

The contamination environment for a cryogenic infrared sensor is significantly dependent on its operating orbital altitude, two candidate altitudes (600 and 5600 nautical miles) are emphasized for evaluation.

The primary concern of sensor contamination is the ability to keep the cryogenic optical elements clean so that the mirror BRDF can be maintained. The BRDF can be degraded by particulate deposition or gaseous cryodeposition.

A micrometeroid impact would provide enough energy to dislodge existing or to generate new particulate contaminant from a spacecraft surface. The dislodged particles have very low initial velocities. Typical values are 40 cm/sec for 5 to 15 um size range and 3 cm/sec for 95 - 105 um size range.

A conceptual design (Configuration 5) to protect the primary mirror from these dislodged particles has been obtained. This configuration can be readily integrated into a CIRRIS - class telescope design. The particulates will be ionized by electron bombardment and then deflected and deposited at the collector plate by electrostatic field. A point design that measures 12 inches in diameter and 20 inches long can protect a 10 inch diameter circular aperture. The power consumption for the election cloud generation is 15 watts at 10^{-7} torr of pressure. The magnetic field generation requires 45 watts for a 36 pound solenoid weight.

The atmospheric and spacecraft outgassing gaseous species have much smaller ionization cross sections in comparison with particulates. Therefore, effective ionization of these contaminents would require much higher electron density which can be generated with much higher applied voltages.

Four IACS configurations were considered for the gaseous species pumping. Configuration 1 is basically the particulate pump described above scaled up to the required electron densities. Parameters for a point design for protection of an 8 inch circular aperture include applied voltage of 700 KV, solenoid weight of 220 pounds and solenoid power consumption of 100 watts. Configuration 2 is a novel pumping arrangement designed for a rectangular optical aperture of length over width ratio of 5. It may provide the required electron density without the very high voltages. More detailed electric field calculations are required to further evaluate this concept. Configuration 3 is a peripheral pump which does not require very high voltages but only be effective against gas contaminants that impinge on the wall of this device. Configuration 4 uses no magnet. It relies on a transversely excited RF electric field to

elongate the path length of the injected electrons to reduce the electronic current. However, a preliminary point design for a 15 cm by 50 cm rectangular optical aperture and an interaction length of 50 cm requires ~8 KW of power to operate. The weight of this configuration will be less than 20 pounds.

In summary, a conceptual IACS design to protect the orbital sensor from an orbit particulate is obtained. This device appears to be compatible with the baffle design of a CIRRIS - class high straylight rejection telescope. Additional effort should be directed at bringing this concept into sensor application.

The problem of gaseous species pumping is more difficult due to the much smaller ionization cross section. A straight forward scaling from commercial ion pump single cell dimension of ~1 inch to 10 to 40 inches require voltage in the order of a million volt. The novel split anode pumping configurations is a promising approach if the electrons can indeed be generated and trapped within the optical aperture. More detailed field calculation are required to evaluate fully its applicability. The peripheral pumping configuration can be built with modest voltage and weight, but its applicability may have to be compared with a simple alternative, as a cryobaffle at 20 Kelvin. The RF Getter pump is very light weight but power hungry. If the shape of the optical aperture is a large length to width ratio rectangle, then its power requirement will be reduced and this approach will become more attractive.

1.2 Summary of Remaining Sections

Section Two defined the optical contaminant problem the IACS will be designed to solve. The figure of merit for optical contamination is the BRDF of the mirror. Experimental measurements on BRDF of low-scatter mirror samples indicate that particulate deposition on cryogenic mirrors, in addition to molecular cryodeposits are dominant sources of BRDF degradation. The experimental data from various sources are referenced to illustrate the above statement. The contaminant environment and

contamination mechanisms are summarized at the end of this section for the prelaunch, launching and on-orbit sensor environments.

Section Three covers the theoretical analysis of an ion anti-contamination system (IACS). It includes the parameters that affect the attenuation efficiency of an IACS. For example, increasing the interaction length by two would square the attenuation efficiency (i.e., 10% becomes 1%). Placing a forebaffle section of length over diameter equal to two between the IACS interaction region and the external atmosphere can reduce the gas flow rate from 100% to 36%.

Five ion pump configurations were considered. The first IACS configuration is a scaled-up version of a single cell Penning cell with modified cathodes. This configuration is ideal for circular optical aperture of small dimensions because the operating voltage scales up to 700 KV for a point design of 20 cm optical diameter. The power consumption of the discharge is less than 1 watt at 10^{-7} torr of external pressure. The required magnetic flux density (~250 Gauss) can be generated by a solenoid that wraps around the electrodes. Operating at 100 Kelvin, a solenoid of 25 cm diameter and 100 cm length weighs 220 lbs. and dissipates 100 watts in Joule heating. If the solenoid winding temperature can be reduced to below 30 Kelvin, a superconducting magnet is possible. This would increase the complexity of the IACS system but it would permit the maintenance of greater magnetic flux densities while essentially requiring no electric power input. Flux densities of 50,000 Gauss are routinely achieved in superconducting solenoids. This 20 cm optical diameter point design has an attenuation efficiency of 10^{-2} for gas kinetic temperature of 450 Kelvin. Parameters for a point design for a 40 inch optical diameter are also presented.

The second IACS configuration is a novel pumping arrangement which may provide the required electron density without the very high voltages. This arrangement is suitable for a rectangular aperture. Essentially, one has taken the standard ion pump single cell configuration and cut the pump into two halves such that each half-pump has a cylindrical

anode and a cathode. A number of these half-pumps are stacked side-by-side to form a closely packed array . Two arrays are placed one above and one below the rectangular optical aperture along the baffle such that each half-pump will be directly opposite another one on the other side. The magnetic field will be directed parallel to the anode axes. Each half-pump will generate a dense electron cloud within the anode. The electron cloud will spill over into the gap between the diametrically positioned anodes and be constrained to a spiral path by the magnetic field, thus ionizing the gas molecules. A point design of this configuration for a rectangular aperture of 10 cm by 50 cm and measuring 100 cm long requires 87 KV and consists of 400 half-pumps. This IACS can potentially provide attenuation of 10^{-2} for a gas kinetic temperature of 450 Kelvin. The electromagnet required for this configuration dissipates 250 watt if operated at 100 Kelvin. More detailed field calculations are required to further evaluate this concept.

The third IACS configuration has the pumping region located outside the optical field of view, and therefore pumps only the gas or particulate contaminants that strike the peripheral surface. The pump configuration can be two concentric cylindrical electrodes or an array of small getter pumps that blankets the periphery of the IACS. These configurations were not seriously pursued due to their inability to pump contaminant gases that come through the optical path. A perfect peripheral pump would be functionally equivalent to an ideal cryopump with the added ability to getter the contaminant molecules and permanetly bury them through chemisorption. Electromagnets will be used on the concentric cylindrical electrodes configuration and permanent magnets are considered for the array configuration.

The fourth IACS configuration uses no magnets. It uses an RF electric field to accelerate the electrons alternately to one direction and then the opposite direction as these electrons are injected into a resonant cavity. The electron ionization path is thus increased beyond the direct transversal path. The heavier gas ions are drawn to the collector plates. The RF cavity is essentially a rectangular box-like structure that accommodates rectangular apertures rather nicely. This box-like structure

is opened at two opposing sides so that the clear aperture is unobstructed. A preliminary point design for a 30 cm by 50 cm optical aperture and an interaction length of 50 cm requires 2 KW of power shared between the thermionic current source and the cavity loss. The weight of this cavity will be less than 20 pounds while the RF power supply may be 50 pounds. This point design will have an attenuation efficiency of 10^{-2}. Since the ionization path was examined for a selected few cavity modes, further examination of the entire cavity mode parameter space may yield more efficient cavity parameters and reduce power consumption.

Section Four summarizes the conceptual design of an experimental setup to measure the effectiveness of various ion pump configuration. This experiment will be conducted inside a vacuum chamber of modest dimension (i.e., 12 inches diameter by 36 inches length). The interior volume of this chamber will be partitioned into two volumes. A modified ion pump will be mounted at an orifice which connects the two volumes. The ability of the modified ion pump to sustain a differential pressure will be measured and analyzed to deduce the equivalent pumping speed.

Section Five presents an analysis of infrared radiation emission due to the electron-gas contaminant impact interaction. Initial results indicate radiance levels due to direct neutral molecule excitation and subsequent relaxation is marginally important given the uncertainty in the Einstein A coefficient.

Section Six proposed an experimental plan for measuring the infrared radiation level in an IACS. The goal of this experiment would be to operate a discharge similar to that to be used in the IACS under conditions that would be encountered during operation in space. A suitably modified Penning-type discharge will be pumping neon because of its similarity to oxygen atoms (a species of primary interest), and its high vapor pressure under cryogenic conditions. The radiation will be monitored using a broadband radiometer capable of measuring 10^{-11} w/cm^2-sr-um against the background of the cooled cryo-shroud at 20 Kelvin.

2.0 DEFINITION OF THE OPTICAL CONTAMINATION PROBLEM

2.1 Scope of the Contamination Problem Being Addressed

This study is centered around the definition of the optical contamination problem and the design study of a device that would alleviate this problem. The mission assumed will consist of a number of orbiting spacecrafts, each comprised of a sensor payload and the associated sensor navigational, communication and power generation subsystems. The sensor payload will be typically an optical telescope that operates at cryogenic temperatures. The spectral bands of the optical filters will be in the infrared. The focal plane will be comprised of detectors that operate close to BLIP.

The candidate orbital altitudes of the spacecraft are 600 and 5600 nautical miles.

The performance of these space looking sensors will be limited by the out of field-of-view rejection (OFVR) capabilities of the cryogenic IR telescope when viewing targets close to earth limb. In state-of-the-art high straylight rejection telescope designs, the dominant straylight coupling mechanism is associated with the optical scattering properties of the primary mirror. Manufacturing and maintenance of very low optical scattering characteristics on the primary mirror directly impacts the OFVR performance of the cryogenic telescope. This, in turn, may adversely affect the limb viewing performance of the sensors and thus affect overall system effectiveness.

The assumed mission lifetime of the system is 4 years. The potential buildup of spacecraft-generated contaminants and/or ambient species on cryogenically-cooled optical systems may degrade system performance to an unacceptable level. This is the impetus to the research and development of an Ion Anti-Contamination System (IACS) that can reduce the buildup rate of potential contaminants to an acceptable level.

2.2 Evidence for Problem of Mirror Contamination

Mirrors are contaminated in room temperature storage. The ZIP telescope primary mirror BRDF was degraded by two orders of magnitude after two years of vacuum storage. The telescope was brought up to atmospheric pressure in a clean room several times within this period. Aerospace Corporation has mirror samples which degrade in a clean room after 6 months. ELS and IRBS mirrors were degraded in clean room storage.

Mirrors are contaminated in cryogenic storage. The CIRRIS telescope primary mirror was degraded after 6 months in cryogenic storage at 30K.

Direct evidence of straylight was obtained on the SPIRE (cryogenic circular variable filter) and ELS (cryogenic grating spectrometer) flights. Data was obtained in the 16 um CO_2 emission level was reached and then remained constant at the predicted level.

2.3 Optical Parameter Impacts

Figure 1 summarized the assumed range of the system/sensor optical parameters and their applicability to the optical contamination problem.

2.4 Figure of Merit for Optical Contamination

Optical contamination is unwanted optical effects due to the presence of some material, substance or energy in the physical components of the optical telescope or within its optical field-of-view. For a space-borne cryogenic telescope that is required to detect weak point targets in the vicinity of a bright source, the maintenance of low background photon flux on the detector is very important. This may be the reason why the telescope was cooled to cryogenic temperature in the first place. The background photon flux that comes from within the telescope structural and optical components can be effectively controlled by cooling

PARAMETERS	ASSUMED RANGE	IMPACT
• BAFFLE TEMPERATURE	30 - 100 KELVIN	CRYO PUMPING OF H_2O VAPOR
• BAFFLE L/D	4 - 8	CRYOPUMPING OF H_2O VAPOR OXYGEN DEPOSITION RATE
• OPTICS TEMPERATURE	10 - 75 KELVIN	OXYGEN DEPOSITION RATE
• DEPOSITION THICKNESS	MONOLAYER TO 2 MICROMETER	ATTENUATION REQUIRED
• OPTICS DIMENSION	4 INCHES X 20 INCHES: TO 30 INCHES	UNDER STUDY
• FIELD-OF/VIEW	1° X 10° TO 15° X 15°	CRYOPUMPING OF H_2O VAPOR
• L.O.S. POSITION W/R TO VELOCITY VECTOR	10° TO 80°	OXYGEN DEPOSITION RATE

Figure 1. Ion Anti-Contamination Study System Optical System Parameter Impacts

the telescope to a temperature such that the self-emission is tolerable. The background photon flux that originates from out of field-of-view sources and scatters off the structural or optical components of the telescope is controlled through selection of a high straylight rejection optical configuration compatible with the addition of an optical baffle and minimization of optical scatter of the optical components.

Experimental OFVR test data have shown that better performance can be obtained on off-axis reimaging telescope configurations when compared with on-axis reimaging systems due to the absence of the secondary mirror support spider in the optical aperture. So, for a well-baffled optical configuration, the structural scatter can be controlled so that the residual optical scatter becomes the dominant OFVR limiting source.

The figure of merit for the optical scattering properties of mirror is the Bidirectional Reflectance Distribution Function (BRDF). Maintenance of the primary mirror BRDF at low initial values throughout a 4 year mission life requires protective measures against optical contamination.

Bidirectional Reflectance Distribution Function (BRDF)

All surfaces, ranging from "black" absorbing surfaces to highly-polished mirrors, have a characteristic Bidirectional Reflectance Distribution Function (BRDF). This is a function describing the reflectance at all angles out for all input angles of incident radiation. Although the term is simple in concept it is much abused. A single plot of scattered energy versus output angle does not necessarily indicate that the BRDF of that material has been specified for all angles of input and scatter.

There are two cases that apparently satisfy this simplification. Well-polished mirror surfaces exhibit a linear shift-invariant characteristic. Also, a classical Lambertian scattering surface has a fixed BRDF profile. However, no "black" material tested exhibits Lambertian characteristics at all incident angles.

It should be noted that BRDF is generally dependent on the optical wavelength.

Low scatter finish (i.e., low BRDF values) of cryogenic mirrors are known to be degraded by the deposition of particulates and cryodeposits. Described in the following sections is an account of where they come from and how they will affect the mirror BRDFs.

2.5 Contamination Due to Particulate Sources

Particulates deposited on low scatter mirrors will produce Mie scattering with large forward components, thus increase the effective BRDF of a low scatter sample. These particulates can be attached to the mirror prior to sensor launch. Probable mechanisms include residuals on mirror after cleaning, airborne particles settling on interior surfaces during sensor assembly and subsequently transported to the mirror during thermal vacuum test cycles, shock and vibration test cycles, and the launch acceleration. Small particles are rather tenacious and adhere to a surface well so that a large force is required to dislodge it. Larger particles (i.e.$\sim$100 um) dislodge more easily.

After the sensor cover is opened in orbit, particulates existed or generated outside the sensor can be transported into the mirror through the entrance aperture. Examples of particulate generation mechanisms include micrometeoroid impacts and spallation due to a nearby nuclear explosion.

2.5.1 Particulate Contamination on Clean Bench

The first report on scatter (BRDF) data due to particulate contamination appeared in Optical Engineering in 1974. The near-axis scatter of infrared (10.6 um) energy from high reflectivity metal mirrors was described. Figure 2 illustrates the effects of dust on BRDF of high quality low scatter electroless nickel-coated aluminum mirrors. Open and shaded symbols are used to designate the data obtained by AEDC and

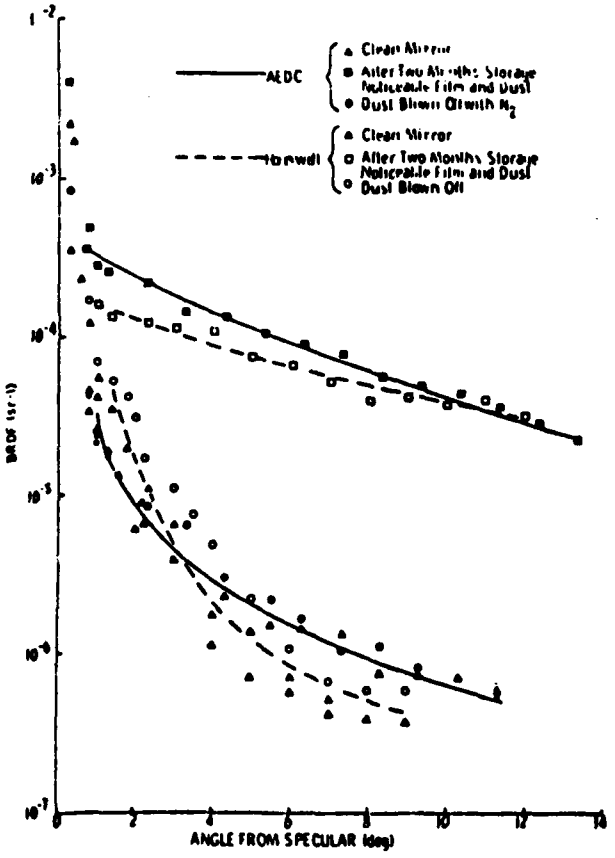

Figure 2. Effect of Dust on BRDF of Metal Mirror

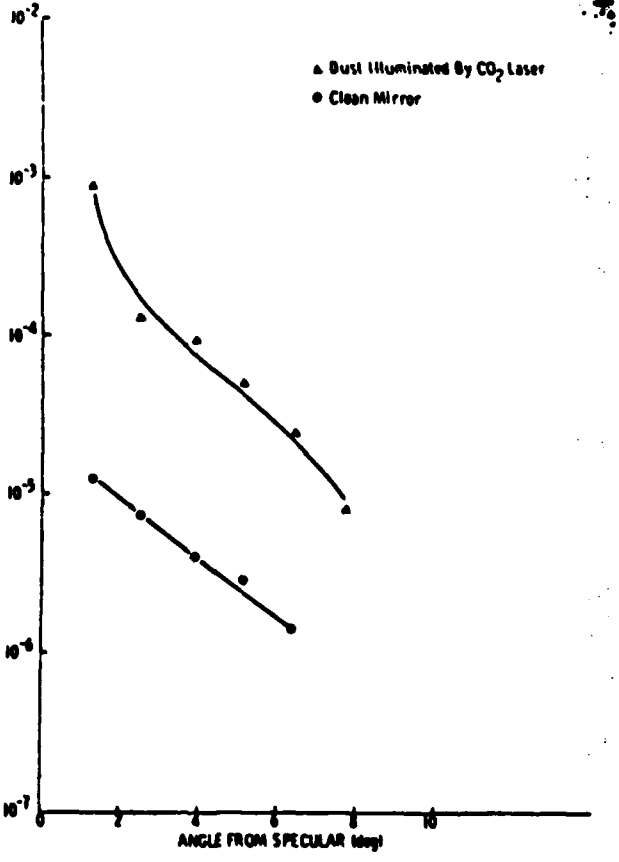

Figure 3. Mirror Degradation Resulting from One Piece of Dust

Honeywell on two different low scatter mirrors. The squares in Figure 2 illustrate the comparative scatter data for the same mirror after a considerable amount of dust was permitted to collect on the surface. It is significant to note that the dust was collected while the mirrors were located in a class 100 laminar flow clean bench. The comparison of the data before and after contamination is striking. There is about a two order of magnitude increase in the scattered energy due to the contamination. After the BRDF had been obtained on the mirror surface contaminated with dust particles, the surfaces were cleaned. The BRDF, after blowing the surface clean with nitrogen, is presented in the form of circles in Figure 2. The above characteristic was evident in routine measurements made in both laboratories.

A set of data on the effects of one dust particle has been reported in the same article and reproduced in Figure 3. In this figure the mirror scatter (BRDF) of the clean surface was about 10^{-5} and below as a function of angle from the specular beam. One piece of dust fell onto the surface of the mirror. The CO_2 laser was aligned to illuminate that particle. The resultant BRDF is shown in Figure 3. The increase in scatter is obvious. Blowing the particle off returned the scatter to the original clean mirror values.

2.5.2 Poly-Dispersed Particle-Scattering Data Agrees with Mie Scatter Theory.

This data was obtained by R. P. Young of ARO and reported in Reference 2. The scatter data in this paper resulted from the contamination of a low scatter mirror with spherical, silver particles (nominal diameters between 9 and 18 um). The energy scattered by the mirror surface was several orders of magnitude below that from the particles, and was considered negligible for the BRDF calculations. Figure 4 is a particle size distribution plot. Most of the silver particles on the glass slide were in the size range between 8.19 and 17.6 um diameter. Nominally 1.7% of the surface was obscured by the contaminant. Particle density was nominally 1.5×10^7 particles/ft^2. The particles were

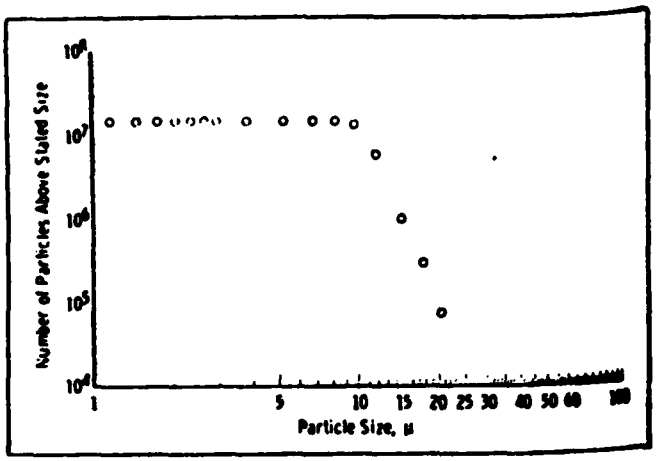

Figure 4. Particle Distribution Plot for Glass Slide Contaminated with 9 to 18 μm Diameter Silver Particles.

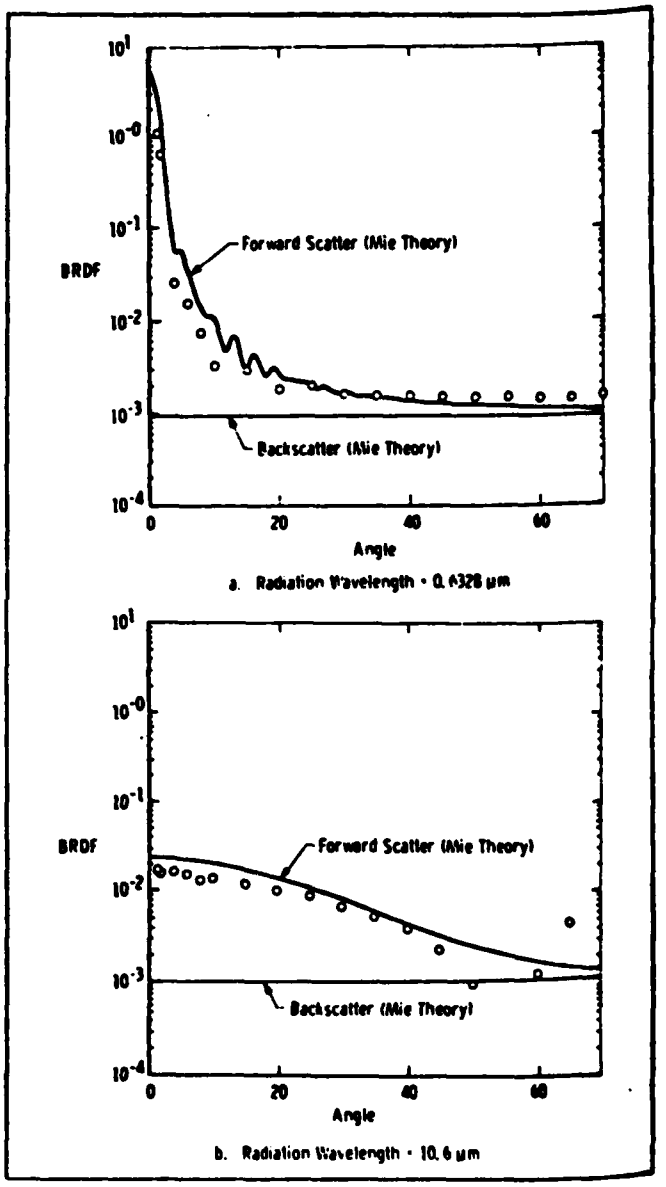

Figure 5. BRDF of Spherical Silver Particles Deposited on a High Quality Low-Scatter Mirror.

Ref: R. P. Young
"Low Scatter Mirror Degradation by Particle Contamination" Optical Engineering Vol 15 No 6 (1976).

uniformly distributed over the glass slide surface, and were sufficiently far apart to prevent interaction of scattered radiation from adjacent surfaces.

Results of the scatter measurements from the contaminated mirror are presented in Figure 5. The vertical axis in Figure 5 is the particle BRDF and the horizontal axis is the scattering angle as measured from the specular beam. Angle of incidence of the illuminating laser beam was 2°. The solid curve was obtained from the Mie scatter theory. The upper curve is the forward particle scatter, reflected toward the radiometer from the mirror surface. The lower curve represents the backscatter from the particle contaminant. Measured scatter data are presented by the circular symbols in Figure 5.

Results of the particle-scattering measurements at 0.6328 um show that the particle BRDF was strongly dependent on scattering angle, decreasing rapidly as the angle from specular increases. Beyond about 20° from specular the BRDF became almost independent of the scattering angle. The measured data agree favorably with the theoretical values of the forward-scattering prediction.

Results of 10.6 um measurements show that the near-specular BRDF was relatively independent on the scatter angle. The BRDF at 10.6 um was lower than BRDF at 0.6328 um up to about 10° from specular. From 10° to about 50° the 10.6 um BRDF was higher than the 0.6328 um BRDF. The measured 10.6 um BRDF data again agree favorably with the theoretically predicted values for the Mie forward scattering for angular measurements between 0° and 45°.

Results of computations for the forward scattering of spherical particles for various degrees of mirror contamination are presented in Figure 6. Particle size was obtained from MIL-STD-1246A. Incident radiation was 5, 10, and 20 um for Figures 6a, 6b and 6c, respectively. Note that the BRDF curves decrease as the radiation wavelength increases, and that the BRDF varies with the scattering angle. The forward scattering

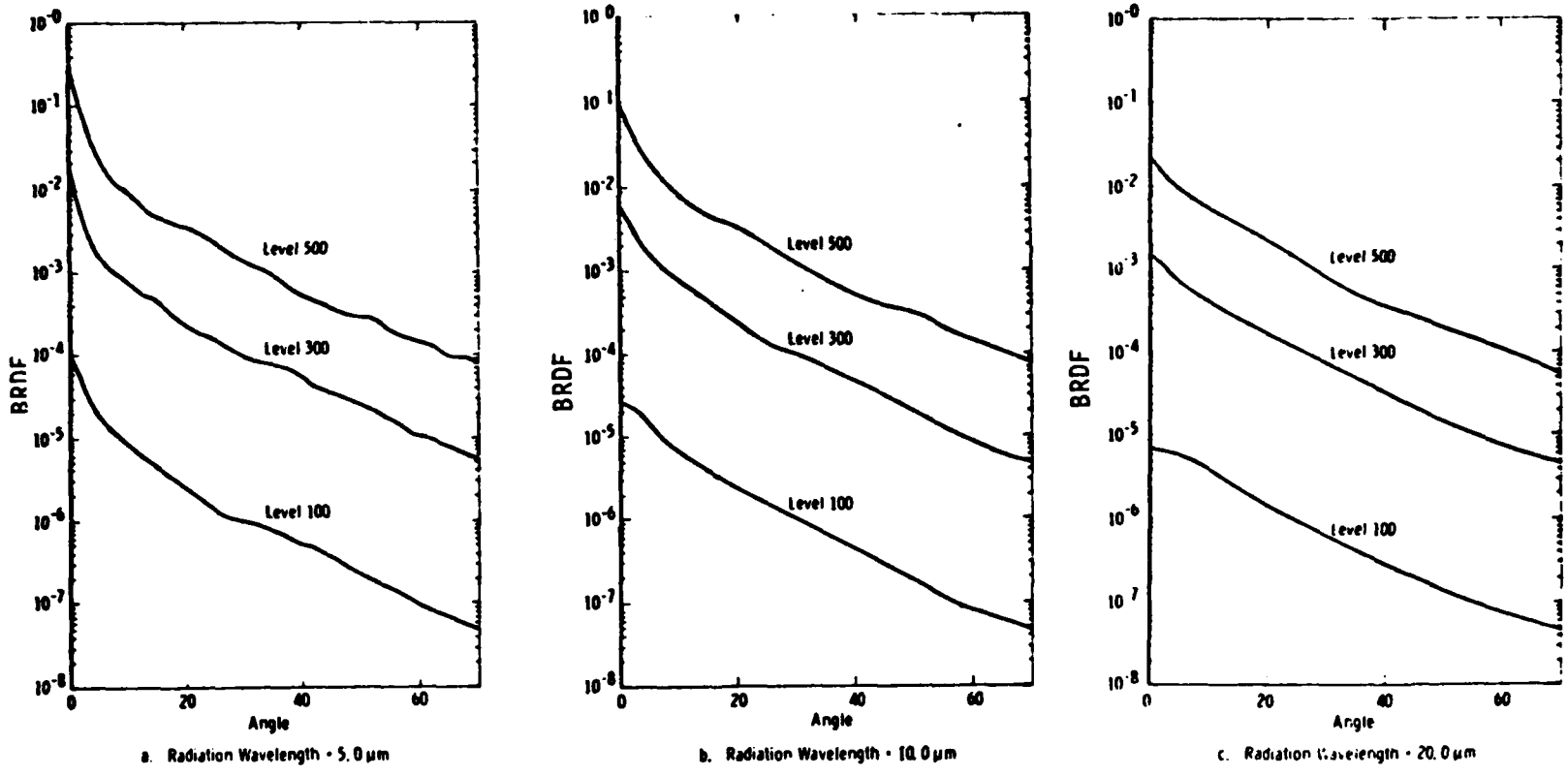

Figure 6. Theoretical Prediction of BRDF AFter Particulate Contamination. (Ref: R. P. Young, "Low Scatter Mirror Degredation by Particle Contamination," Optical Engineering 15, No. 6)

values are not strongly dependent on particle material; therefore, the theoretical results in Figure 6 are relatively independent of the particle composition. The BRDF curves of Figure 6 include particle scattering only. Mirror scatter would have to be added to these values to obtain total surface radiation scattering.

2.5.3 Monodispersed Particle Scattering at 10.6 um

Increase in BRDF due to contamination by monodispersed particle size distribution was reported in Reference 3. The contaminant particles were polystyrene vinyl spheres of a single size. The mirror surfaces had an outside layer of silver overcoated with silicon oxide. The test procedure consisted of first measuring the BRDF of the four clean mirrors with the CO_2 laser. Uniform spherical latex particles held in a water suspension were deposited on each mirror with separate eye droppers. Figure 7 shows the increase in BRDF above that of the clean mirror for a surface coverage of 1.5 percent of a monolayer by particle diameters of 5.2, 9.8, 15.4 and 22.2 um. It is interesting to note that the slope of the BRDF increases as particle diameter increases and the data points fit a straight line of the form BRDF - $A\theta^{-B}$. The BRDF of a contaminated mirror is given by the sum of the BRDF plotted in Figure 7 and the BRDF of a clean mirror.

2.5.4 Sensor OFVR Data Before and After Particulate Contamination

Particulate contamination of a high straylight rejection IR cryogenic telescope was reported in Reference 4. This telescope is a highly baffled, off-axis, doubly folded reimaging optical system. The optical train consists of eleven gold-coated mirrors, of which the first and second mirrors are superpolished, low scatter mirrors.

The OFVR characteristics of the telescope are expressed as Point Source Power Transmittance (PSPT) versus Out of Field Angle (OFA). Since the PSPT is directly proportional to the detector instantaneous field of view (IFOV), the data were normalized for an IFOV of 1 microsteradiance.

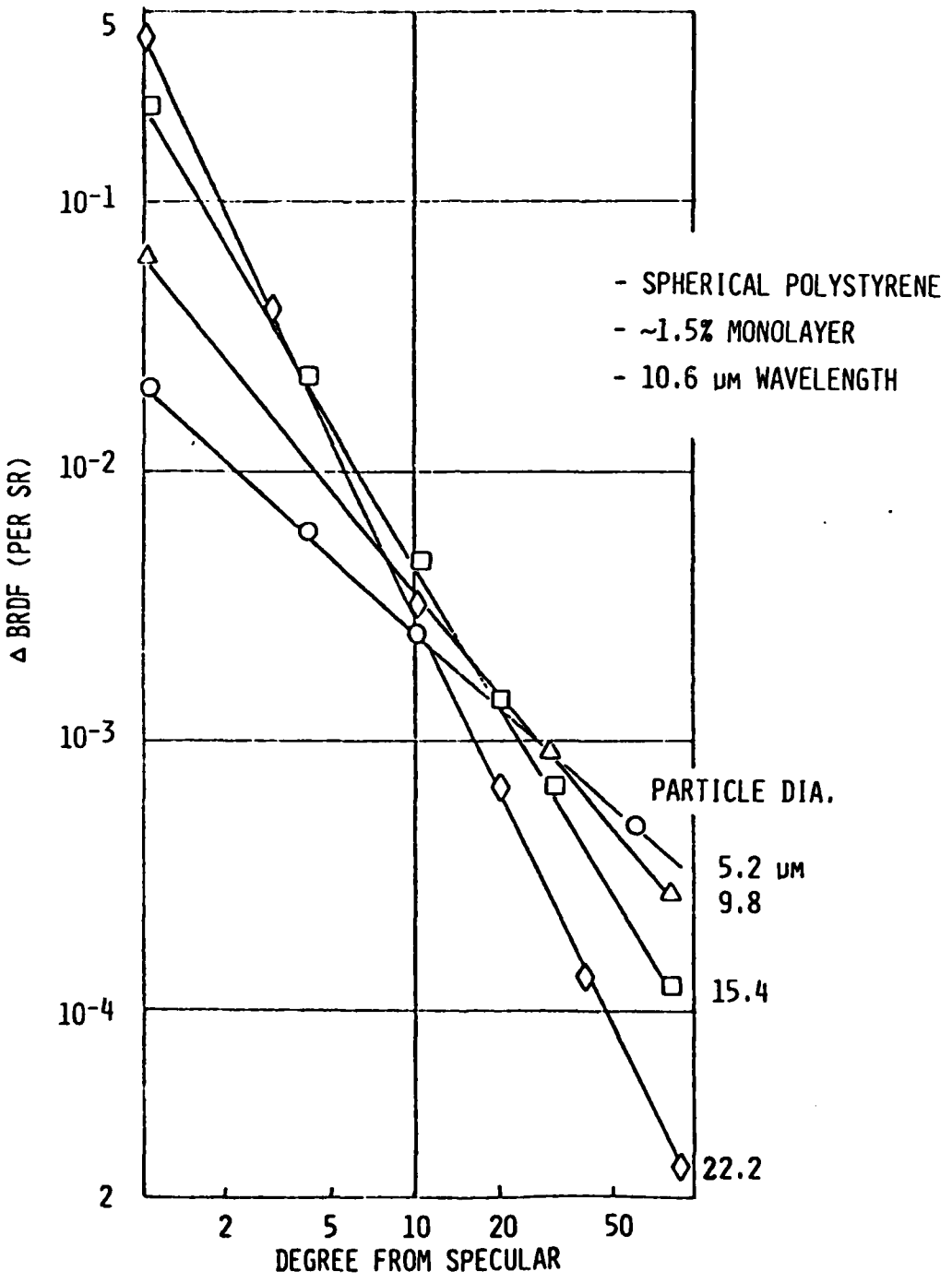

Figure 7. Experimental Determination of BRDF from Particulate Scatter (Martin/AEC) Ref: Somers, Muscare, "Effects of Contaminants on BRDF: SPIE Vol 338

Since the original (pre-storage) OFVR test, the telescope was integrated into an evacuated vessel and underwent 5 cryogenic test cycles during a period of 1 year. Afterward, the telescope was placed in the vacuum vessel and stored in an evacuated pressure of less than 10^{-3}mm Hg at room temperature for a duration of 2 more years. All of the other OFVR tests were performed after this storage period.

The OFVR data shown in Figure 8 is the OFVR characteristic in the -Elevation direction with respect to test detector line-of-sight. This is the scan direction that would have the off-axis collimated laser source illuminating the top side of the baffle tube. The PSPT is plotted in logarithmic scale while the OFA is in linear scale and the data is normalized to a 1 usr detector IFOV. Four OFVR measurements along the same scan direction are illustrated in Figure 8. The "triangular" symbols are data for the original (pre-storage) OFVR test. They are joined by straight lines for clarity. The implied BRDF of the primary mirror was 1×10^{-4} per sr at 1°.

The "rhombus" symbols are data recorded after the telescope was taken out from storage and placed in the OFVR test facility. The PSPT for OFA less than 5° increases by a factor of 200 to 400. This is the OFA regime for which the primary mirror is fully illuminated. One can conclude that the increase in PSPT is due to the optical contamination of the primary mirror. Subsequent removal of the baffle system and visual inspection of the primary indicated that many dust particles can be seen on the mirror surface.

Subsequent thorough washing of the primary removed all visible particulates and the OFVR was retested. This test data is shown in Figure 8 as "square" symbols. It is apparent that the OFVR performance was restored for OFA between 2° to 7°, but the OFVR was still degraded by a factor of 2 to 20 for OFA between 8° to 15°.

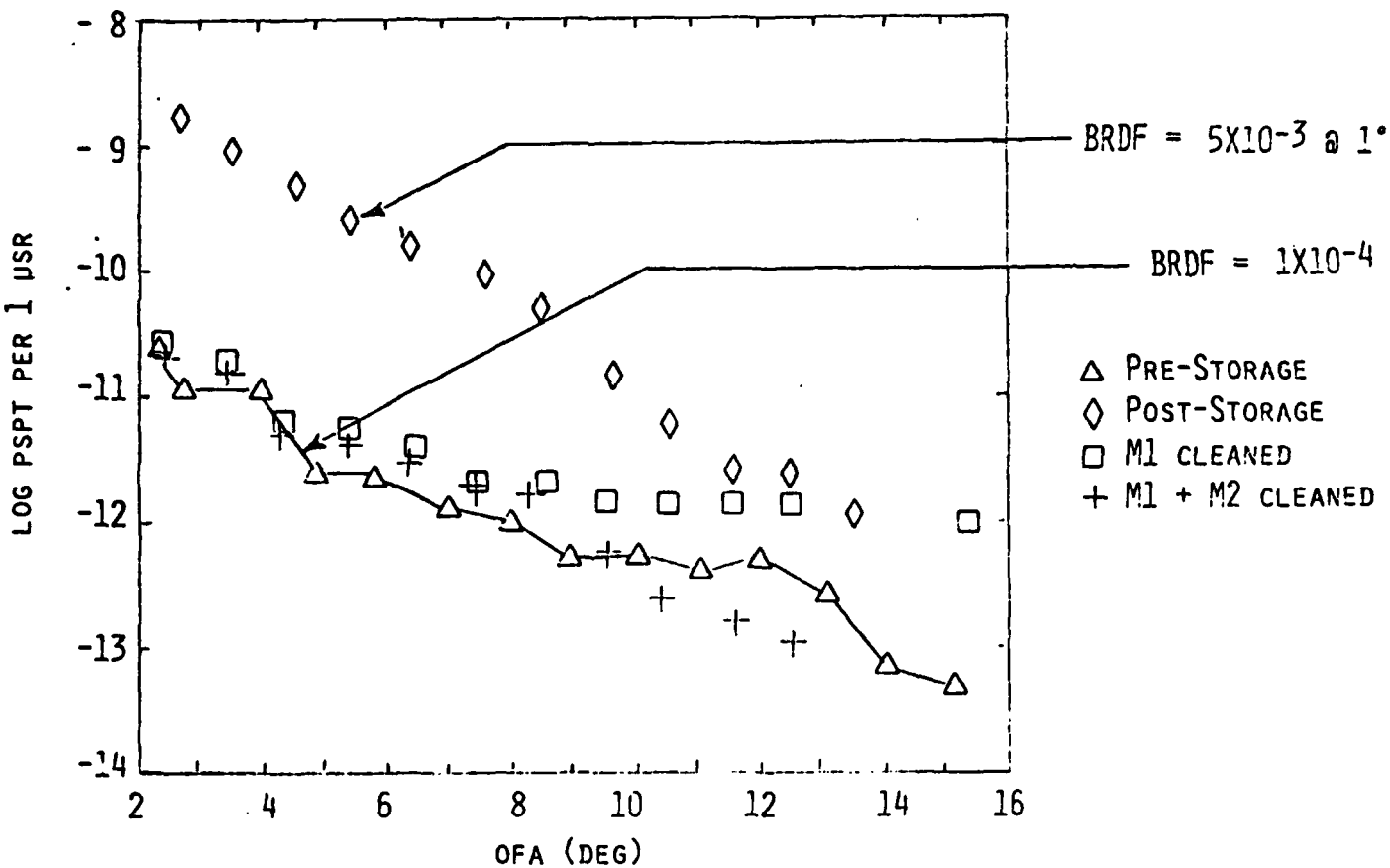

Figure 8. Experimental OFVR Data Particulate Contamination: SSG-ZIP Telescope (Ref: Wong, Wang and Murdock, "Out of Field of Vie, Rejection Measurements of the ZIP Telescope #2," SPIE vol. 384

The secondary mirror was also cleaned and then the OFVR was remeasured and plotted in Figure 8 as "plus" symbols. It is apparent that the OFVR is restored to its prestorage values of three years ago.

In summary, particulate contamination on a sensor during test, integration and storage is demonstrated and reported. The impact on sensor OFVR is significant. A factor of 400 increase in straylight would increase BLIP detector noise levels 20 times! It is also demonstrated that thorough cleaning of M1 can restore OFVR performance for most OFA's. Additional cleaning of M2 restore OFVR for all OFA's. One solution to alleviate the on-ground sensor particulate contamination problem is to design into sensor hardware the provision to clean M1 and M2 in situ after all optical, thermal and vibrational test cycles.

2.5.5 Mechanism of Particulate Contamination of Mirrors

Particles Inside Telescope

A clean mirror can be contaminated during the assembly test and launch procedures if the other telescope interior surfaces are contaminated. These contaminations include: (1) particles generated and deposited during assembly, and (2) particles generated during test and launch.

(1) Metal chips sometimes are created during assembly. Some optically black paints flake. Assembly personnel deposit human skin flakes, hair, dirt and other fabric material into the clean work area. Airborne particles settle on surfaces.

(2) Large particles are dislodged under vibration and shock and can fall on the mirror. Smaller particles can be carried around by gaseous turbulence during cryo vacuum test cycles. Very small particles (1 um) adhere to surfaces by Van de Waal forces and removal requires 1000 g's of acceleration.

Particles Outside Telescope

Exterior surfaces on a sensor payload will have some particles attached. These particles can be released in orbit and its trajectory will be determined by the particle ejection velocity, atmospheric drag, solar radiation and coriolis acceleration. Forces that would release these particles include impact of micrometeoroid, and bursting of bubbles of gas trapped in various material.

2.6 Contamination Due to Gaseous Cryodeposits

2.6.1 Effects of Cryodepost Contamination

Effects of cryodeposit contamination of low scatter mirrors was reported by AEDC. The results are summarized in Figure 9. Cryodeposits of water vapor (H_2O) and oxygen (O_2) are of special importance.

The multi-layered insulation (MLI) used in cryogenic sensors exhibits significant outgassing over long term (i.e., hundreds of hours) and the outgassed species is 99.5% H_2O (Figure 10). Figure 11 illustrates the H_2O cyrodeposit effects on BRDF.

The importance of oxygen is due to the abundance of atomic oxygen at altitudes between 200 and 1000 km during maximum solar activity. At high altitudes of 10,000 km, the number density of atomic oxygen falls off to a level of insignificance. The effects of 10.6 um BRDF due to oxygen and carbon dioxide cryodeposits of various thicknesses in um are plotted in Figure 12. It is apparent that the smaller angle BRDF can increase by an order of magnitude for 10 um thick of O_2 cryodeposits. Another significant effect is the disproportionate increase in scatter for large off-specular angles. Carbon dioxide concentration is very low in the atmosphere above 100 km altitude. However, it can be a significant component of some propellant gas mixtures.

- GASEOUS SPECIES INVESTIGATED
  N_2, O_2, NH_3, CO, AIR, H_2O, MIXTURES
- N_2: - CRYODEPOSIT OF N_2 WAS HIGHLY VISIBLE BUT SHOW NO INCREASE IN IR SCATTER (THICKNESS UP TO 29μm)
  - SCATTER INCREASE WAS MEASURED FROM N_2 DEPOSIT BY SLOWLY WARMING THE MIRROR UNTIL PARTIAL VAPORIZATION OCCURED. (FIG 11)
- O_2: - ONLY GAS WHICH CAUSED CONSISTENT INCREASE IN SCATTER WITH DEPOSITED THICKNESS. MEASURED 2 ORDERS OF MAGNITUDE INCREASE FOR THICKNESS OF 10μm. (FIG.12 & 13).
- CO_2: - INCREASE IN IR SCATTER IF DEPOSITED ON A LOW TEMPERATURE SURFACE (20 TO 25°K) BUT NOT WHEN DEPOSITED ON A NEAR MAXIMUM MIRROR TEMPERATURE OF 80° K. HOWEVER, WHEN THE DEPOSIT WAS COOLED, IT SHATTERED AT 60K AND RESULTS IN HAIRLIKE CRYSTALS ON PART OF THE MIRROR 5 DECADES INCREASE OF SCATTER
- NH_3: - UNPREDICTABLE BECAUSE OF ITS TENDENCY TO SHATTER OR CRYSTALLIZE, EITHER DURING DEPOSITION OR IF MIRROR TEMPERATURE IS CHANGED AFTER DEPOSITION.
- CO: - NOT SIGNIFICANT INCREASE OF IR SCATTER WAS FOUND (THICKNESS UP TO 6μm).
- H_2O: - DEPOSIT SHATTERED DURING DEPOSITION FOR COLD GAS ON COLD MIRROR (4 TO 5 ORDER OF MAGNITUDE - WATER ABSORBS 10.6μm RADIATION INCREASE).
- AMBIENT AIR: NONE OF THE DEPOSITS SHOWN ANY INCREASE IN IR SCATTER
- AMMONIA-NITROGEN: NO LARGE INCREASE IN SCATTER UNLESS THE DEPOSIT SHATTERED.
- SIMULATED PROPELLENT GAS: (3% CO; 11% CO_2; 39% N_2, 47% H_2O). INCREASE IR SCATTER WAS OBSERVED ONLY IF THE CRYODEPOSIT SHATTERED DURING WARMUP.
- NITROGEN AND OXYGEN - RANDOM INCIDENCE: SCATTER MORE THAN NORMAL INCIDENCE.

Figure 9. Effects of Cryodeposit Contamination on Low-Scatter Mirrors

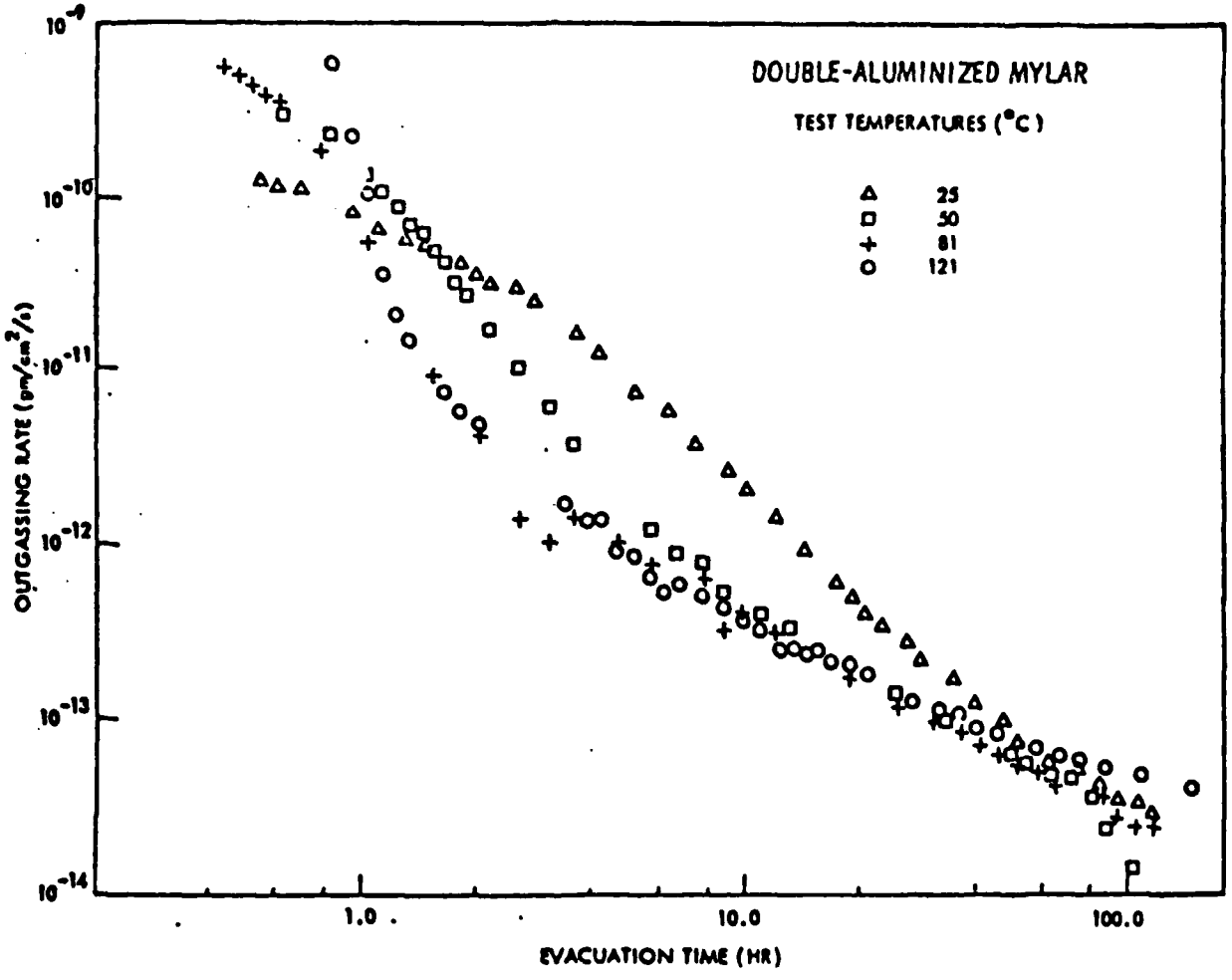

Figure 10. Outgassing Rate of Doubly-Aluminized Mylar for Temperatures of 25° C and Above (Ref: Glassford and Kiu, "Outgassing Rate of Multilayer Insulation," Proc. of the USAF/NASA International Spacecraft Contamination Conference, AFML, 1978.

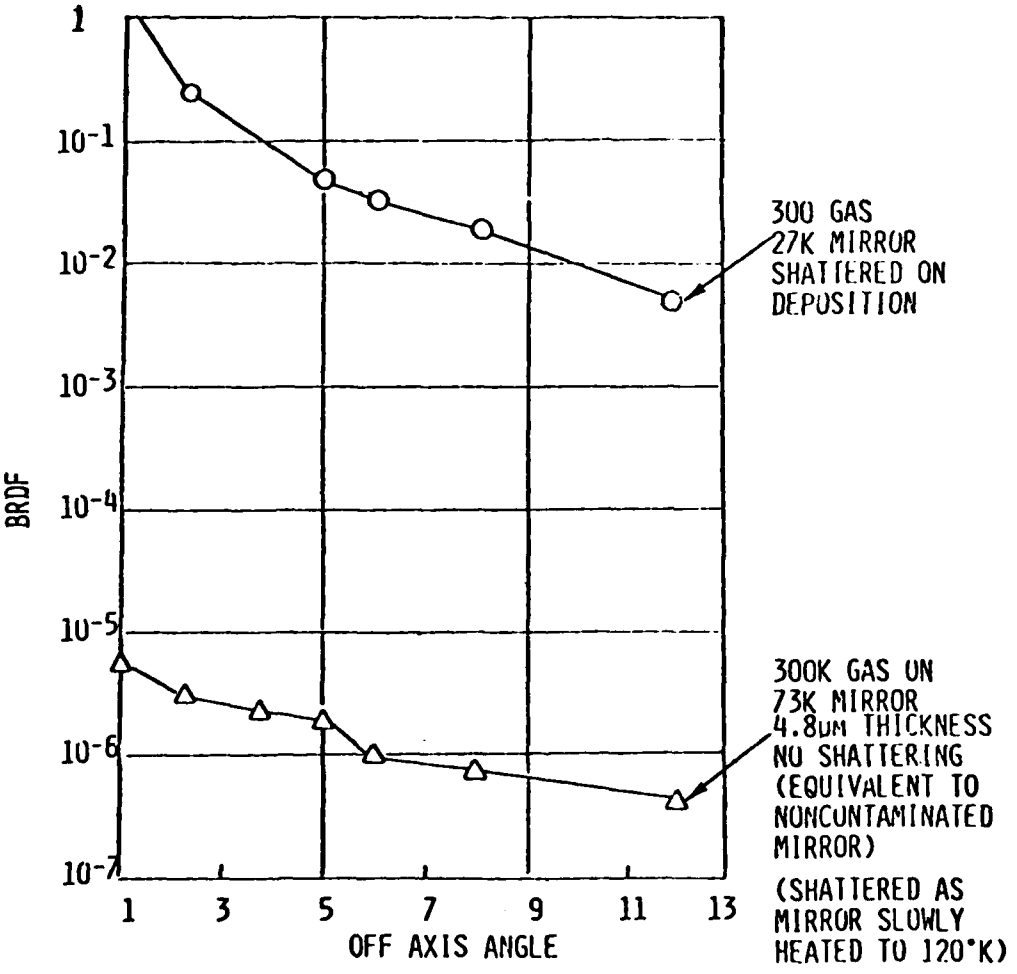

Figure 11. H_2O Cryodeposit Effects on BRDF (Ref: "Degradation of Low Scatter Metal Mirrors by Cryodeposit Contamination,: AEDC-TR-75-128, Oct. 1975)

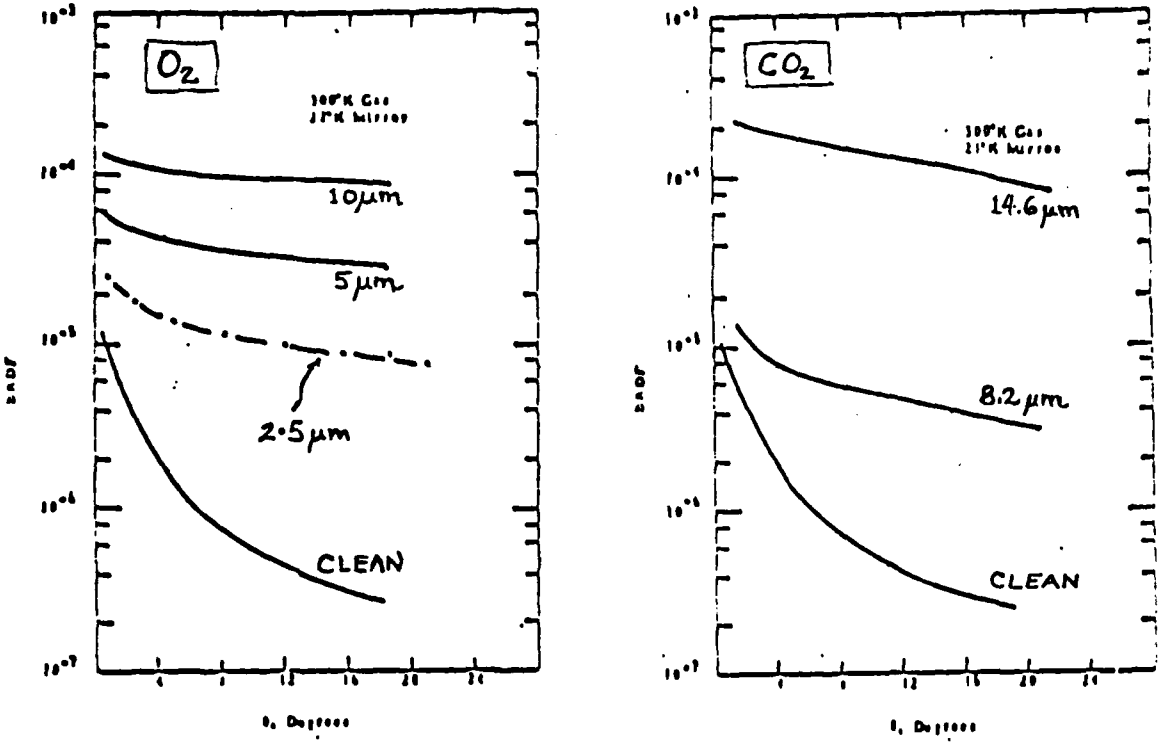

Figure 12. Degradation of BRDF of Ni Plated Al Mirror due to O_2 and CO_2 Cryodeposition; λ = 10.6 μm (After Arnold, F., "Degradation of Low-Scatter Metal Mirrors by Cryodeposit Contamination," AEDC-TR-75-128, October 1975).

2.6.2 Sensor Gaseous Contamination Problem

For a baseline mission, the sensor(s) will be attached to a free-flying spacecraft at one of the two potential altitudes - 600 or 5600 nautical miles. The BRDF of the optical mirrors may be limited by the buildup of spacecraft-generated contaminants and/or ambient species. There is limited data on the contaminant environment, particularly the spacecraft outgassing. In the following, we have examined the problem of contamination by atmospheric ambient species and have concluded that the primary problem is atomic oxygen. The build-up is very sensitive to mirror temperature and appears to be insignificant for temperatures above 30 Kelvin.

Because of the limited data on spacecraft outgassing and because of the dependence of the return flux on spacecraft geometry, it appears that little can be stated at present about the deposition rates of these species. However, most of the known species are condensed at the baffle temperatures and, for reasonable baffle L/D, are reduced significantly by condensation on the baffle walls.

2.6.2.1 Cryopumping of Ambient Species

A spacecraft in circular orbit at 800 kilometers has a velocity of 7.5×10^5 cm-sec^{-1}, which is large compared to the thermal velocity of ambient molecules of interest. Consider as a worst case the situation shown in Figure 13. The telescope baffle is aligned with the velocity vector of the satellite and the material scooped up by the baffle will be the product of the ambient density multiplied by the satellite velocity. The rate, R, of deposition of a given atomic or molecular species on the primary mirror is given by:

$$R = \frac{v_s \, [x] \, m_x \, a_x}{p_x} \quad (\text{cm sec}^{-1})$$

where

v_s = the velocity of a satellite in circular orbit at 800 km (7.5×10^5 cm sec^{-1})

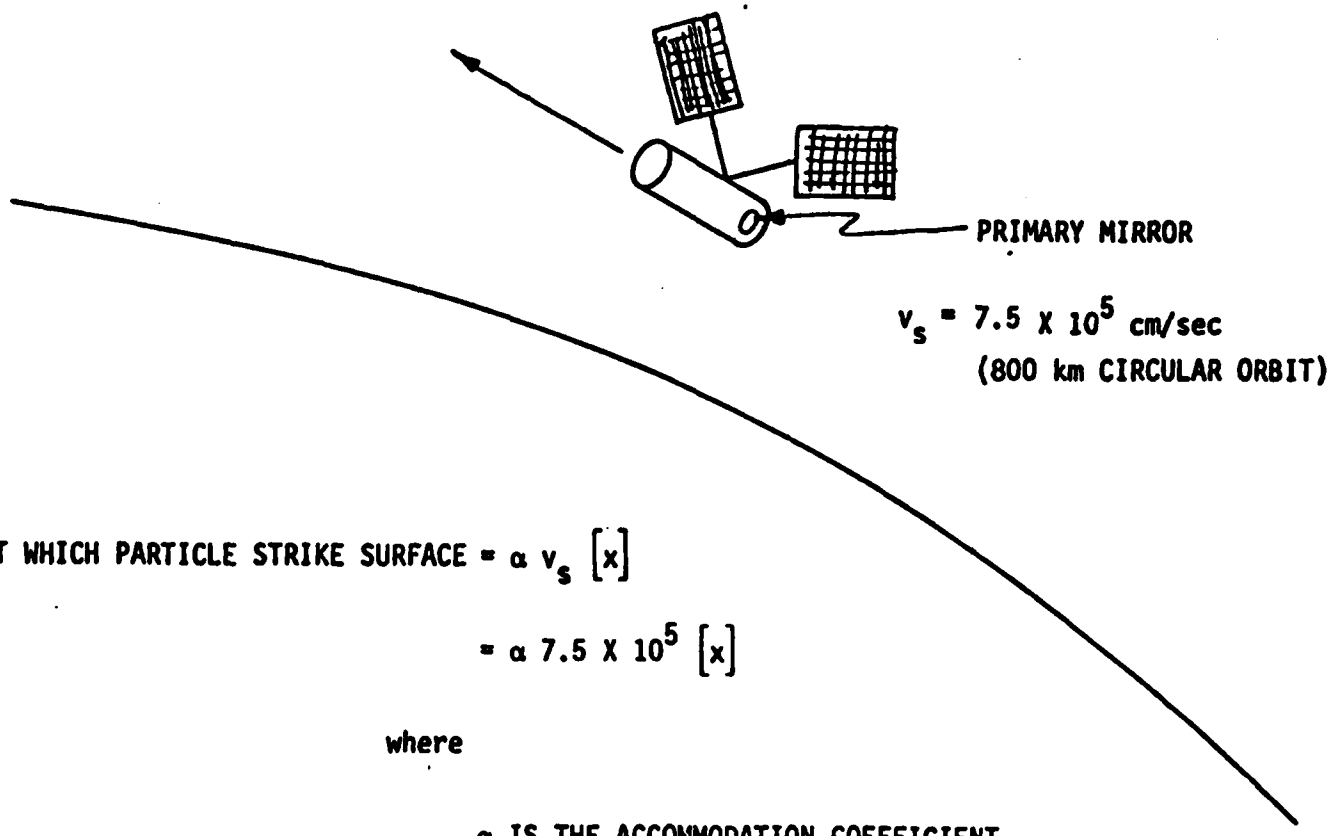

RATE AT WHICH PARTICLE STRIKE SURFACE = $\alpha v_s [x]$

$= \alpha\ 7.5 \times 10^5 [x]$

where

α IS THE ACCOMMODATION COEFFICIENT

$[x]$ IS THE SPECIES DENSITY

Figure 13. Worst Case Geometry

$[x]$ = number density of the species x (cm^{-3})

m_x = weight of an atom or molecule of species x (gm)

p_x = density of species x at primary mirror temperature (gm cm^{-3})

a_x = accommodation coefficient (fraction striking surface which sticks to it).

A reasonable stringent criterion is that the deposition buildup be less than 0.1 um per year (3.2×10^{-9} um sec^{-1}). This is a buildup of a thickness equal to a hundredth of a wave per year for a system operating at 10 um. If we assume an accommodation coefficient of 1, the minimum number density of a species that can produce the specified deposition buildup or great is given by

$$[x]_{min} = 4.3 \times 10^{-19} \, p_x/m_x$$

Figure 14 shows the relative concentration of ambient species as a function of altitude for the conditions minimum and maximum solar activitiy[7]. For the species shown in Figure 14, the calculated values of $[x]_{min}$ are as follows:

SPECIES	$[x]_{min}$ (cm^{-3})
H	1.8×10^4
He	8.0×10^3
O	1.8×10^4
O_2	9.2×10^3
N_2	7.4×10^3
Ar	2.0×10^4

In general, species whose densities are less than 10^4 cm^{-3}, or 10^{10} m^{-3}, are not a problem. During periods of minimum solar activity, only H and He exceed densities of 8×10^9 m^{-3} above 650 kilometers (Figure 14). However, at periods of maximum solar activity, H, He, O, O_2, and N_2

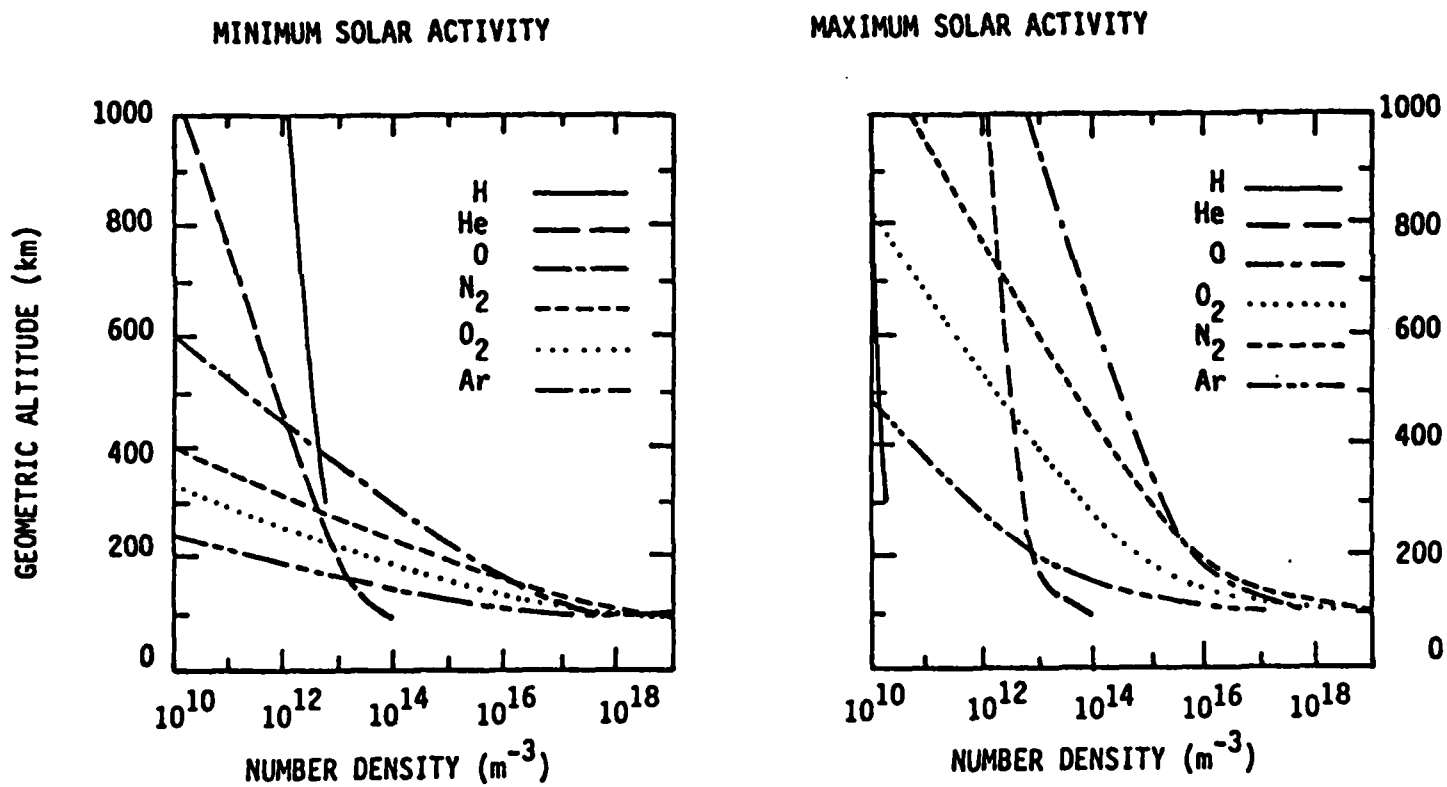

Figure 14. Relative Concentrations of Atmospheric Constituents

exceed $10^{10}m^{-3}$ above 600 kilometers. We will consider these species in the following sections.

Ambient Oxygen (O and O_2) - Consider the ambient atomic oxygen concentration. Figure 15 shows the ambient atomic oxygen concentration from the 1976 Standard atmosphere[7] and upper and lower values estimated for maximum and minimum solar activity. As the oxygen deposits, it can react with the surface material for form various oxides. However, after tens of monolayers are built up, the depositing oxygen is shielded from the surface, and it is assumed the depositing atomic oxygen will recombine to form O_2, so that the rate of vaporization of oxygen from the surface is determined by the vapor pressure of molecular oxygen, which is shown in Figure 16[8].

Now, as mentioned previously, the worst case is when the optical axis of the instrument is aligned with the velocity vector. Since the spacecraft velocity is large compared to the ambient velocity, the baffle or plate will scoop out the air and the number of atoms, N, striking the surface is given by

$$N = a\, v_s\, [O] = a\ 7.4 \times 10^5 [O]\ cm^{-2}sec^{-1}. \qquad (2)$$

Since we are assuming two atoms recombine to form one molecule, the number of oxygen molecules depositing per second on the surface is a (7.4×10^5) [O]/2, and the number leaving is $\frac{a}{4} p_{vap}\left(\frac{8}{\pi KTm}\right)^{\frac{1}{2}}$

where T is the surface temperature in degrees Kelvin, m is the molecular mass in grams, and p_{vap} is the vapor pressure in dynes/cm^2. The deposit will build up if [O] is greater than $[O]_{min}$, where

$$\frac{[O]_{min}}{2} = 6.3 \times 10^{12} \frac{P_{vap}}{T^{\frac{1}{2}}} \qquad (3)$$

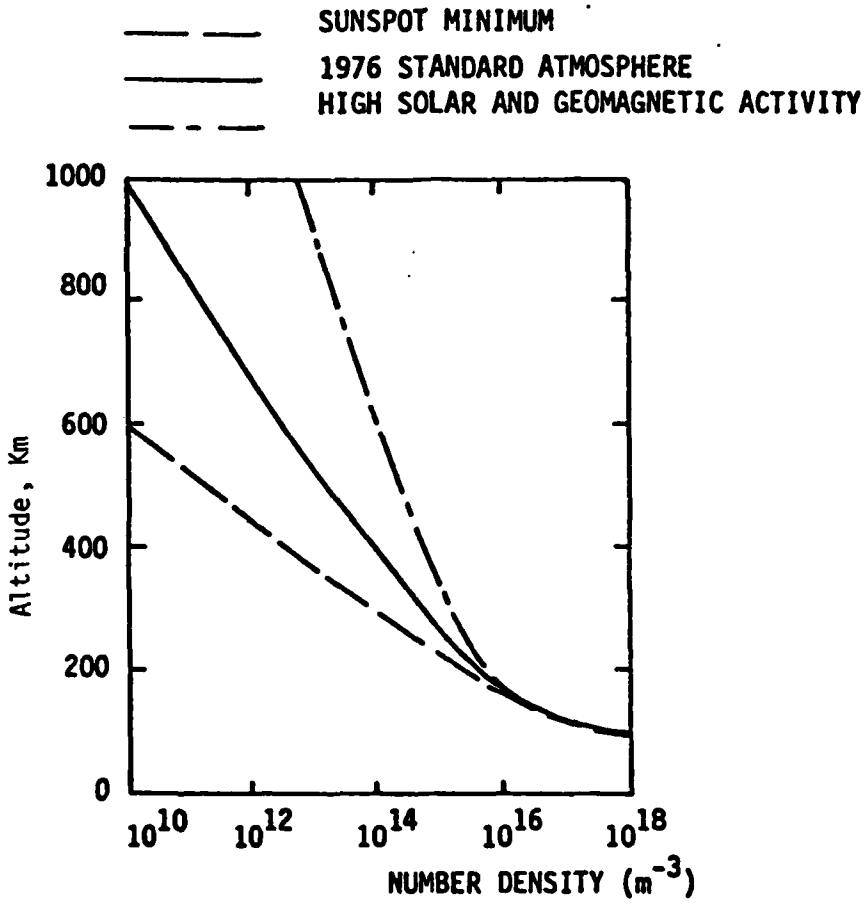

Figure 15. Limits of Atomic Oxygen Concentration vs. Altitude

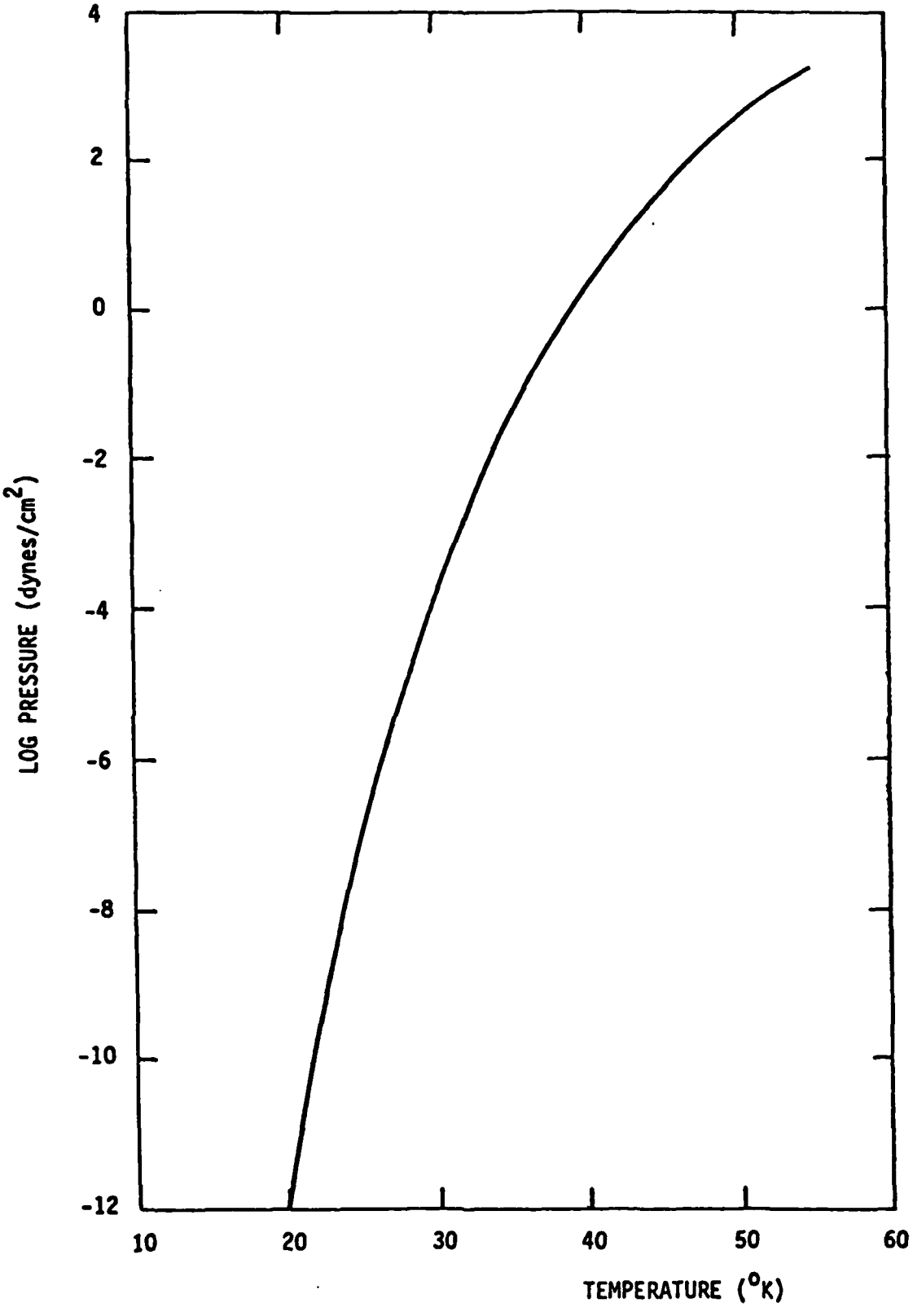

Figure 16. Vapor Pressure of O_2 vs. Temperature

Analogously,

$$[O_2]_{min} = 6.3 \times 10^{12} \frac{P_{vap}}{T^{1/2}} \qquad (4)$$

Figure 17 shows the dependence of the minimum oxygen concentration required for an oxygen coating to begin building up on the mirror surface as a function of surface temperature. From Figure 15, the maximum O concentration above 650 kilometers is 10^8 cm^{-3}. From Figure 17, then O deposition is significant for mirror temperatures less than 30 Kelvin. Since, from Figure 14, the maximum O_2 concentration above 650 kilometers is more than two orders of magnitude less than atomic oxygen, ambient O_2 contamination can be neglected compared to that of atomic oxygen.

If the optical axis is not along he velocity vector, the material scooped up is proportional to the projection of telescope aperture in the direction of the velocity vector. Assuming that the telescope will sample all pointing directions (with respect to the velocity vector) uniformly reduces the average deposition by a factor of four.

Ambient Nitrogen - Following equation 5,

$$[N_2]_{min} = 6.3 \times 10^{-12} \frac{P_{vap}}{T^{1/2}}.$$

Figure 18 shows the N_2 vapor pressure dependence on temperature[9]. Since, at the temperature range of interest (30 - 35°K), the vapor pressure of N_2 is significantly higher than O_2 (Figure 16), and since above 650 kilometers, the N_2 density is at least an order of magnitude lower than O, nitrogen deposition can be neglected when compared to O.

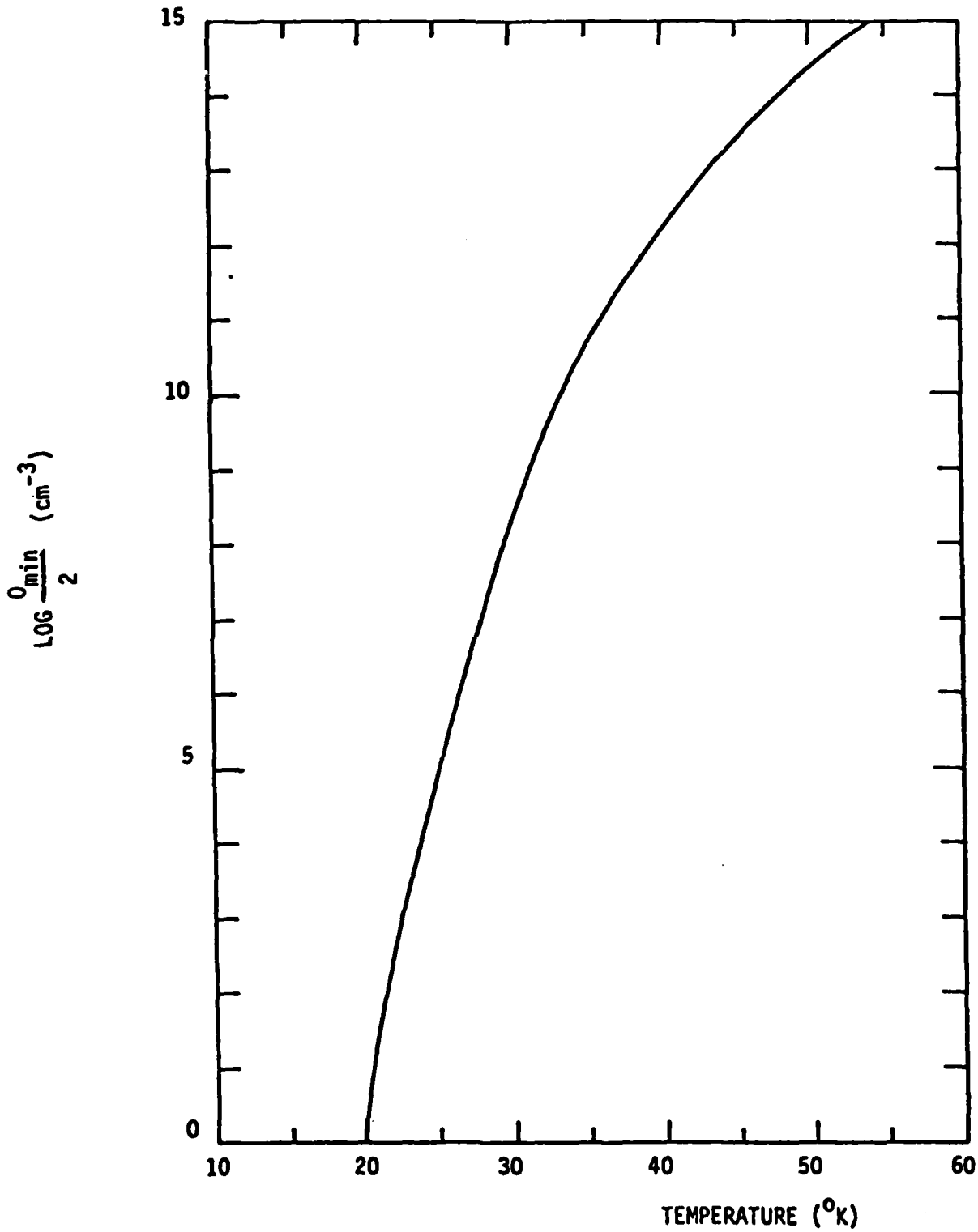

Figure 17. Minimum Q Required for Coating Buildup

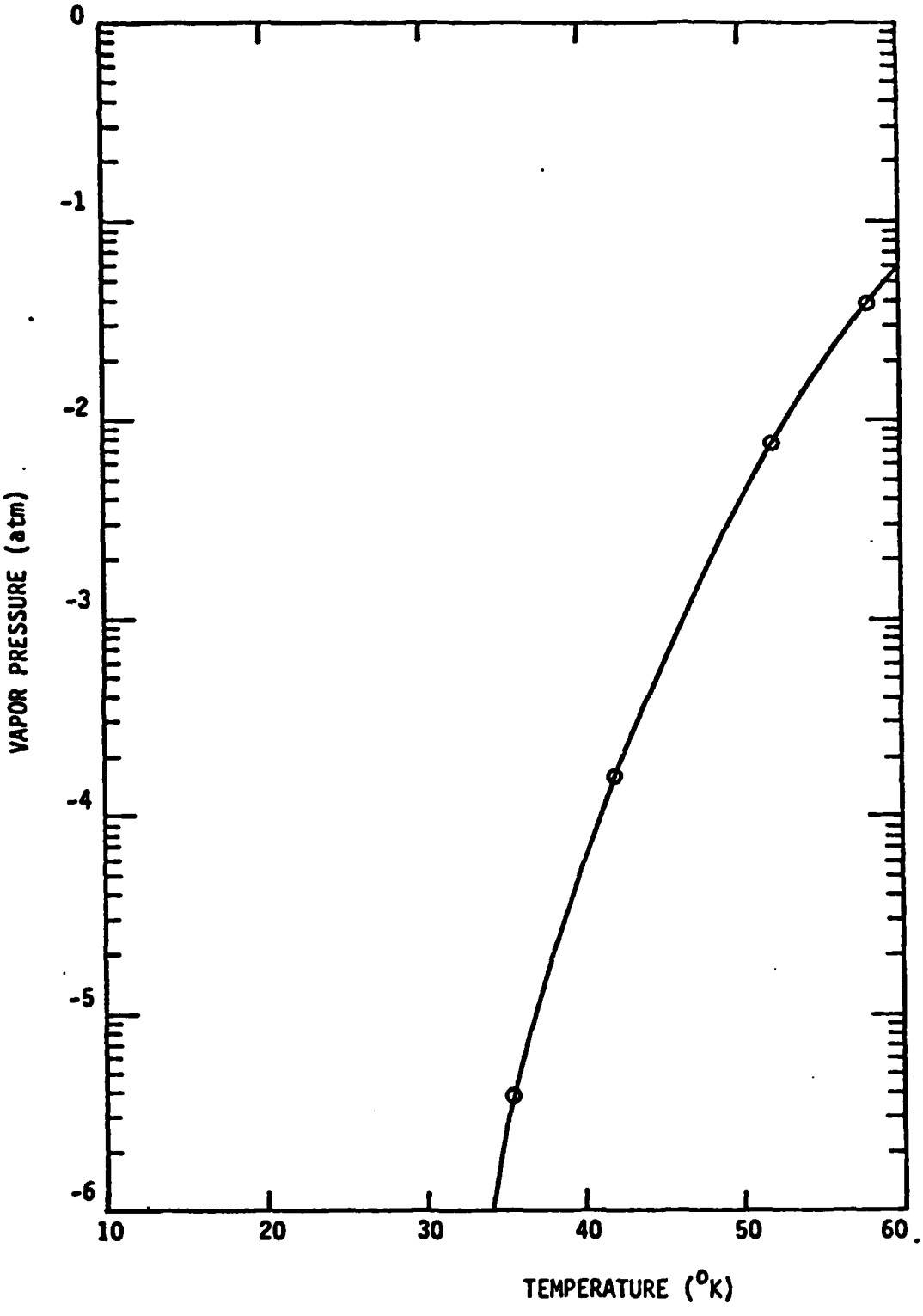

Figure 18. Nitrogen Vapor Pressure vs. Temperature

Ambient He and H - Figures 19 and 20 show the low temperature vapor pressures for hydrogen (normal boiling point 20.129°K) and helium (normal boiling point 4.216°K)[10]. The vapor pressure of these gases is high, so that is not a problem for the mirror temperatures we are considering.

2.6.2.2 Spacecraft Generated Gaseous Contamination

At 650 kilometers altitude and higher, the maximum ambient density occurs during periods of high solar activity and is less than 10^8 cm^{-3} (Figure 14). The mean free path for a collision with an ambient molecule is on the order of 100 kilometers, and in the vicinity of the spacecraft, vapor produced by outgassing will move with the spacecraft. If the contaminant density in the vicinity of the spacecraft is n, then the rate at which the contaminant vapor will deposit on a surface is

$$\text{Deposition rate} = \frac{a\, n\, \bar{v}\, m}{4T} \ (gm/cm^2\text{-sec})$$

where

a = the accommodation factor (fraction of molecules incident on a surface which adhere to it)

$\bar{v}$ = mean velocity of gas molecules or atoms

T = temperature in °K

In general, the gaseous contaminants that are bothersome are condensable gases such as water vapor, CO_2, various solvents used in spacecraft fabrication, etc. At the mirror temperature, it is assumed these gases will condense and that varporization will be negligible. However, the effect of these gases can be reduced by pumping within the baffle walls.

Figure 21 illustrates the geometry for baffle pumping. If the particles are isotropically distributed, the fraction of the particle entering the telescope aperture which strikes the mirror without first

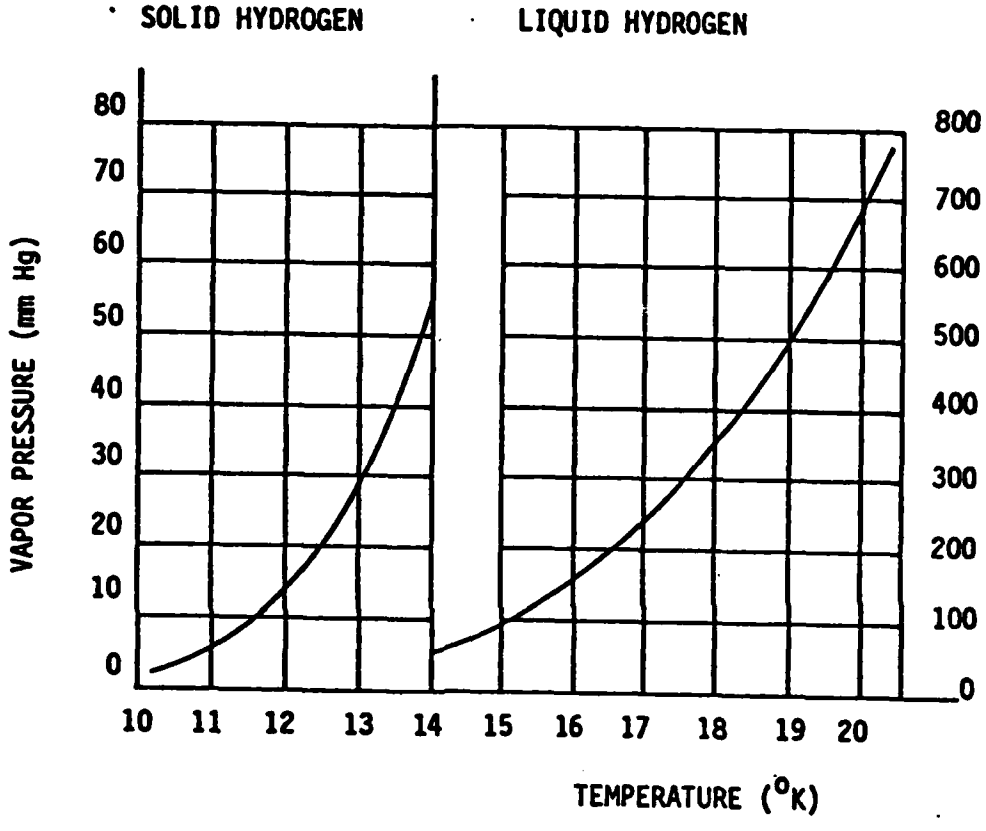

Figure 19. Vapor Pressure of Hydrogen

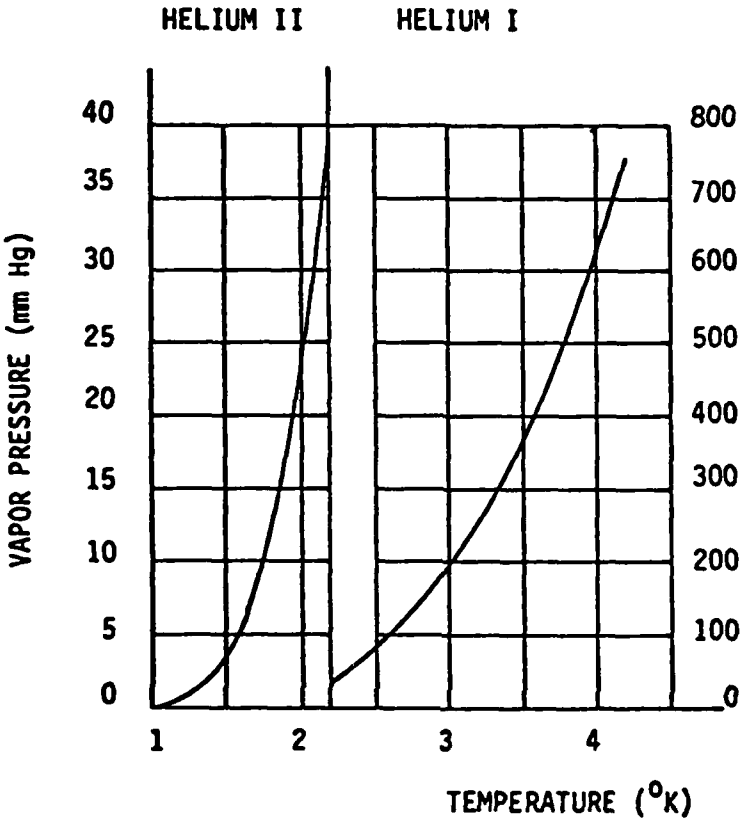

Figure 20. Vapor Pressure of Helium

CRYOGENICALLY COOLED BAFFLE WALLS

TELESCOPE ENTRANCE APERTURE

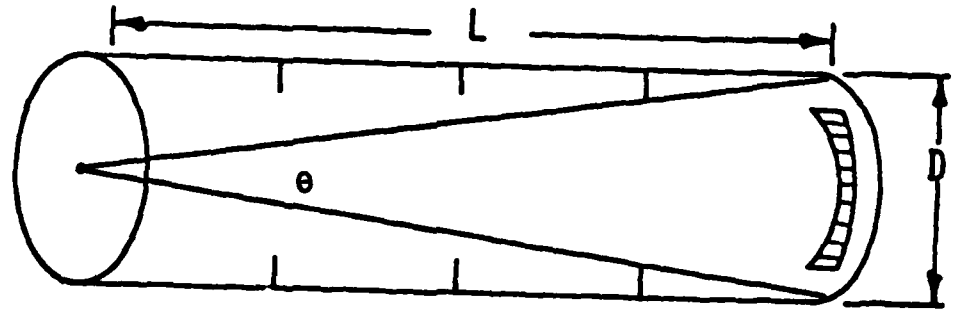

COLD PRIMARY MIRROR

FOR VALUE OF $\theta > D/L$ CONTAMINANT IS CRYOPUMPED

FRACTION STRIKING MIRROR $\frac{D^2}{4L^2}$

Figure 21. Cryopumping with Cooled Baffle

striking the baffle is $D^2/4L^2$. For a D/L ratio of 1/5, the vapor striking the optical surface is four percent of the vapor entering the aperture.

Figure 22 shows the capture, or accommodation, coefficient for several atmospheric gases as a function of gas temperature and surface temperature[11]. The coefficient is defined as the condensation probability per collision on the cryosurface for molecules having an average energy equivalent to the gas temperature. Only one surface temperature was measured for O_2, but since with the other gases, the coefficient is nearly independent of cryosurface temperature, this value is assumed for all surface temperatures of interest. The measured accommodation coefficient for oxygen was unity for a kinetic temperature of 77°K and .86 for a kinetic temperature of 300°K. Clearly , any significant vapor pressure of these gases will present a contamination problem.

2.7 Summary of Contaminant Environment

State of the art high straylight rejection IR telescope employ an off-axis reimaging optical configuration that can be readily baffled optically. The primary mirror is often a conic surface of revolution other than a flat surface. The representative sensor telescopes like ZIP and CIRRIS use primary mirrors that exhibit BRDF at 10.6 um of 1×10^{-4} sr^{-1} at 1° off specular and rolls off as θ^{-2} where θ is the off specular angle. Assuming that this level of mirror scatter has to be maintained for a period of four years, the following contaminant environments should be addressed.

Prelaunch

The primary mirror has to be free of film and dust prior to launch unless one has a provision to clean the mirror on orbit. In situ BRDF measurement of clean mirrors contaminated by black paint (Z306/9922), clear adhesive (M-773), or MLI did not show any measurable increase of BRDF at 10.6 um for deposition thickness up to 0.11 um (see Reference 3). Oxygen cryodeposits of several um will significantly degrade the BRDF of a

Cryosurface temperature (°K)	N_2		A		CO_2	
	77°K	300°K	77°K	300°K	195°K	300°K
10	1.0	0.65	1.0	0.68	1.0	0.75
12.5	0.99	0.63	1.0	0.68	0.98	0.70
15	0.96	0.62	0.90	0.67	0.96	0.67
17.5	0.90	0.61	0.81	0.66	0.92	0.65
20	0.84	0.60	0.80	0.66	0.90	0.63
22.5	0.80	0.60	0.79	0.66	0.87	0.63
25	0.79	0.60	0.79	0.66	0.85	0.63
77					0.85	0.63

Cryosurface temperature (°K)	CO		N_2O		O_2	
	77°K	300°K	195°K	300°K	77°K	300°K
10	1.0	0.90	1.0	0.63		
12.5	1.0	0.85		0.62		
15	1.0	0.85	0.94	0.62		
17.5	1.0	0.85		0.61		
20	1.0	0.85	0.86	0.61	1.0	0.86
22.5	1.0	0.85		0.61		
25	1.0	0.85	0.85	0.61		
77				0.61		

Figure 22. Accommodation Coeffecients of Common Gases

clean low scatter mirror. Surface cleanliness of better than Level 100 has to be maintained so that particulate scatter will be lower than mirror scatter levels.

The interior surfaces of the telescope must be devoid of particulates as much as possible.

Launching

The launching and insertion of the sensor/spacecraft into orbit involves acceleration and vibration. Particles inside the telescope can be dislodged during this period of time and come into contact with the primary mirror through a number of transport steps. Spacecraft exterior surfaces can be severely contaminated during this phase. Generally, the sensor cover should be closed throughout this period. Once on orbit, the cover may still be closed for some time until initial sensor outgassing rate is reduced to a manageable level.

On Orbit

During the mission lifetime, sometimes as long as four years, atmospheric gas species, as well as sensor/spacecraft-generated gas species, may condense on the cryogenic optical/mechanical surfaces. For 1976 standard atmosphere, the oxygen cryodeposit thickness is 0.35 um per four years at 1,000 km at nominal solar activity. It increases to 350 um at maximum solar activity. The deposition will be 0.00012 and 0.12 um for the 10,000 km altitude for nominal and maximum solar activities, respectively. The above estimate assumes mirror sticking coefficient of unity, atomic oxygen recombines into oxygen molecules O_2, and the sensor LOS points along velocity vector always.

The assessment of MLI outgassing contaminants is more difficult. Since 99.5 percent of the outgassed species will be water vapor, it may present significant cryodeposit problems if the MLI is allowed to vent directly into the baffle and/or toward the primary mirror. Due to the low

atmospheric density and long mean free paths at 1000 km and much more so at 10,000 km altitude, backscattering of outgassed water vapor is minimal. If the MLI is vented at the back (i.e., opposite to the sensor aperture opening side) of the sensor, the water vapor has to be scattered by other surfaces before it can come in through the sensor aperture.

Exterior surfaces on sensor payload will have some attached particles. Various mechanisms can initiate the release of these particles. Examples include the impact of micrometeoroid and bursting of bubbles of trapped gas.

3.0 IACS DESIGN ISSUES AND CANDIDATE CONFIGURATIONS

3.1 Ion Pumping Mechanisms

In the preceding sections we have considered methods which reduce the contamination of optical surfaces produced by the condensation of ambient gases and spacecraft outgassing. The effectiveness of these approaches will depend on the orbital parameters, the temperature of the optics, and the nature of the outgassing material. We will now consider the addition of an Ion Anti-Contamination System (IACS).

The concept of the workings of an IACS can be broken down into three steps:

(1) Gas contaminants are ionized in localized region between entrance aperture and optics.

(2) Ionized contaminant molecules are swept out by electric field perpendicular to optical axis.

(3) These molecules are deposited on cryogenic surfaces which are optically baffled from telescope optics and are held there as long as these surfaces are kept at cryogenic temperature.

A schematic of an IACS is illustrated in Figure 23. An artist's visualization of the basic concept is shown in Figure 24.

The mechanism we are considering is electron collisional ionization of the incident gas and subsequent electric field removal of the ions to the baffle wall. The device we are considering is similar in concept to a VacIon pump. Figure 33 illustrates the basic concept. A negative voltage is applied to the central cathode and the cylindrical anode is grounded. Assuming an initial ionization (e.g., by cosmic radiation), the ion will move directly to the cathode under the influence of the applied electric field while the electron will be constrained by the magnetic field to follow a cycloidal path. Both particles are, in fact, affected by the magnetic field, however, the radius of gyration is directly

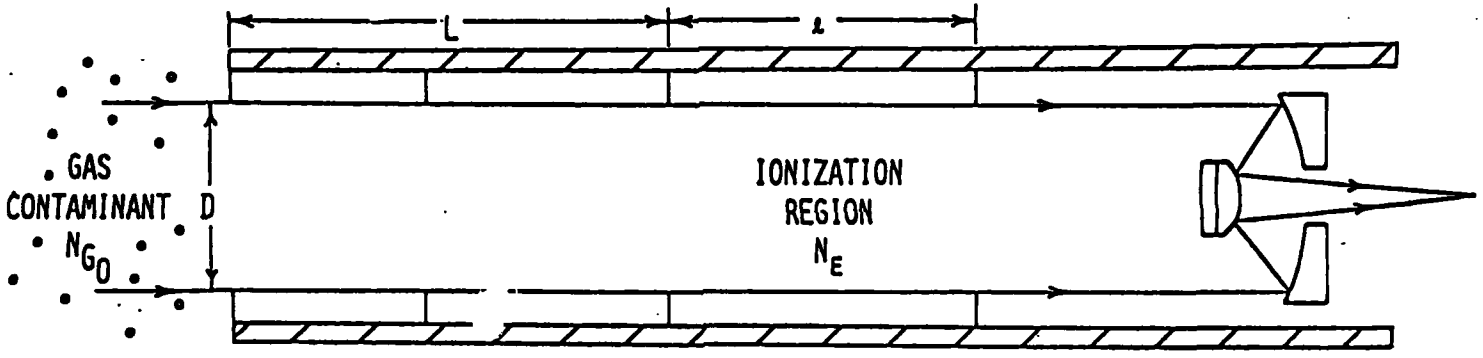

N_{G_0} - CONTAMINANT DENSITY AT FRONTAL BAFFLE (cm^{-3})

D - DIAMETER OF BAFFLE OPENING (cm)

A - CROSS SECTIONAL AREA OF BAFFLE OPENING $\frac{\pi D^2}{4}$ (cm^2)

L - LENGTH FROM APERTURE TO IONIZATION REGION (cm)

ℓ - LENGTH OF IONIZATION REGION (cm)

Figure 23. Schematic of Ion Anti-Contamination System

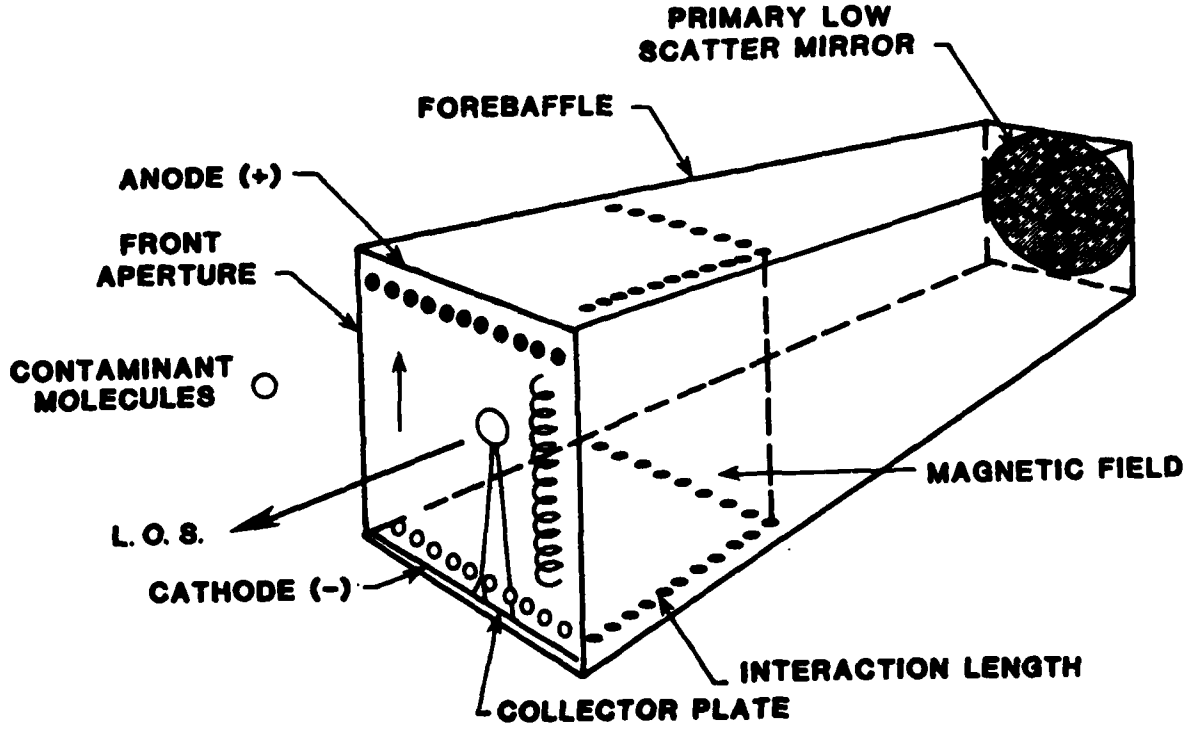

Figure 24. Ion Anticontamination System

proportional to the mass; and the mass (and therefore the Larmor radius) of an H_2O ion is 3.3×10^4 larger than that of an electron. In order to move rapidly to the anode, the electron must collide with the ambient gas. At the normal operating voltage, a number of the collisions will be ionizing and electron multiplication will take place. Subsequently, the electron avalanche will migrate to the anode and additional electrons will be produced at or near the cathode by such mechanisms as ion recombination on the walls, photoelectron production, field emission, etc. The desired operating condition is a self-sustaining series of avalanches, and this is the normal mode of operation of a VacIon pump. However, it can be readily seen that there is a space charge limit on the electron density, and that limit occurs when the potential due to the electron cloud is equal and opposite to the applied potential. The maximum electron density is

where $$[N_e]_{max} = \frac{16E_o V}{D^2 e} \quad (\text{electrons/m}^3)$$

E_o = 8.85×10^{-12} c2/n m2
V = Voltage between anode and cathode (V)
D = Diameter of cathode (m)

The electron density then is proportional to the ratio of the applied voltage to the square of the cathode diameter.

3.2 Effectiveness of Ion Pumping in the Optical Path

Consider the top configuration shown in Figure 25. As the contaminant gas flows through the plasma region, it will be ionized and removed by a superimposed electric field. The fraction, F, of the incident gas that traverses the plasma region un-ionized (and therefore, that fraction that can coat the optics) is given by

$$F = e^{-(\sigma N_e v_e l / v_g)}$$

where

σ = ionization cross section (σ is 4×10^{-10} cm^2 for ionization of H_2O by a 1 keV electron)

N_e = electron density (cm^{-3})

v_e = mean electron velocity (2×10^9 cm sec^{-1} for a 1 keV electron)

l = length of the plasma region along the baffle axis (cm)

v_g = mean gas velocity along the optical axis ($cm\text{-}sec^{-1}$)

If we take l to be 40 inches (100 cm) and use the values given above for 1 keV electrons on H_2O, then

$$\ln F = -8 \times 10^{-6} \frac{N_e}{v_g}$$

The anticipated gas flow velocity, v_g, will be in the range of 1 to 5×10^4 $cm\text{-}sec^{-1}$. The following table evaluates F as a function of electron density and v_g:

	F		
v_g (em-sec^{-1})	$N_e = 5 \times 10^9$ cm^{-3}	10^{10} cm^{-3}	2×10^{10} cm^{-3}
$v_g = 10^4$	1.8×10^{-2}	3.4×10^{-4}	1.1×10^{-7}
2×10^4	1.4×10^{-1}	1.8×10^{-2}	3.4×20^{-9}
5×10^4	4.5×10^{-1}	2×10^{-1}	4.1×10^{-2}

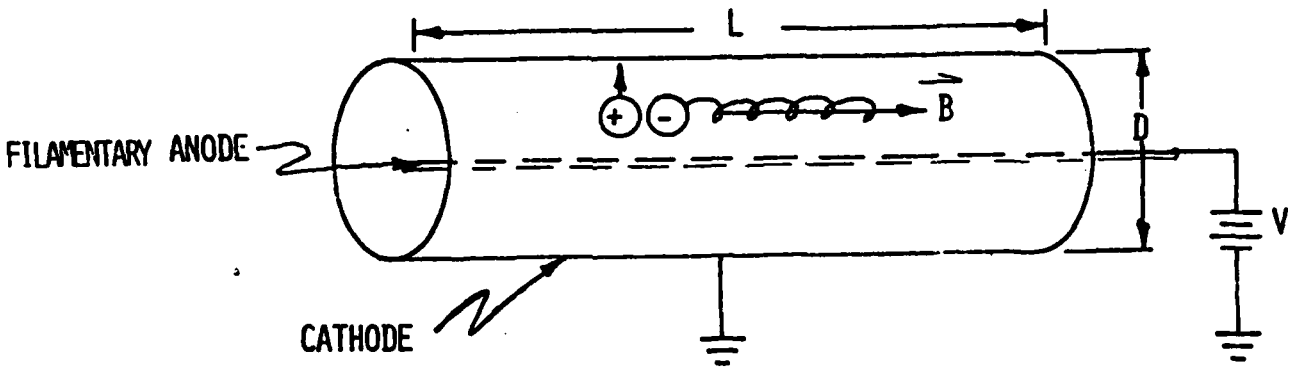

MAGNETIC FIELD PARALLEL TO CYLINDRICAL AXIS

IONS FORMED GO DIRECTLY TO CATHODE

ELECTRONS TRAPPED BY MAGNETIC FIELD

SPIRAL WITH RADIUS $= \frac{MV}{eB}$

KILOVOLT ELECTRONS $R = \frac{1.1 \times 10^{-1} \text{ cm}}{\text{KILOGAUSS}}$

SPACE CHARGE LIMITS ELECTRON DENSITY

$$[N_E]_{MAX} = \frac{16 \varepsilon_o V}{D^2}$$

Figure 25. Electron Ionization Pumping

The exponential dependence of F on the ratio N_e/V_g is obvious from the table. The basic problem in the instrument design is to produce a region of high electron density ($\sim 2 \times 10^{10}$ cm^{-3}) in the optical path.

Other parameters that affects the efficiency are ionization cross section, mean electron velocity, mean gas velocity along the optical axis, and the interaction length.

The ionization cross section decreases as the electron energy increases so that the product of the ionization cross section and mean electron velocity is approximately constant. (Figure 26). The effects of varying the other parameters are discussed below.

3.3 Interaction Length & Forebaffle Conductance

Increasing the interaction length would increase the dwell time thus the pumping efficiency at a specific electron density. However, the interaction length is limited by the maximum volume of the baffle system as well as the maximum power consumption.

The mean gas velocity along the optical axis can be reduced by placing a tubular section in front of the ionization region. This is because at these sensor altitudes the gas flow is molecular flow so that the conductance of the tubular region will reduce the gas fow rate into the ionization region. For example, a section of a length to diameter ratio of 1 and 2 can reduce flow to 51% and 36% respectively. Therefore, the net deposition on the mirror will be reduced accordingly. If the baffle is cold enough to cryopump the gas contaminats, the flow rate is further reduced.

3.4 IACS Candidate Configurations

The configuration shown in Figure 25 performs two of the three functions required for IACS. It provides a stable electron trapping region and a mechanism for removal of the ions. However, the ions on reaching the

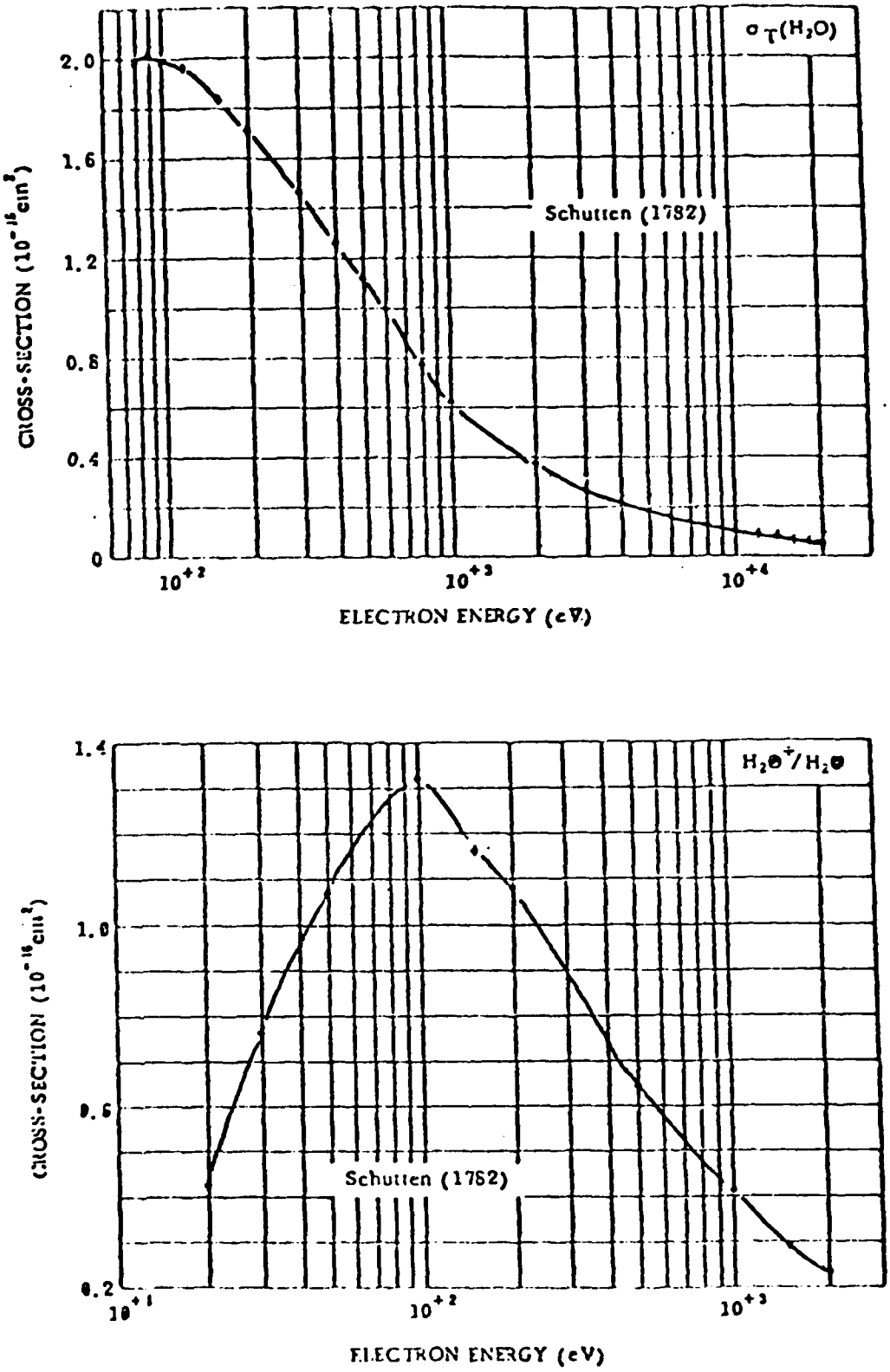

Figure 26. Electron Energy (eV)

cathode are neutralized and unless something else is done they are returned to the gaseous state. Commercial VacIon pumps use a large titanium cathode with which the active ions will chemically react and in which nonactive species (H, He, and Ar) can diffuse or be buried. In addition, the impinging ions continually sputter a fresh coat of titanium within the pump with which neutral active gases will react. Additional pumping capacity can be achieved by sublimating (thermally evaporating) titanium onto the pump wall. Significantly higher pumping speeds can be obtained by sublimating the titanium onto cryogenically cooled walls.

In order to incorporate titanium sputtering effectively, the cathode design must be modified from that shown in Figure 25. Figures 27 and 28 are a schematic and an isometric drawing of a standard VacIon pump. The anode is cylindrical with two flat plates for a cathode while the radial electric field is maintained by two small cylindrical cathodes extending inside the cylindrical anode. The superimposed magnetic field is parallel to the anode axis. This particular pump which has a pumping speed of two liters per second is operated at 3500 Vdc and uses a 1200 gauss magnetic field for electron containment.

Figure 29 illustrates conceptually the two configurations we have considered. In the first, the ionization region is in the primary optical path of the beam. In the second, the ionization region is in the walls of the baffle, a region that is not viewed by the telescope. The principal advantage of pumping in the optical path is that all the gas entering the telescope goes through the ionization region. This approach is discussed in Section 3.4.1. The peripheral pump has the advantage of being out of the optical line of sight of the telescope. In this case, any radiation produced in the ionization region can be removed using conventional stray light suppression techniques. The preliminary evaluation of the radiation question is positive; that is, the identified radiation sources will not degrade the optical performance. However, this preliminary evaluation cannot be considered definitive. The peripheral pump design is discussed in Section 3.4.3. Section 3.5 discusses the magnetic field required for containment and weight and power budgets for various types of magnets.

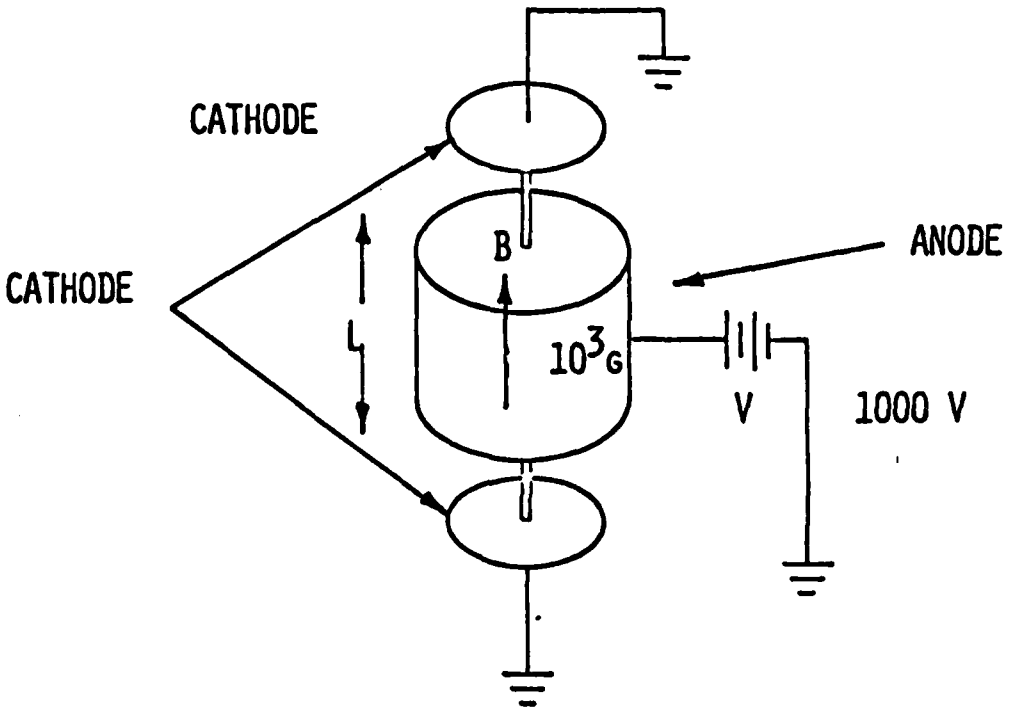

Figure 27. Ion Pumping Concept

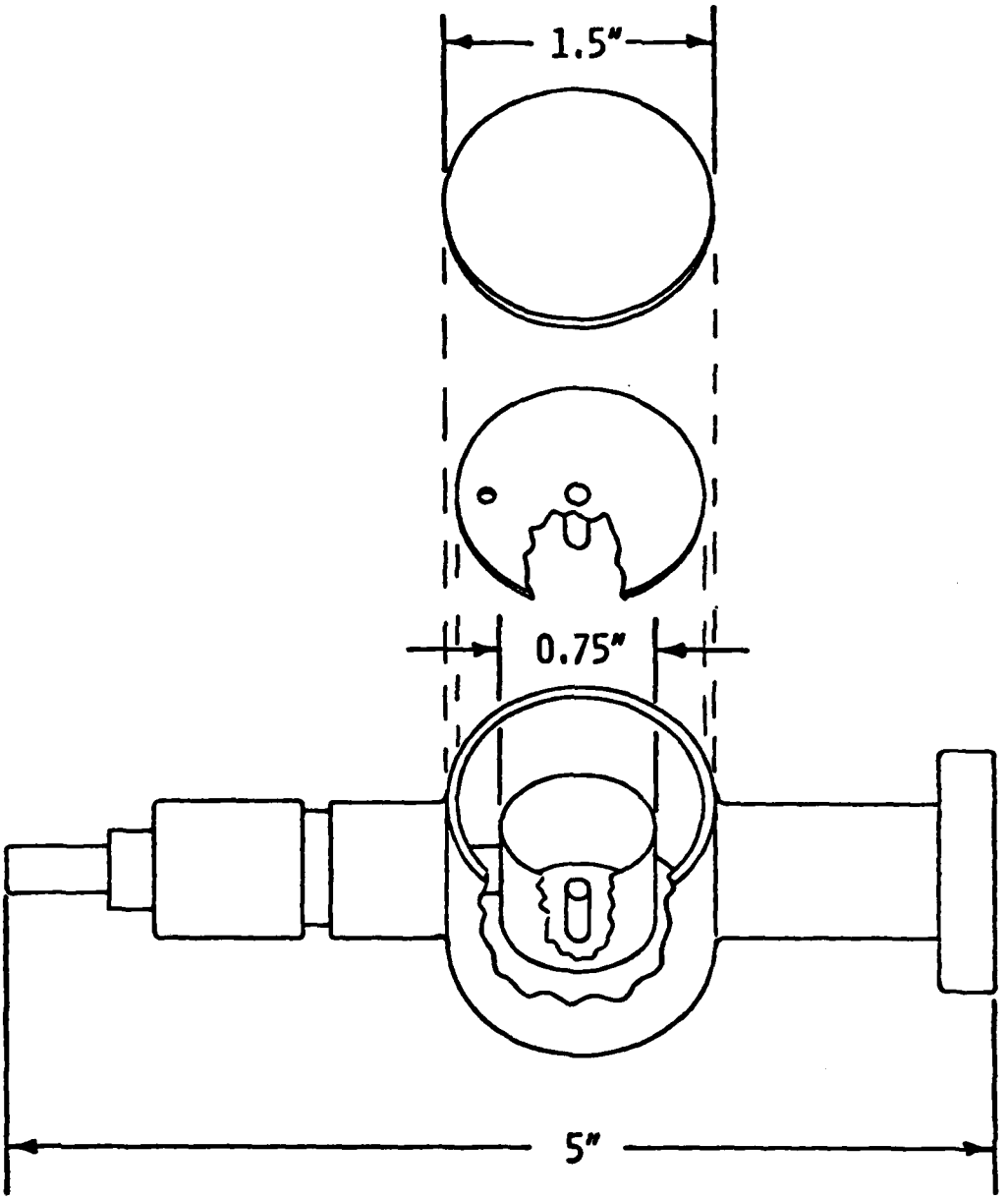

Figure 28. VacIon Appendage Pump

PUMPING IN OPTICAL PATH

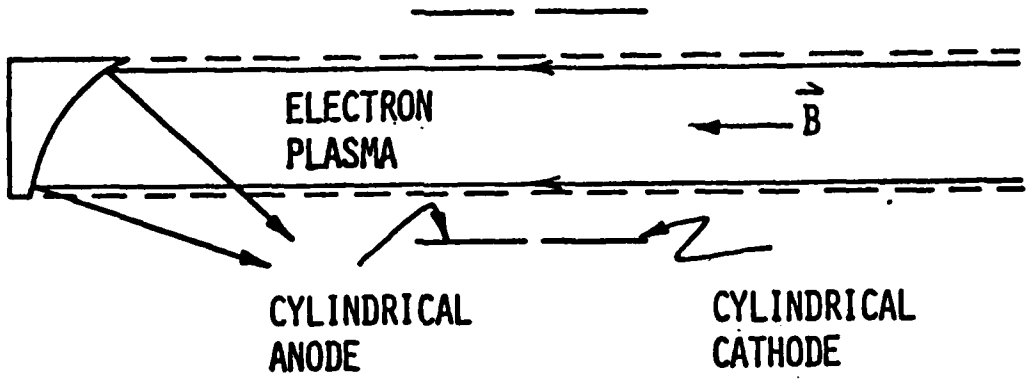

PUMPING IN BAFFLE WALLS

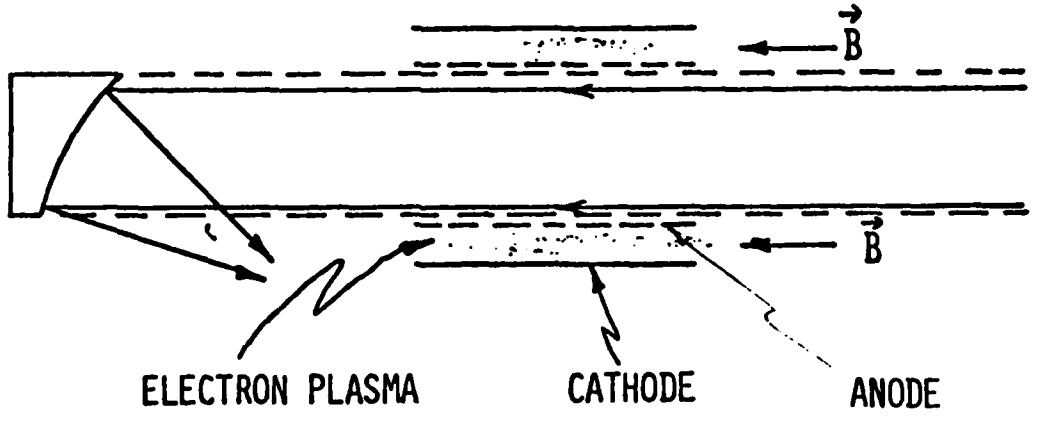

Figure 29. Possible Pump Configurations

3.4.1 Circular Aperture Pump (Configuration 1)

In the previous section, the maximum election density inside a filamentary cathode was given as

$$[N_e]_{max} = \frac{16\epsilon_o V}{D^2 e} \quad \text{electrons/m3}$$

or

$$\frac{8.5 \times 10^8 V}{D^2} \quad \text{electrons/m}^3$$

For the densities we are considering (2×10^{16} electrons/m^3), V/D^2 must be at least 2.4×10^7 V/m^2.

For a reasonable operating voltage (ten of kilovolts), the maximum anode diameter is a few centimeters. If we scale up the device shown in Figure 27 to a cathode diameter of 20 cm, the operating voltage would be in excess of 300 kV. The feasibility of operating these devices at such high voltages is open to question. Since standard commercial devices operate at electron densities of less than $10^{10} cm^{-3}$, even higher voltages may be required to reach the desired electron densities. In addition, a novel anode cathode design is required for this type of pump since the elements may not intrude into the optical path. Such a configuration is shown conceptually in Figure 30. A more detailed study is required to evaluate the electron density obtainable with this configuration. One potential advantage of such a scaled up device is that the required magnetic field scales inversely with the cylinder diameter. The required magnetic field is then on the order of a hundred gauss.

The dependence of operating voltage and magnetic flux density on the optical aperture diameter are illustrated in Figure 31. The ion pumping device must have the optical diameter as a minimum inner diameter

- COOLED MAGNET 100 GAUSS FIELD OR
- SUPERCONDUCTING MAGNET - KILOGAUSS FIELD CONFIGURED TO TRAP ELECTRONS

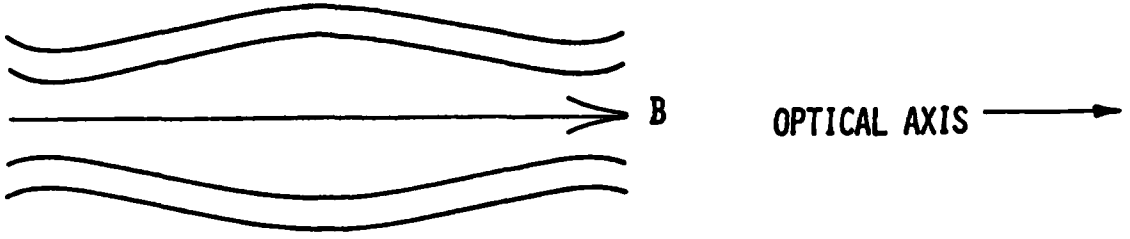

- CYLINDRICAL ANODE AND CATHODE

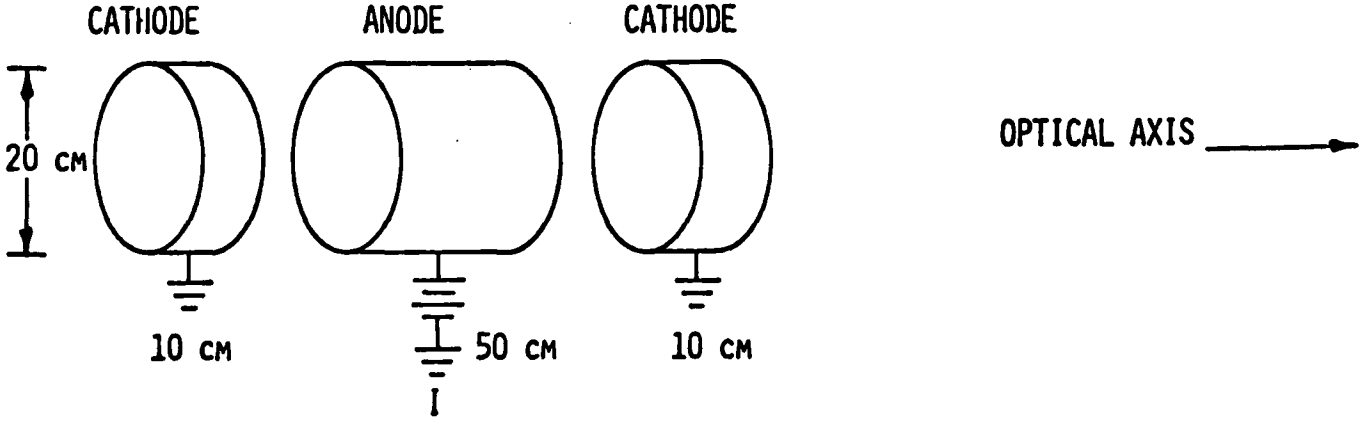

Figure 30. Conceptual Design of Axial Pump

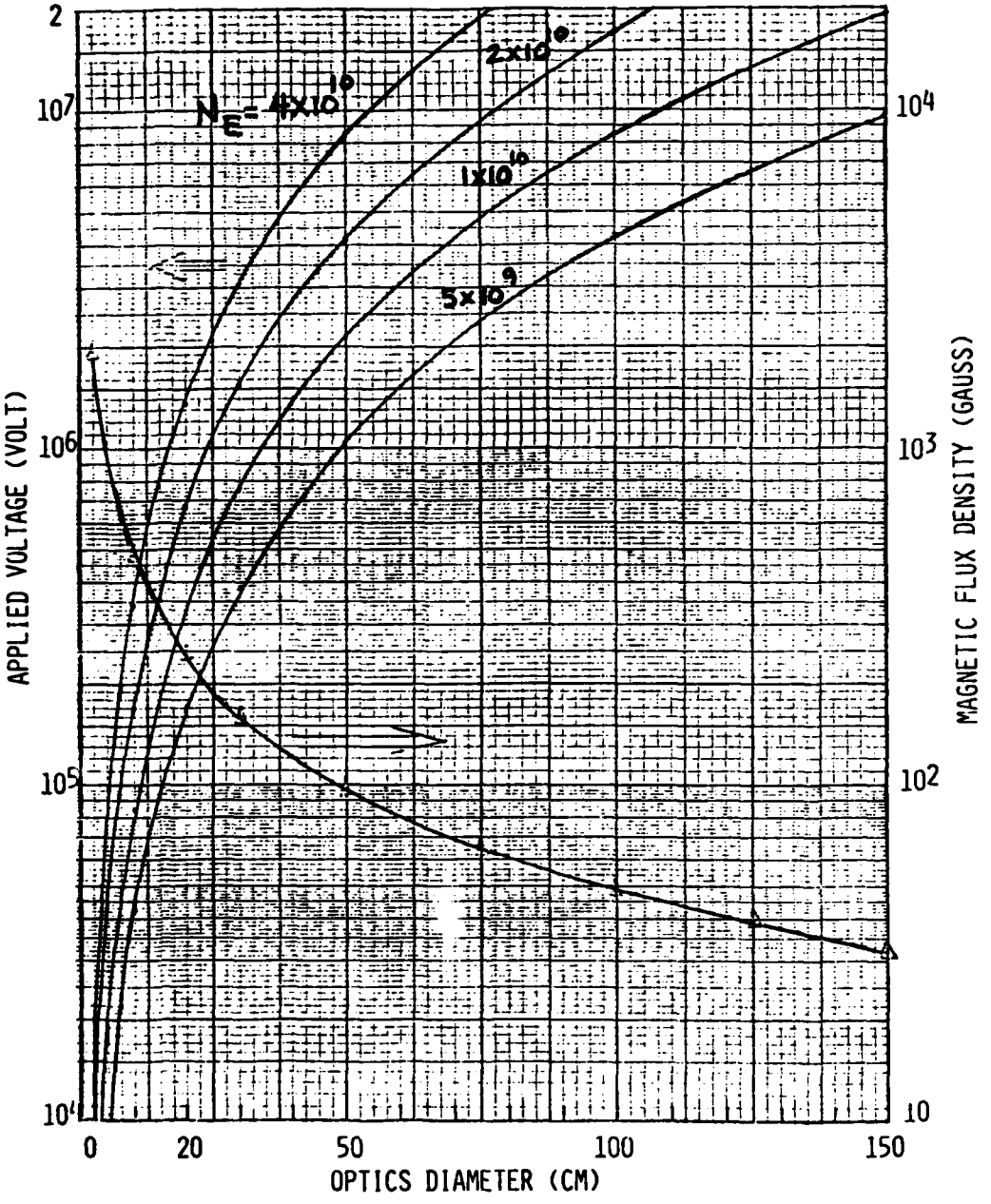

Figure 31. V & B vs. D (Circular Through Pump)

since no obstruction of the optical aperture is allowed. It is obvious from this figure.that for a moderate optical diameter of 20 cm, the operating voltage will be 700 kilovolt for electron density of 2 X 10^{10} cm^3, and the magnetic flux density will be 300 gauss.

The highest electron density that was reported on this type of ion pump was 0.8 x 10^{10} cm^3 at operating pressure of 10^{-5} torr. A factor of 2.5 increase is considered a reasonable extrapolation. Figure 32 shows the election density dependence on operating pressure for a device diameter of 2.54 cm. It is evident that the electron density can be stable over at large pressure range from 10^{-5} down to 10^{-10} torr for various applied voltage. The electron density versus applied voltages is cross plotted in Figure 33. An equivalent applied electric field is also included.

For nominal electron density of 2 X $10^{10}cm^{-3}$ and 1 KeV electrons, a one percent transmission efficiency can be obtained if the gas molecules dwell in the ionization region for 2.88 milliseconds. Figure 34 illustrates the trade off between interaction lenth and the maximum gas velocity that can be effectively pumped. Figure 35 summarizes the parameters for a 8 inch diameter aperture and a 40 inch diameter aperture design.

3.4.2 Rectangular Aperture Through Pump (Configuration 2)

The second IACS configuration is a novel pumping arrangement which may provide the required electron density without the very high voltages. This arrangement is suitable for a rectanular aperture. Essentially, one has taken the standard ion pump single cell configuration and cut the pump into two halves such that each half-pump has a cylindrical anode and a cathode. (See Figure 36). A number of these half-pumps are stacked side-by-side to form a closely packed array. Two arrays are placed one above and one below the rectangular optical aperture along the baffle such that each half-pump will be directly opposite another one on the other side. The magnetic field will be directed parallel to the anode axes.

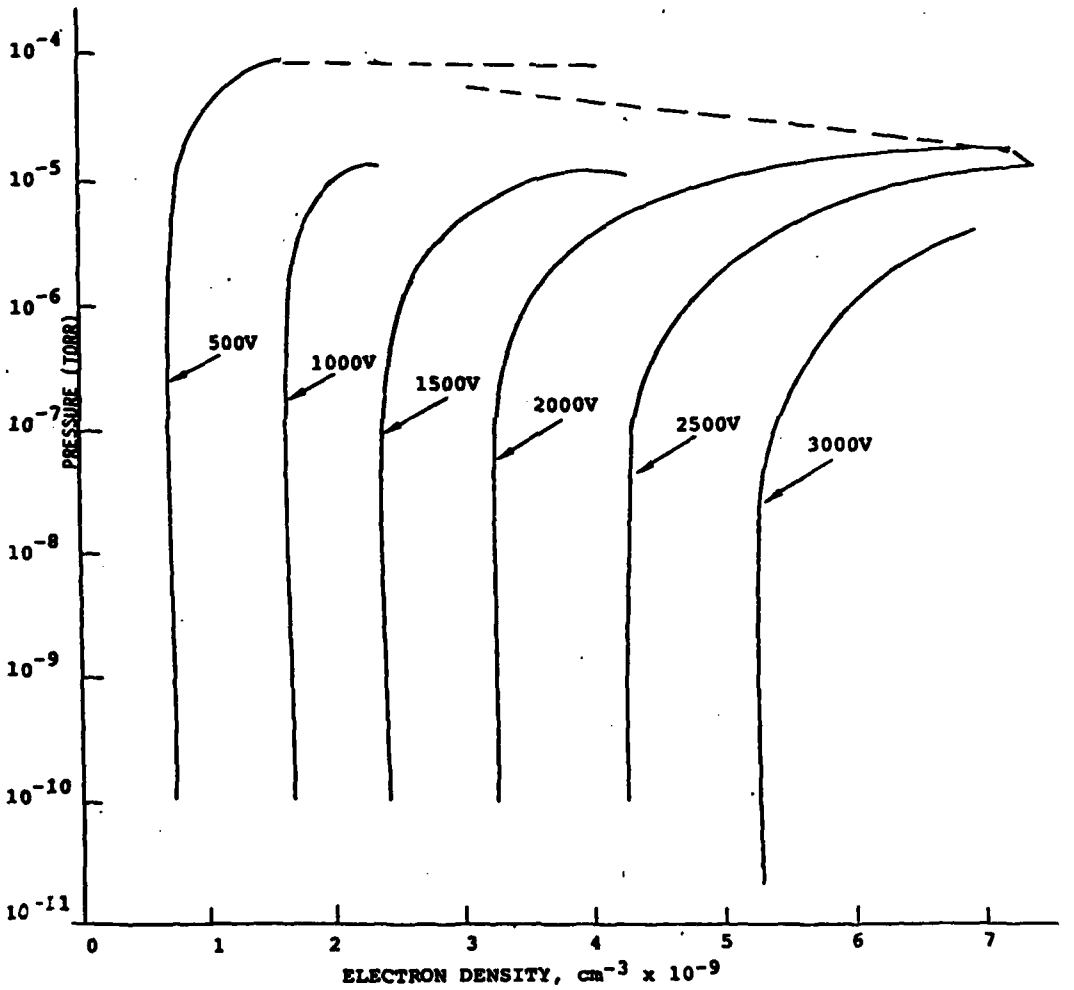

Figure 32. Electron Density as a Function of Pressure and Voltage (After Lange, W. J., J. Vac. Sci. Technol., Vol 7 No 1, 1969)

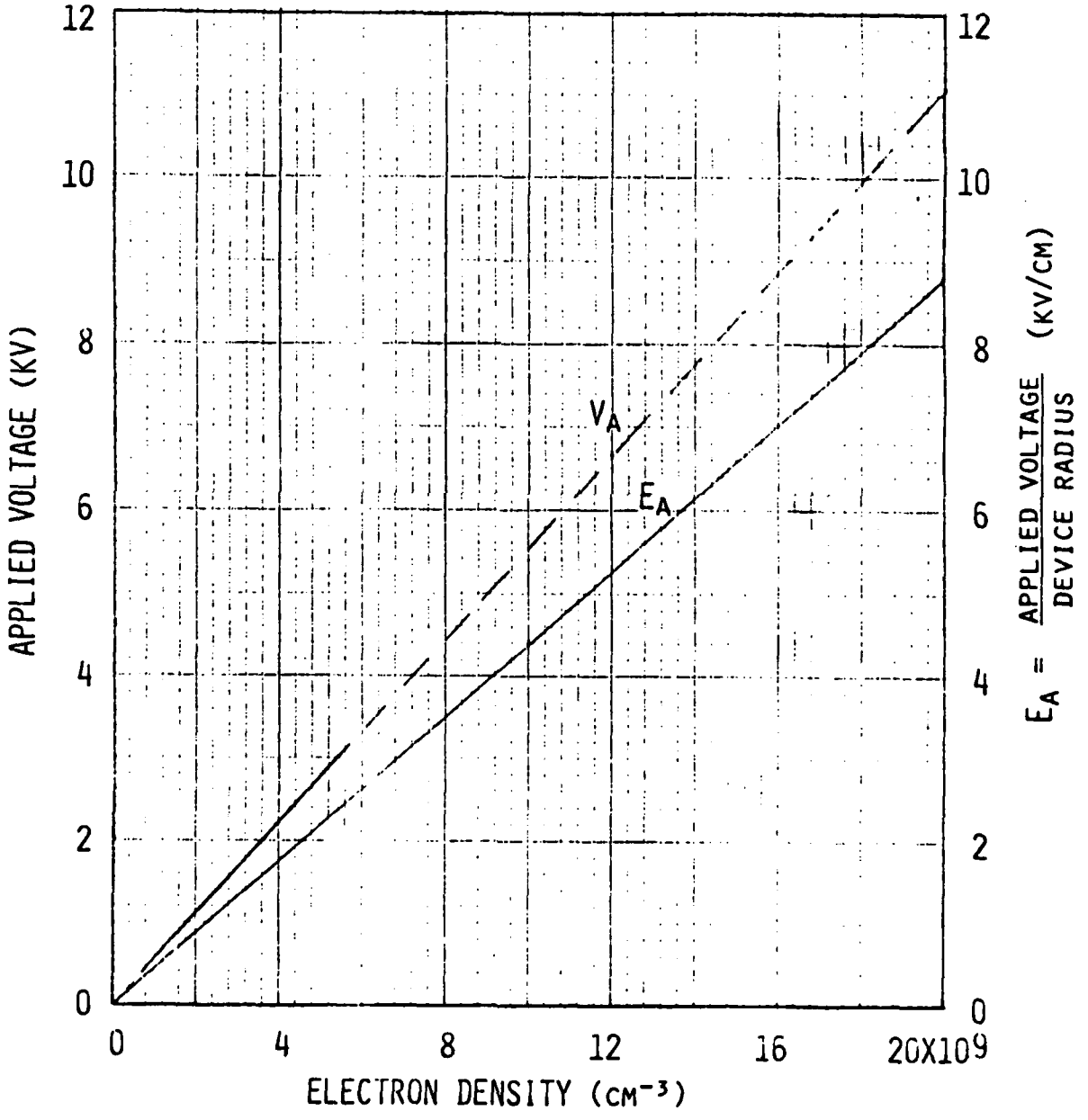

Figure 33. Electron Density as a Function of Field Strength

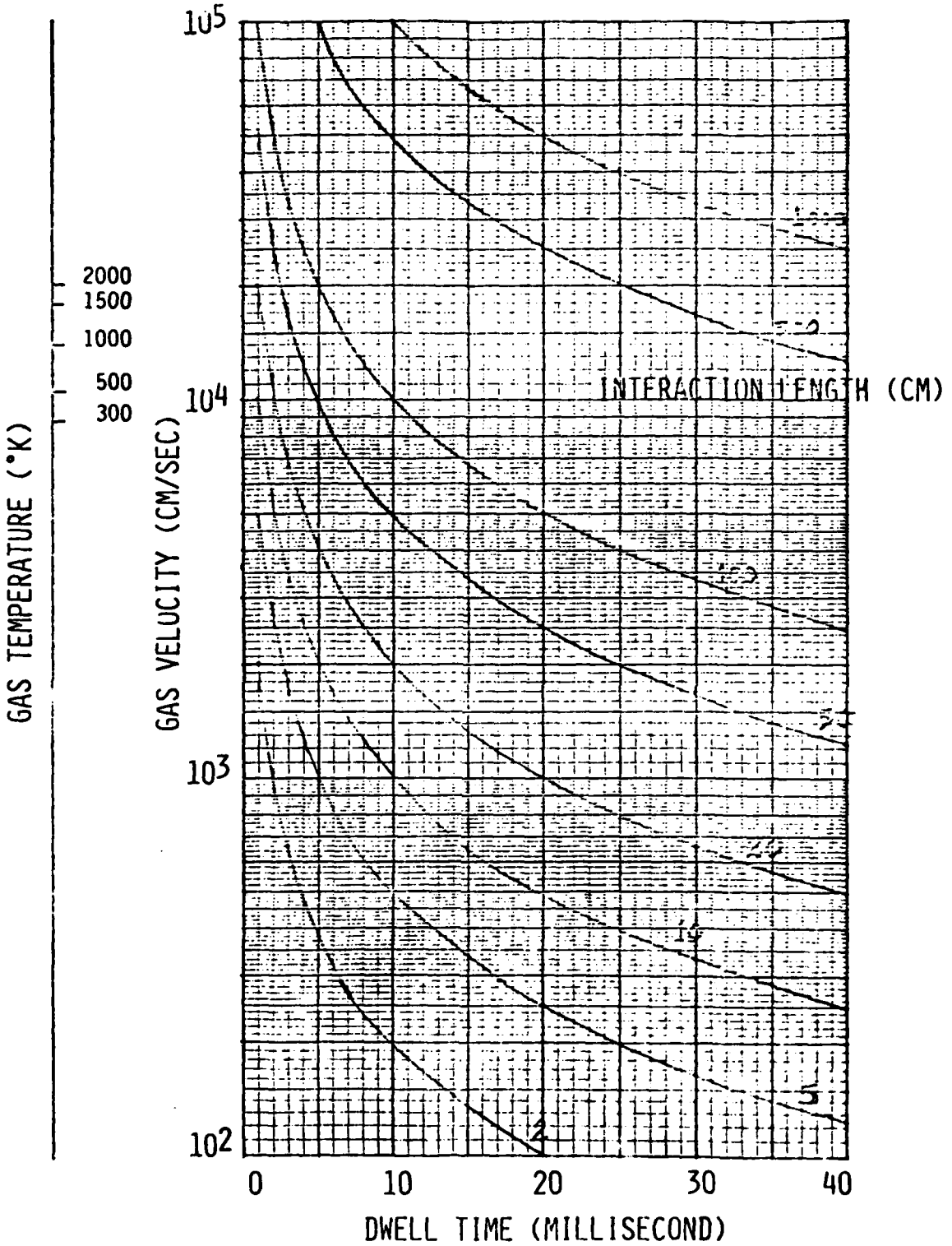

Figure 34. Dwell Time as a Function of Gas Velocity and Temperature

APERTURE	8 INCHES	40 INCHES
INTEGRATION LENGTH	40 INCHES	200 INCHES
MAX GAS TEMPERATURE	450 KELVIN	450 KELVIN
APPLIED VOLTAGE	700 KVOLTS	3400 KVOLTS
MAGNETIC FLUX DENSITY	242 GAUSS	48 GAUSS
POWER (10^{-7} TORR)	0.05 WATTS	0.09 WATTS
MAGNET TEMPERATURE	100 KELVIN	100 KELVIN
MAGNET POWER	100 WATTS	500 WATTS
MAGNET WEIGHT	220 LBS	510 LBS
		OPTIONS: SUPERCONDUCTING MAGNET: 0 POWER

Figure 35. Point Design - Through Pump

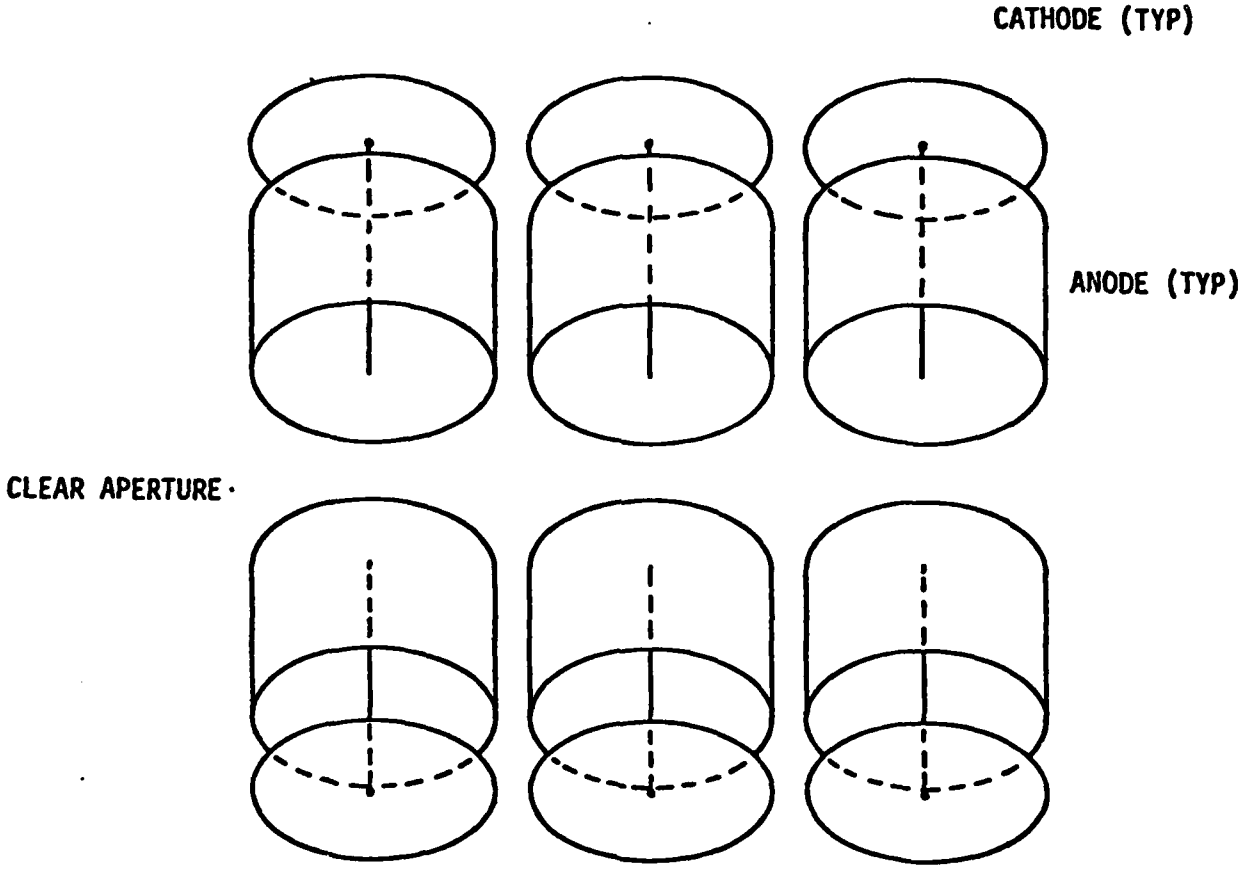

Figure 36. Ion Pump Array

Each half-pump will generate a dense electron cloud within the anode. The electron cloud will spill over into the gap between the diametrically positioned anodes and be constrained to a spiral path by the magnetic field, thus ionizing the gas molecules. A point design of this configuration for a rectangular aperture of 10 cm by 50 cm and measuring 100 cm long requires 87 KV and consists of 400 half-pumps. (See Figure 37). This IACS can provide attenuation of 10^{-2} for a gas kinetic temperature of 450 Kelvin. The electromagnet required for this configuration dissipates 250 watt if operated at 100 Kelvin. More detailed field calculations are required to further evaluate this concept.

Figure 38 summarized the parameters for a 4 inch by 20 inch as well as a 16 inch by 80 inch design.

3.4.3 Circular Aperture Peripheral Pump (Configuration 3)

This approach has two advantages. The pump region is outside the optical field of view, and therefore, conventional stray light rejection techniques may be used. In addition, all the incident atoms strike a surface which may be used as a getter. Use of the surface as a getter may allow one to operate at electron densities significantly less than in the case discussed in the previous section. Also, molecules reflected from a cold surface will undergo a loss of kinetic energy, and therefore a velocity loss.

Two configurations have been considered, one an annular cylinder shown in Figure 39, and the second, a peripheral array of pumps shown in Figure 40. Both configurations are relatively straightforward and provide comparable electron densities. For a potential difference of 3000 volts, the electron density in the configuration shown in Figure 39 is 3×10^{9} electrons cm^{-3}, while it is 4×10^{9} for the configuration shown in Figure 40.

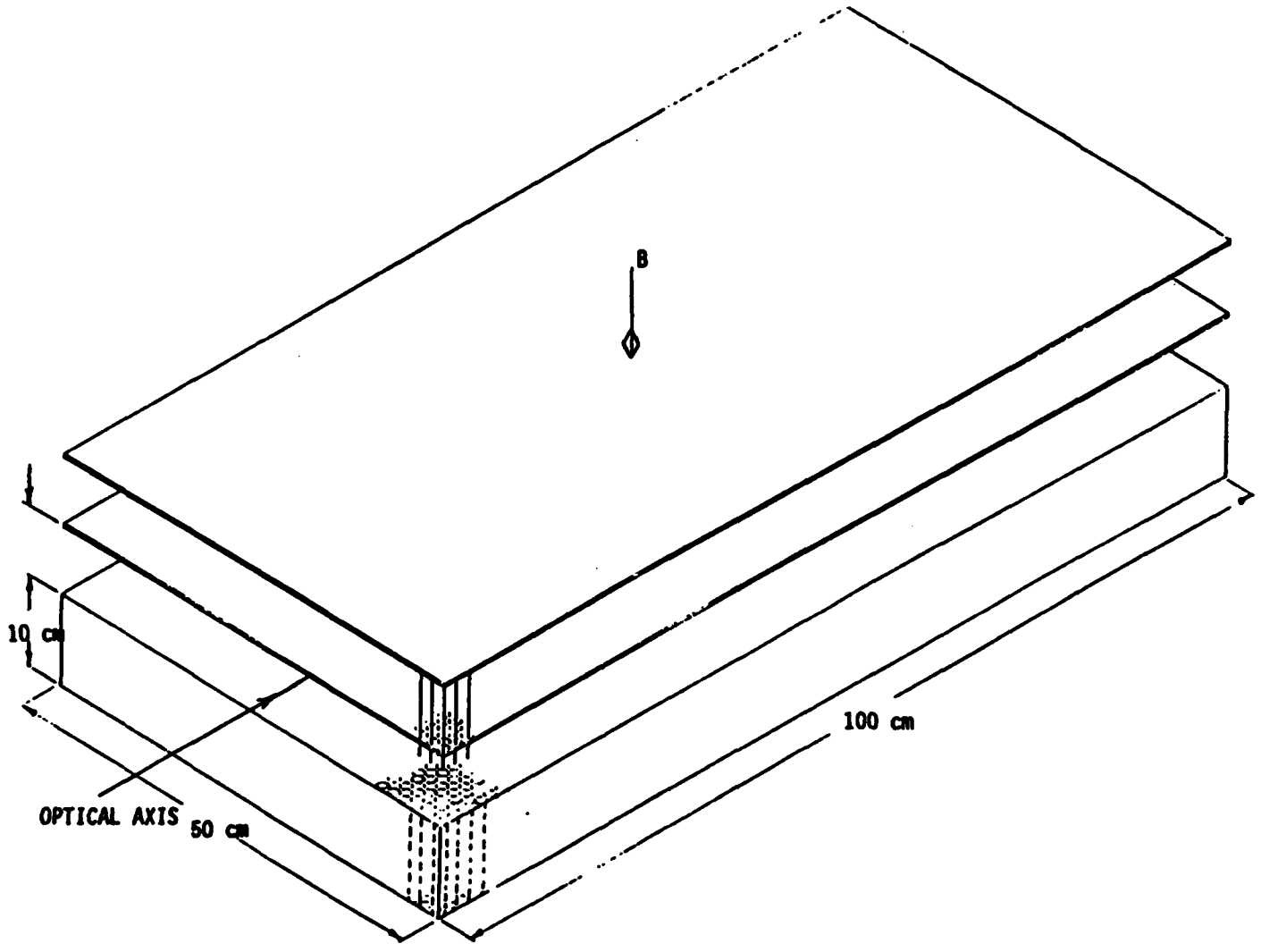

Figure 37. Rectangular Aperture Through Pump

APERTURE	4" X 20"	16" X 80"
INTERACTION LENGTH	40"	200"
MAX GAS TEMP	450	450
APPLIED VOLTAGE KV	87	338
MAG. FLUX DENSITY (GAUSS)	950	241
POWER (10^{-7} TORR)	0.7	2.6
MAGNET TEMPERATURE (°K)	100	100
MAGNET POWER (WATTS)	250	500
MAGNET WEIGHT LBS	TBD	TBD
EFFICIENCY	0.01	0.01
ANODE ELEMENT DIA X LENGTH	5 cm X 9 cm	10 cm X 6.8 cm
# ELEMENTS (TOTAL)	400	2,070

Figure 38. Ion System Point Design - Honeycomb

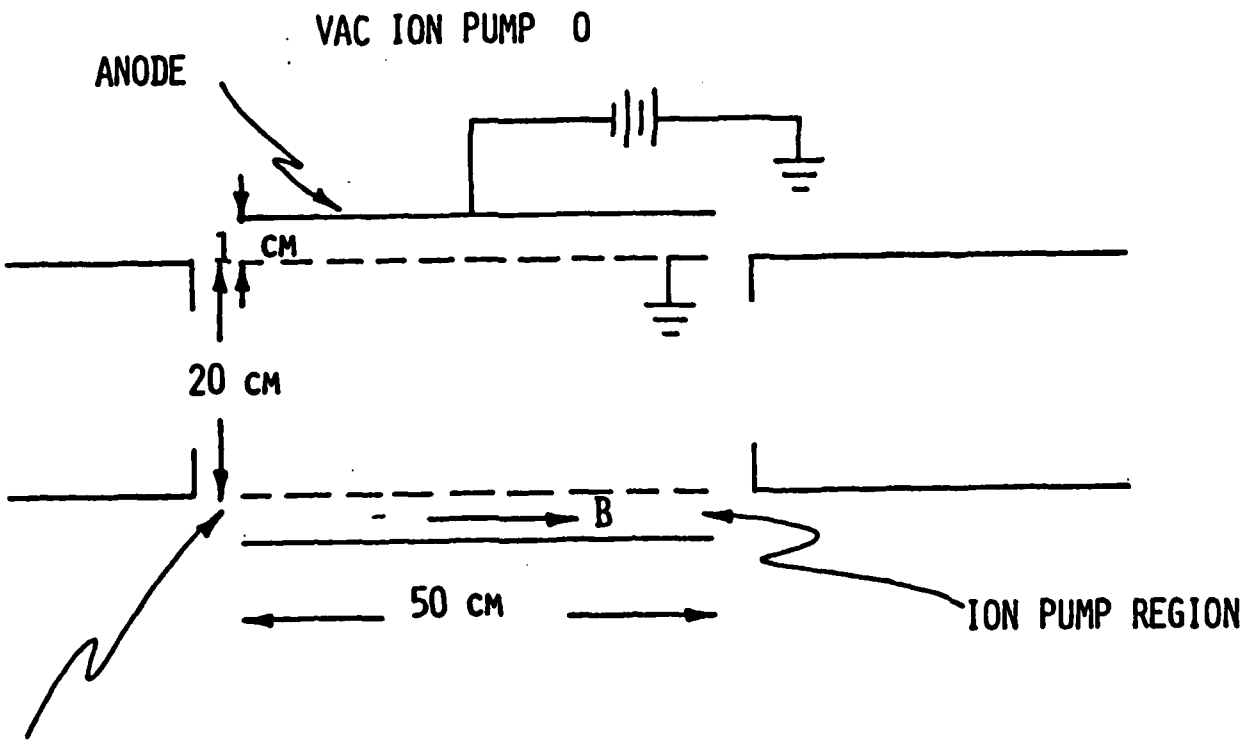

Figure 39. Peripheral Pump Configuration 1

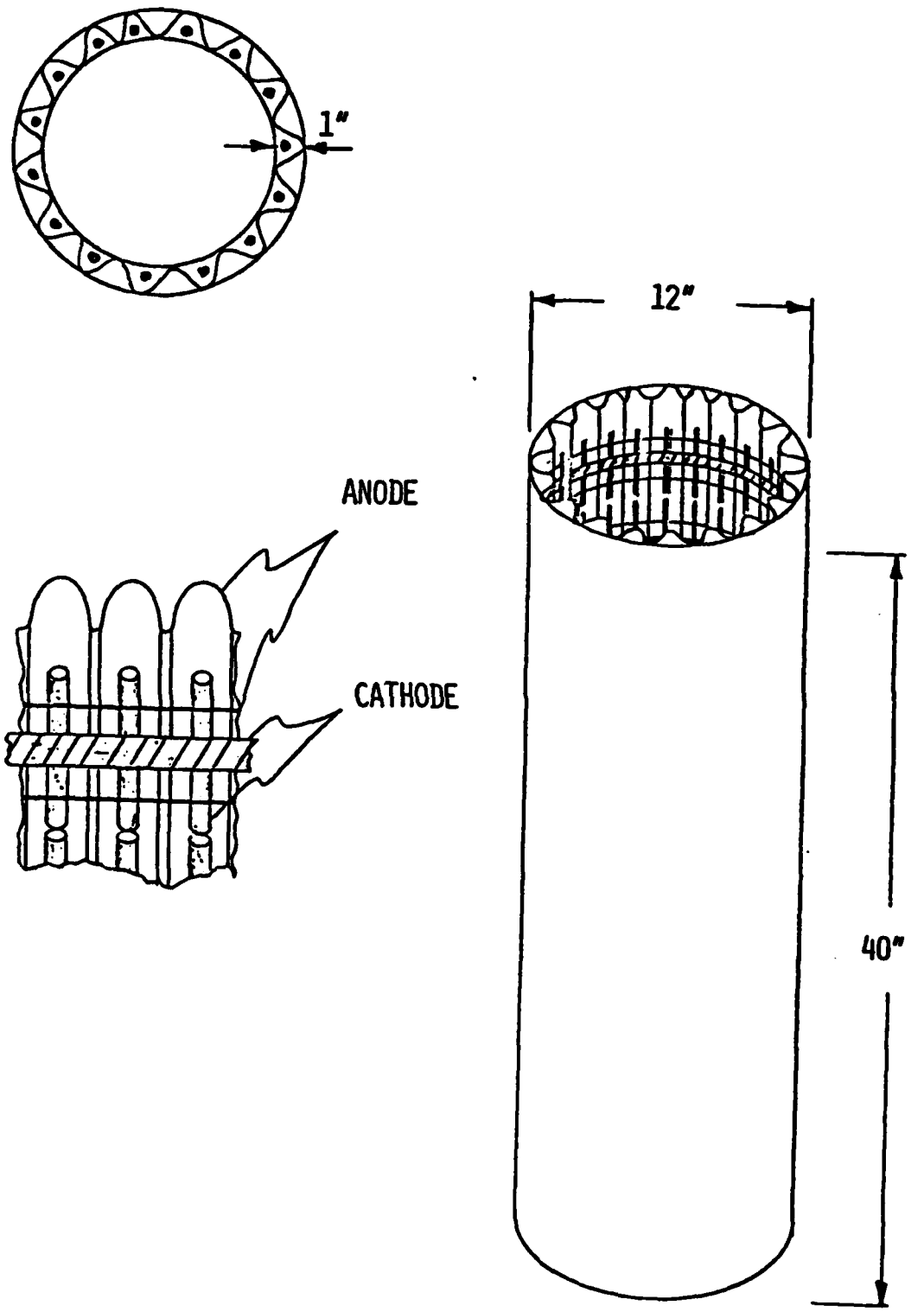

Figure 40. Peripheral Pump Configuration No. 2

These peripheral pumps ideally would be functionally equivalent to a cryobaffle with unity sticking coefficient.

3.4.4 RF Ion Getter Pump (Configuration 4)

The RF configuration does not require any steady state magnetic field, therefore, the power and weight constraints associated with solenoids or magnets disappeared. This configuration comprises of a rectangular resonant cavity which is excited by RF oscillations while concurrently electrons are injected into the cavity. The conceptual arrangement is shown in Figure 41. The cavity is basically a rectangular box that is open in the front and back sides to accommodate the optical aperture. The optical aperture will have a length of L_{opt} and a height of H_{opt}. The dimension between the front and back sides will be d along the sensor LOS axis.

The RF oscillation and electrons are injected from the same side of the cavity wall. The electrons, being of low mass, follow the transverse accelerations (i.e up and down the optical aperture) while crossing the optical aperture to the opposite side, thus increases the ionization probability of gas contaminants. The heavier gas ions are drawn to the collector plates on top and below the line of sight.

The pumping speed S is proportional to the total "ionization volume" V_e given by

$$V_e = A_s * L_{ion}$$

in which A_s is the electron source area and L_{ion} is the total ionization path during the electron's transversal of the aperture area - itself a measure of electron lifetime.

In order to obtain a first order estimate of L_{ion}, an analytic expression for the cavity Q was obtained. Q, of course, is a measure of the energy lost in the cavity - specifically,

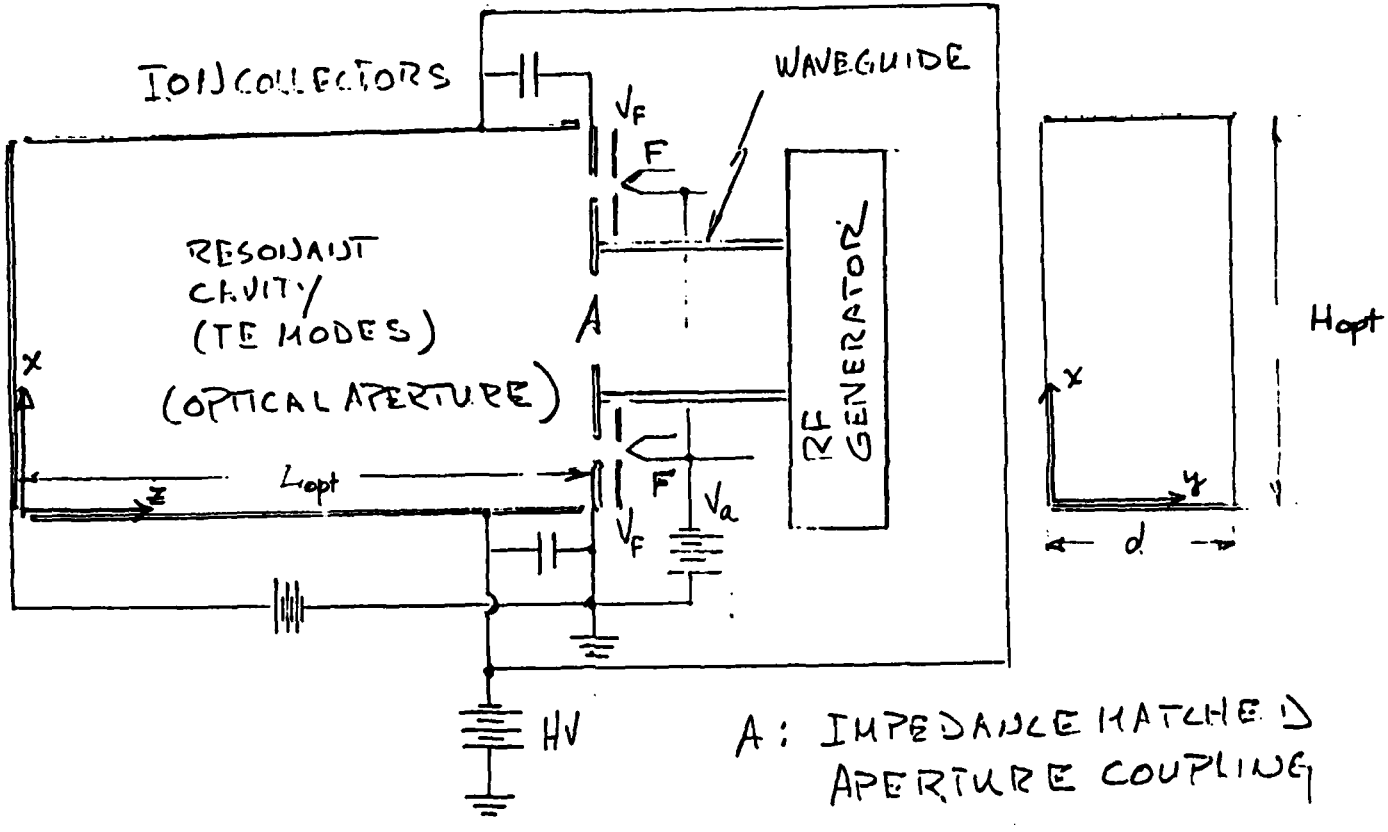

Figure 41. Schematic Drawing of Ion Getter Pump

$$\frac{d\,U_{mn}}{dt} = -\frac{fc}{Q}\,U_{mn}$$

where

$$U_{mn} = \frac{\epsilon_o}{4}\int_{cavity} \bar{E}\cdot\bar{E}^{*}\,dxdydz$$

which is readily seen to be given by ξ

$$U_{mn} = \left(\frac{a l d_o}{2mn}\right) E_o^2 \doteqdot_o \; {}_{-o} \; f_s^2\,(d\xi)$$

in which d_o is a characteristic length of the symmetic function $f_s^2\,(\xi)$. Assuming that the integral of the latter is about unity, one obtains for the cavity dimensions L_{opt} = 0.5 m, a = 0.3 m and d_o = 5.0 m.

$$U_{mn} \simeq \frac{3.32 \times 10^{-12}}{m.n}\,E_o^2 \text{ Joules}$$

It is seen that U_{mn} decreases with m, while Q_m increases. The power dissipation in the cavity, however, is linearly dependent upon the cavity frequrency f_c. Further, it is clear that L_{ion} is directly related to E_{mn}.

The computer aided estimate of L_{ion} revealed that certain selection of m=n and selection injuction conditions led to unstable trajectories - i.e., the electrons were simply transported out of the ionization region regardless of whether or not they were injected on-axis with zero transverse velocity or not. For other frequencies the election trajectories were oscillatory and confirmed and appeared to conform to the empirical form.

$$P = \frac{L_{ion}}{L_{opt}} \simeq 1 + \frac{B}{m} \frac{(Eo)}{(V_a)}$$

in which is a characteristic of the cavity dimension, m - n is the cavity mode, E_0 is the RF field amplitude, and V_a is the injection voltage of the electrons.

It is seen that P is relatively insensitive to m incrasing only very slightly with m. The above approimate relation allows the estimation of the power required for a given pumping speed. It is seen from the above that for a typical cavity Q of 104 for m - n- 100 and the other parameters as cited, a 2 Kwatt cavity dissipation barely doubles the pumping speed. Additional power will be consumed by the electron source current for a given pressure differential across the RF cavity. Figure 42 summarizes the critical parameters for 4 optical apertures and the required power for the pump system. It is assumed that the required pumping speed goes up as the aperture is increased. Aperature pumping speed of 10 l/s/cm^2 is assumed. P_∞/Po is the differential pressure ratio across the RF cavity, P_s is the total power consumption, A_s is the electron source area, V_a is the electron injuection potential and T is the cavity temperature.

From the table in Figure 42, it is seen that the pump power requirements are not at all sensitive to P_∞ / P_0 for $P_\infty/P_0 \lesssim 0.01$. That is simply due to the fact that the "price of entry" is really the power required to achieve P_∞/Po $\simeq$ 0.1 - below that required only small extra increment of power. Notice that the last two entries represent both a factor of the reduction in Aopt over the 50 X 30 cm^2 aperture assumed in the first two entries. The last entry of 31.4 cm X 21.1cm represents a smaller aperture length/height aspect ratio. The required power goes up as the aperture area is reduced by two when compared with the entry above. One may then simply conclude that the RF ion pump may be useful for IR system using a slit aperture. For example a scanned aperture with a 50 cm X 5 cm slit aperture would require about 3-4 K watt to protect the primary mirror.

A_{OPT}		P PATH EL's / L_{OPT}	SOURCE CURRENT DENSITY REQ'D FOR P_0/P_i (mA/cm^2)			P_s*
L_{OPT} CM.	H_{OPT} CM		0.01	0.005	0.001	KW
50	30	1	382	384	385+	28.9
50	30	2	191	192	192.7	15.4
50	15	2	95.5	96	96.4	8.23
35.4	21.2	2	135	136	136.5	11.2

*P_s COMPUTED FOR P_{00}/P_0 INCLUSIVE OF 1 KW RF POWER WHERE REQUIRED

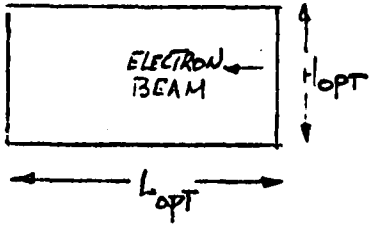

$A_s = 300\,CM^2$

$V_A = 250\,V$

$T = 300°K$

$S_A = 10\,\ell/s/CM^2$

Figure 42. Pump Power Estimates

3.4.5 Particulate Pump (Configuration 5)

An orbit particle ejection rate and velocity due to meteroid impact of surface particle contamination was estimated for IRAS.[12] It is reproduced in the following table. Similar particle ejection volocities are assumed for the design of a particulate pump.

Table 3. Particle ejection rate due to micro meteoroid impact; satellite surface area, 30 m^2, surface cleanliness, 10^6 particles/m^2 (level 500 per MIL-STD-1246A)

Size range (um)	Ejection rate ($hour^{-1}$)	Most probable velocity (cm/sec)
5-15	0.51	40
15-25	0.45	12
25-35	0.63	5
35-45	0.80	4
45-55	0.93	4
55-65	1.02	3
65-75	1.10	3
75-85	1.15	3
85-95	1.18	3
95-105	1.20	3

The particulate pump consist of a electron cloud generation region and a deflection region. Figure 43 illustrates the basic concept. The electron cloud is generated by a magnetically confined gas discharge within the anode. A election density of 4.25×10^8 cm^{-3} is sufficient to attach 100 electrons on a 1 um spherical particle within an ionization region of 30 cm long. Generation of this electron density within an anode of 12 inches in diameter would require 44.6 KV and an axial magnetic field

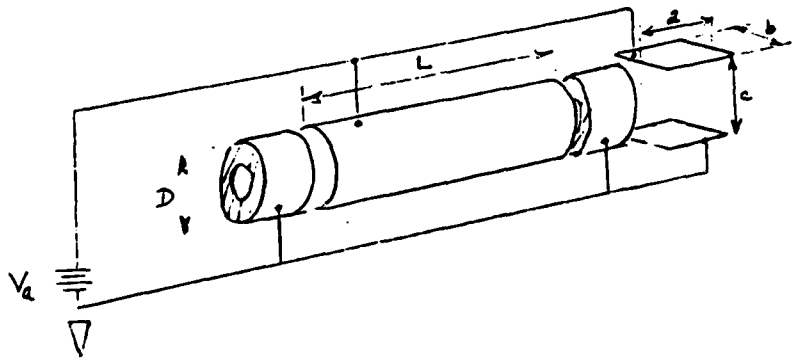

Figure 43. Particulate Pump Configuration

Optical Clear Aperture	8 inches
Anode Diameter	12 inches
Anode Length	30 cm
Cathode Length(s)	5 + ⅝ cm
Defl. Plate Length	20 cm
** Device Length	50 cm
Applied Voltage	44.6 KV
Magnetic Flux Density	280 Gauss
Electronic Current	330 μA @ 10^{-7} Torr.
Drain Power	14.7 watt
Solenoid Weight	36.4 lbs.
Solenoid Power	45 watt

* Max. Particle Velocity	vs.	Particle Diameter
6.03 m/s		1 μm
3.64		10
0.60		100

* IRIS v_p<1m/s

** Device Length 20" for a 12" Aperture

Figure 44. Particulate Pump Parameter Summary

of 280 gauss. A set of parallel plates charged up to the same potential can deflect the 1 um particle within 10 cm if the particle velocity is less than 6 m/sec. The maximum velocity allowed for 10 and 100 um particles are 3.64 and 0.60 m/sec respectively. The magnetic field can be generated by a solenoid of 36 pounds while consuming 45 watts in joule heating.

Figure 44 summarized the various parameters for the particulate pump. Figure 45 illustrated how this pump may appear if integrated in a CIRRIS - type telescope.

3.5 Magnetic Field

To maintain the required electron density in the pumping region a magnetic field is often required. Methods of maintaining the required field strength in the spacecraft environment are discussed. A nominal magnetic flux density of 250 gauss has been used to compare technologies.

Three possible variations in field configuration are shown in Figure 46. The use of a permanent magnet to maintain this field is considered because it would be a passive system and thus have no temperature or power requirements. These advantages are outweighed by a weight of greater than 10^3 kilograms for geometries a and b in Figure 46. Geometry c could be provided using a somewhat lighter permanent magnet configuration which obstructs a fraction of the annular field region.

The use of an electromagnet to maintain the required field has been investigated. Three winding configurations are shown in Figure 47. These configurations are based upon a simple solenoid where the flux density is defined as

$$B = u_o \frac{Ni}{1} \text{ Wb/m}^2$$

where

u_o = $4\pi X 10^{-7}$ MKS units
Ni = Amp turns of winding
1 = length of solenoid winding (m)

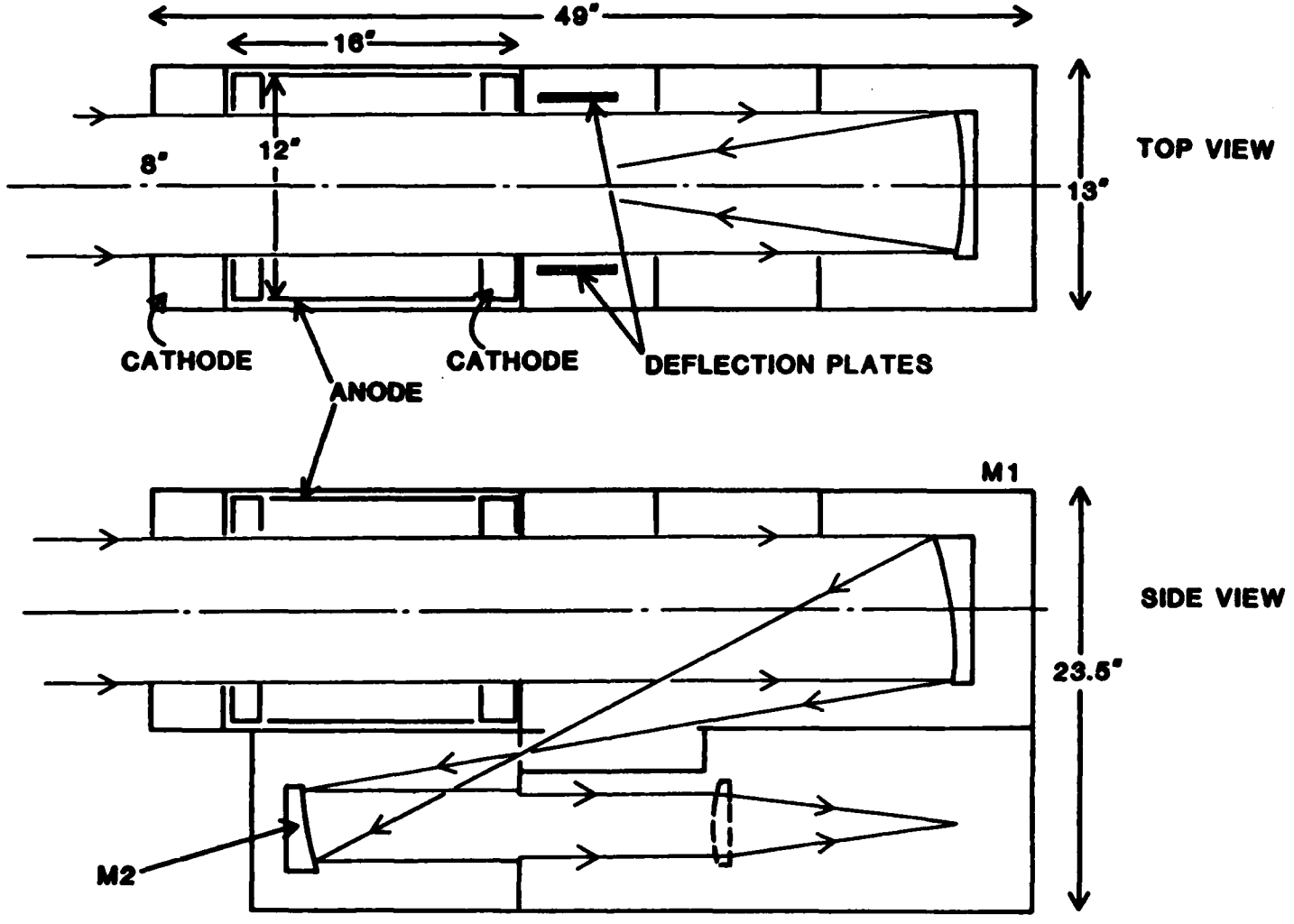

Figure 45. Integration of Particulate Pump in CIRRIS-Type Telescope

Configuration I splits the solenoid into two separate coils to product a uniform B fixed across the baffle region. The overall size of these coils may be reduced but only by reducting B field uniformity. Configuration II is a simple solenoid, and Configuration III uses magnetic pole pieces having a high permeability to constrain the generated flux to an annular region around the baffle.

It can be shown that the winding weight of a magnetic solenoid is proportional to

$$\frac{(BLD)^2}{P}$$

where

B	=	required flux density
L	=	magnetic coil length
D	=	magnetic coil diameter
P	=	coil power dissipation

The winding is assumed to be of copper wire at a specified temperature. It should be noted that the winding weight is independent, in the first order, of wire size and current. The winding power dissipation is due to winding resistance. Thus, if the coil were cooled from 295°K to 100°K, there will be a factor of five reduction in winding resistance or, if spacecraft power is budgeted to a fixed value, an equal reduction in winding weight.

If the winding temperature can be reduced to below 30°K, a superconducting magnet is possible. This would increase the complexity of the pumping system but it would permit the maintenance of greater field flux-densities while essentially requiring no electrical power input. Flux densities of 5×10^4 gauss are routinely achieved in superconducting solenoids.

Typical power requirements and weights for the three technologies are given in the following table:

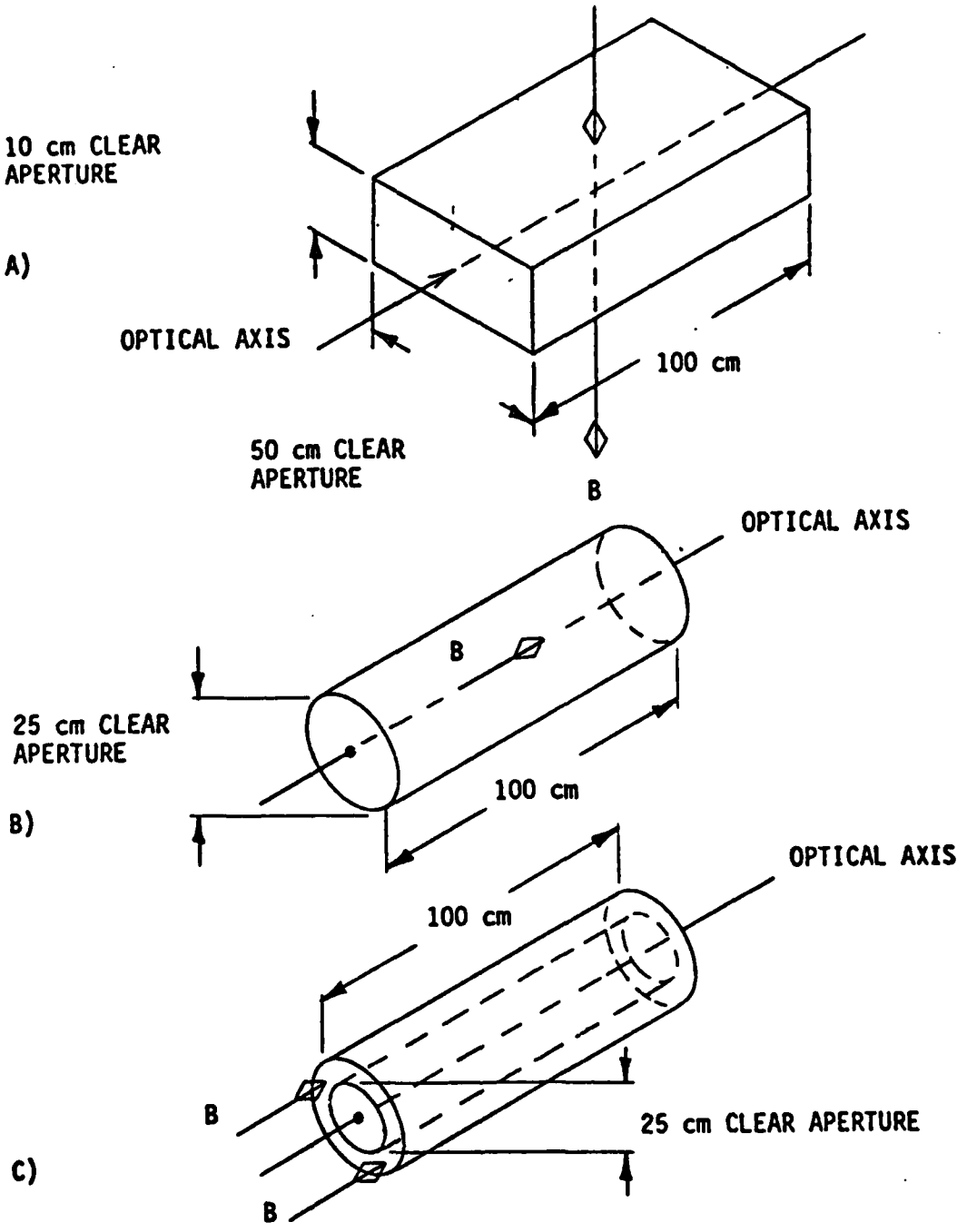

Figure 46. Magnetic Field Geometries

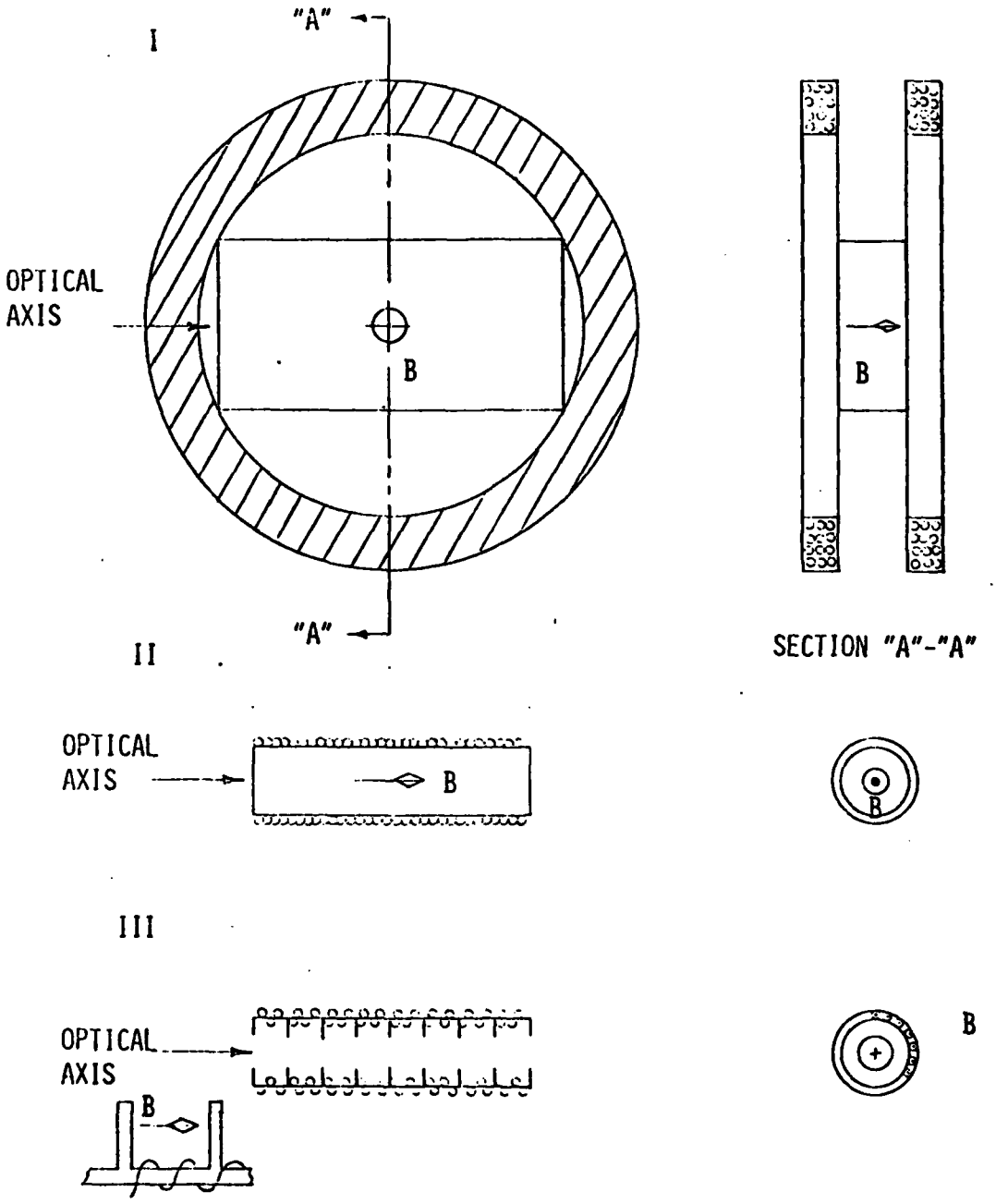

Figure 47. Magnetic Winding Configurations

Table

Estimated Power Requirements & Weights of Three Magnet Designs

		WEIGHT (kg) CONFIGURATION		
		I	II	III
	POWER (W)			
CONVENTIONAL (295°K) ELECTROMAGNET	50	900	750	700
COOLED (100°K) ELECTROMAGNET	50	200	150	150
SUPERCONDUCTING ELECTROMAGNET	--	250	250	250

3.6 High Voltage Engineering Considerations

The design of electrodes with stand-off voltages greater than 100,000 V involves fairly massive structures of high purity alumina insulators of length commensurate with a general rule of thumb that it requires a one inch leakage path for every 10KV. The above is usually accomplished by corrugating the surface which extends the surface as:

$$S = \frac{L}{2\pi} \int_0^{2\pi} d\vartheta \sqrt{1 + \left(\frac{\pi \alpha N D}{L}\right)^2 \cos^2 \vartheta}$$

wherein L is the length of the insulator, D is its diameter, N the number of corrugations, ϑ is a normalized variable, and α is the ratio of corrugation depth to the diameter. An additional virture of the corrugation is that fact that deposits that collect on the insulation in a vacuum will not form a continuous film.

All electrodes must be highly polished and given a radius such that the field near the surface doesn't exceed 250 KV/in. This is

especially important in very high and ultra high vacuum systems in which very clean surfaces and small particulates or rough spots on the electrodes may initiate a brakdown through a field-emission induced townsend discharge.

Materials that must be avoided in the presence of high voltages include tin and cadmium which have a tendency to grow whiskers in areas of high field stress. All high voltage electrodes must be conditioned prior to their use in the vaccum system. This process repeatedly cycles the high voltage gear up and down with high impedance current limiters in series to limit the breakdown current after an arc or spark occurs.

It should be noted that HV insulators charge up during operation which may cause fluorescence - usually in the visible but I have not heard that there is no attendant IR radiation as well. Should an arc or breakdown occur within an HV system, that system will no longer be able to maintain the design voltage because the arc usually creates melt craters in opposing electrodes and metal vapor deposts on insulating surfaces. It is, therefore, good practice to choose material of high melting point such as W or Mo as electrode material. The difficulty with the refractory metals, however, lies in the fact that they are difficult to polish since they are generally of a sintered material. However, there are Mo alloys such as Ti/Al/Mo which are often used as anode material.

Finally EHV systems must have pressure sensitive interlock arrangements that prevent an accidental turn-on of the high voltage when the pressure is still high, since a breakdown is certain as can be seen in the Figure 48. It is seen there that the electric field only need be on the order of 100-300 V/cm to cause breakdown at 1 Torr.

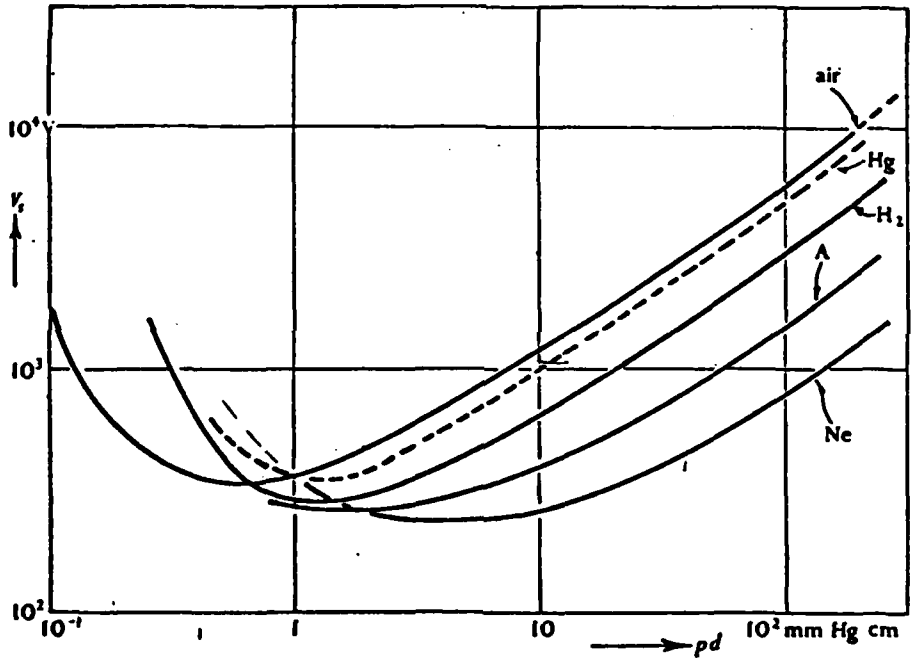

Figure 48. Sparking Potential V_S as a Function of the Reduced Electrode Distance pd in Several Gases

4.0 EFFECTIVENESS EXPERIMENT CONCEPTUAL DESIGN

The pumping efficiency of an IACS design should be measured so that the various candidate designs can be evaluated in terms of their effectiveness in reducing the flow rate of the contaminants through the IACS.

An experimental setup to measure the effectiveness of various ion pump configurations is shown in Figure 49. The experiment description is summarized in Figure 50. A modified commercial ion pump will be used to model the proposed IACS configuration. Scaling laws will be used to project the results to the proposed IACS configuration.

The experiment will be conduced inside a vacuum chamber of modest dimensions (i.e., 12" D X 36"L). The interior volume of this chamber will be divided into two partitions. The modified ion pump will be mounted at an orifice which opens to both volumes. A valve will be mechanized which can be opened or closed so that gas particles in the two volumes can flow freely back and forth or can be isolated completely. The contaminant gas is connected to volume 1 (V1) of the chamber through an automatic pressure controller which can regulate the flow rate of contaminants into the V2. A pressure gauge will monitor the V1 pressure continuously.

The other volume (i.e. V2) of the chamber is connected to two pumps. A turbomolecular pump which is backed up by a diffusion pump is used to pump V2 from atmospheric pressure down to 10^{-6} torr. A valve will be closed to isolate the turbomolecular pump from the chamber volume once this pressure is obtained. The other connected pump is an ion pump which will be used to pump down V1 and V2 to the lowest pressure possible when the modified ion pump under test is turned off and the partition gate valve is opened. This ion pump can be used to monitor the pressure as well as the outgassing rate of the chamber by measuring the current drawn through its power supply and use of a calibration curve. The chamber has to be cleaned thoroughly and baked before pumpdown to reduce the condensables on

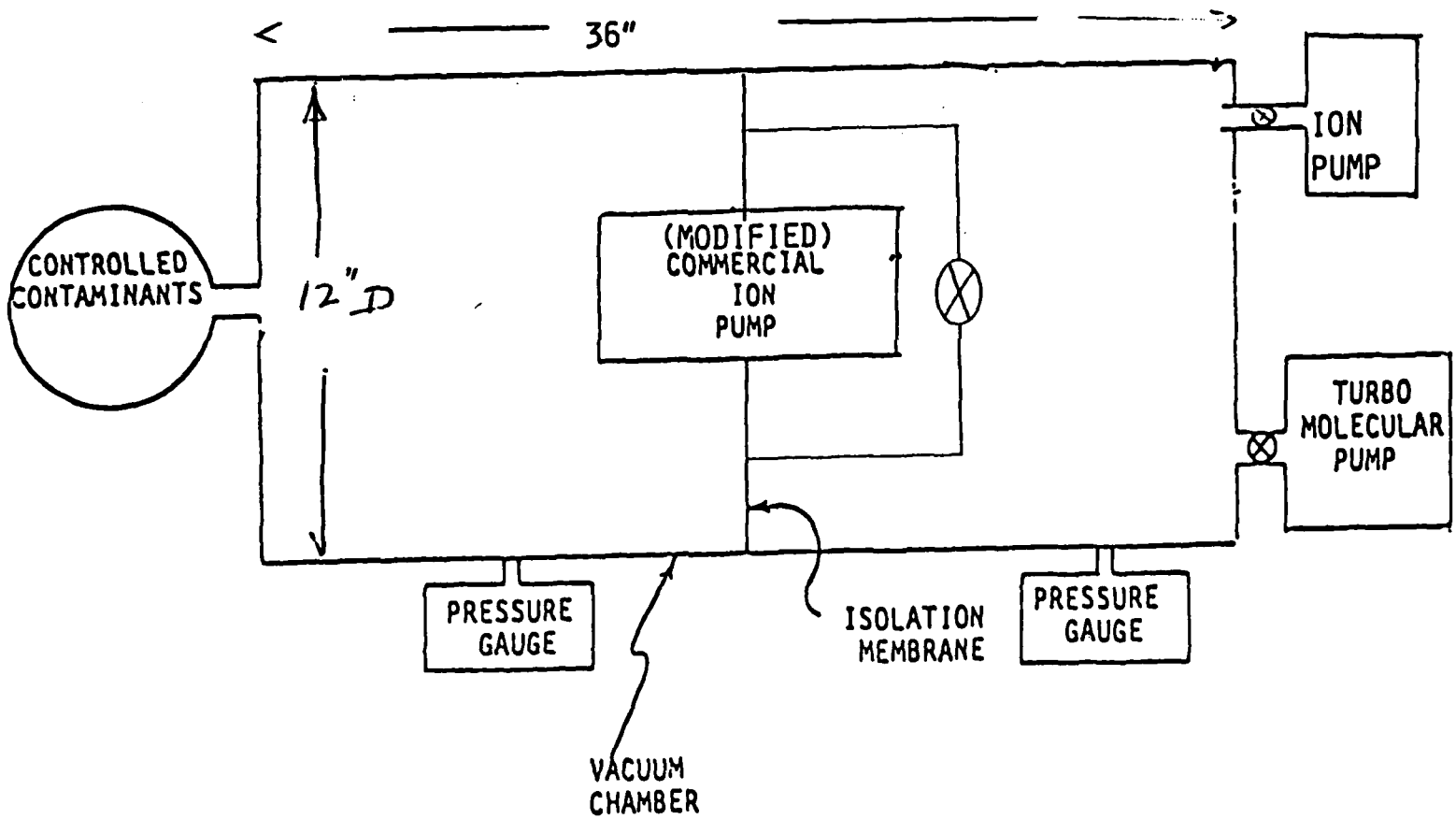

Figure 49. Effectiveness Experiment

- MODIFY COMMERCIAL ION PUMP TO SCALE TO PROPOSED CONFIGURATIONS
- MEASURE PRESSURE RATIO AND PUMPING RATE WITH PUMP OFF AND CONTAMINANT FLOWING
- MEASURE PRESSURE RATIO AND PUMPING RATE WITH PUMP OPERATING AND CONTAMINANT FLOWING
- EXPERIMENT IS CONDUCTED AT ROOM TEMPERATURE
- CHAMBER IS CLEANED AND BAKED(STAINLESS WITH METAL GASKETS)
- PUMPING RATE AT CONSTANT PRESSURE RATIO IS A DIRECT MEASURE OF EFFECTIVITY

Figure 50. Experiment Description

the interior walls. A stainless steel chamber with metal gaskets at all mechanical interfaces will provide optimal chamber residual pressure. The chamber is held at room temperature.

Upon satisfactory pumpdown on the chamber, the partition valve is closed and contaminant gas is introduced into V1. The test pump is turned on. The automatic pressure controller will meter the contaminant flow rate so that a constant pressure is established in V1. The gate valve at the chamber partition is now opened so that contaminant gas can flow through the test pump into V2. The monitoring ion pump will keep V2 pumped down, as well as monitoring the flow rate of contaminants through the test pump. After the pressures in V1 and V2 are stabilized, one can measure directly the conductance of the test pump.

AD-A144 197 DESIGN STUDY OF ION ANTI-CONTAMINATION SYSTEM(U) UTAH 2/2
STATE UNIV LOGAN SPACE DYNAMICS LABS W K WONG
07 MAR 84 SDL/84-014 AFGL-TR-84-0086 F19628-83-C-0056
UNCLASSIFIED F/G 20/6 NL

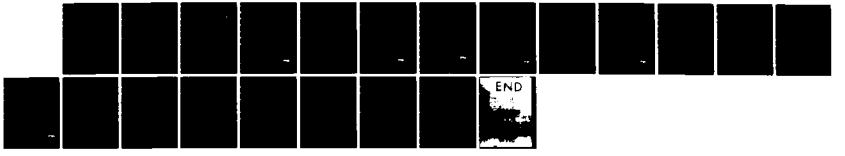

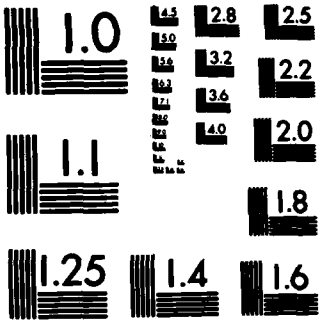

5.0 IR RADIATION ANALYSIS

Figure 51 illustrates the spectral positions of various bands of atmospheric constituents. Vertical lines correspond to the positions of the fundamental vibration/rotation bands of the species listed. Rotational bands tend to fall in the LWIR while electronic bands of relatively low lying states fall primarily in the UV to SWIR. Both "hot" and combination bands of the species listed, as well as other contaminant molecules, will fall throughout the infrared, as will Rydberg transitions from highly excited atoms and molecules. Lastly, electron-neutral and electron-ion Bremsstrahlung are continuous processes which will provide radiation throughout the spectral region shown.

Figure 52 shows potential excitation mechanisms introduced by electron irradiation of gases within an enclosing chamber. Creation of excited states will ultimately lead to radiation.

Figure 53 is a schematic of one possible configuration for the ion anti-contamination system. Various quantities are as defind.

Figure 54 summarizes typical ion pump operating conditions for the schematic of Figure 53 n_e is electron density, V. voltage, n_N and V_N, neutral density and velocity, respectively, and τ_R is the characteristic molecular residence time.

Figure 55 shows upper bound radiational levels which might arise for the scenario of Figure 53 and a direct excitation process. Typical band parameters for a 10 um radiator have been applied. The quantity a is a measure of the electron collison efficiency for excitation.

Figure 56 is a plot of blackbody radiance vs. wavelength for several temperatures. Predicted non-equilibrium radiance levels can be contrasted to that for a blackbody background at a specific temperature.

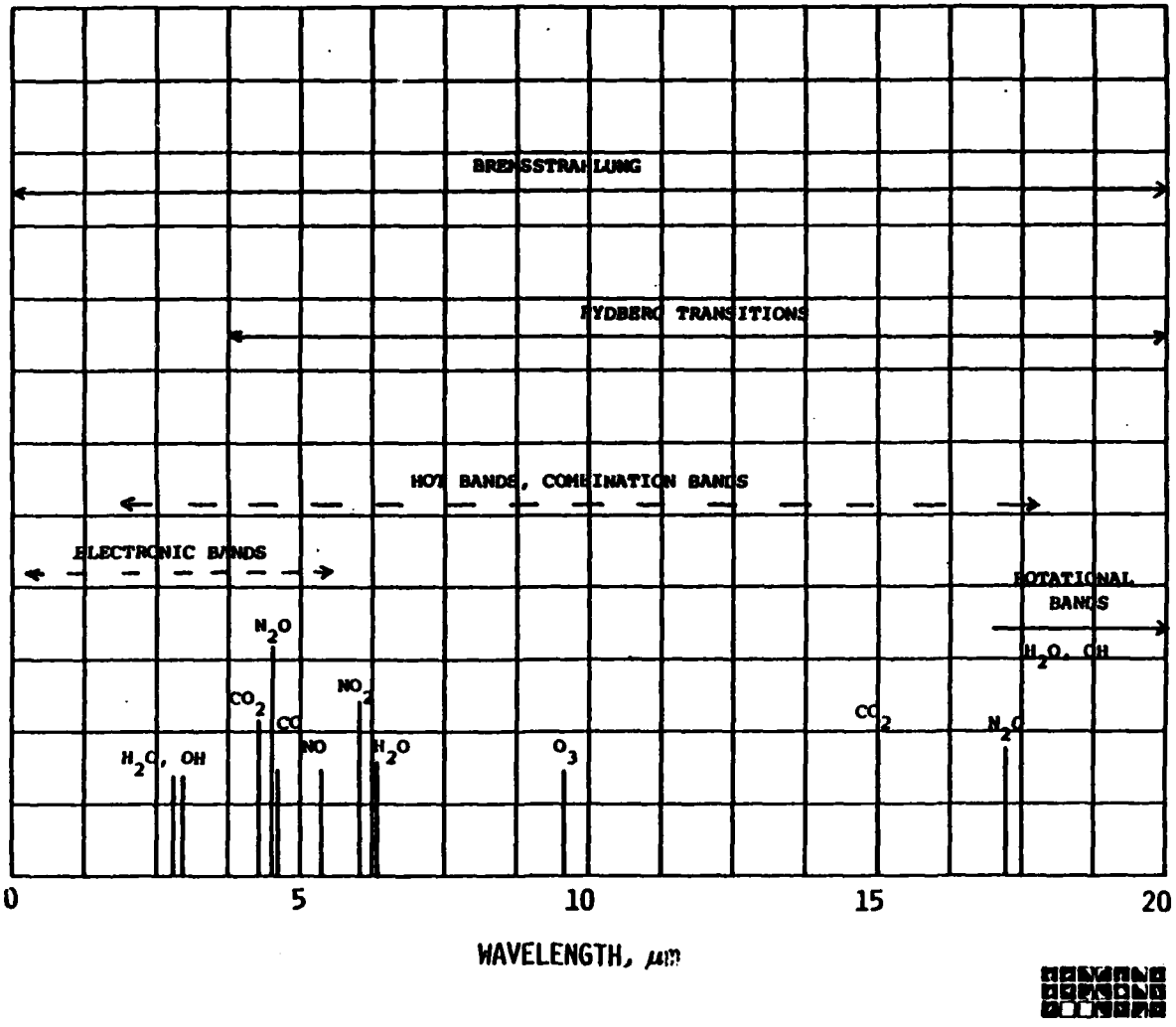

Figure 51. Infrared Bands

1. Direct excitation

$$e + X \rightarrow e + X^*$$

2. Dissociative excitation

$$e + AB \rightarrow e + A + B^*$$

3. Excitation by ionization

$$e + AB \rightarrow AB^{+*} + 2e$$

$$e + AB \rightarrow A(A^*) + B^{+*}(B^+) + 2e$$

4. Recombination radiation

$$X^+ + e \rightarrow X^*$$

5. Bremsstrahlung

6. Electron/ion-surface interactions

Figure 52. Sources of Radiation

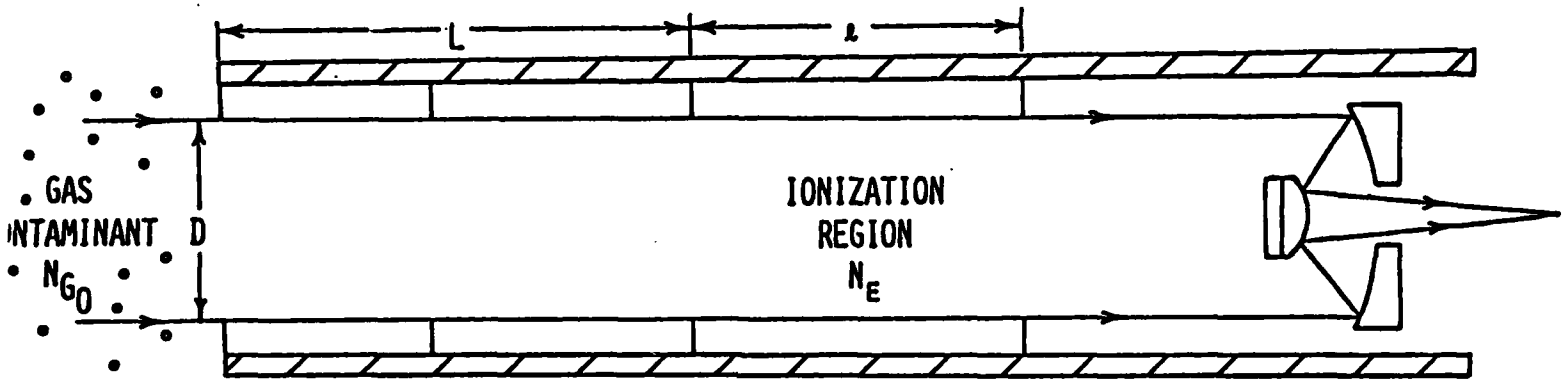

N_{G_0} - CONTAMINANT DENSITY AT FRONTAL BAFFLE (CM^{-3})

D - DIAMETER OF BAFFLE OPENING (CM)

A - CROSS SECTIONAL AREA OF BAFFLE OPENING $\frac{\pi D^2}{4}$ (CM^2)

L - LENGTH FROM APERTURE TO IONIZATION REGION (CM)

ℓ - LENGTH OF IONIZATION REGION (CM)

Figure 53. Schematic of Ion Anti-Contamination System

LENGTH ~ 1/2 M

$n_e \sim 2 \times 10^{10}$ cm^{-3}

V ~ 10 keV

$n_N \sim 10^7 - 10^8$ cm^{-3}

$V_N \sim 10^5$ cm/s

$\tau_R \sim 5 \times 10^{-4}$ s

Figure 54. Characteristic Operating Conditions

$$e + x \xrightarrow{\sigma} x^*$$

$$x^* \xrightarrow{\tau} x + h\nu$$

Can readily show upper bound

$$I \approx \frac{\sigma v n_e n_N h\nu \ell}{4\pi\Delta\lambda(1+\tau/\tau_R)} \quad \frac{W}{cm^2\text{-}sr\text{-}\mu m}$$

Ex. $\lambda = 10\ \mu m$, $\Delta\lambda = 1\ \mu m$ $\quad \tau = 5 \times 10^{-2}$ s

$$\sigma v = a\sigma_T v \approx 10^{-7} a\ cm^3/s$$

$$I = 10^{-11}\text{-}10^{-10} a \quad \frac{W}{cm^2\text{-}sr\text{-}\mu m}$$

Figure 55. Generic Case

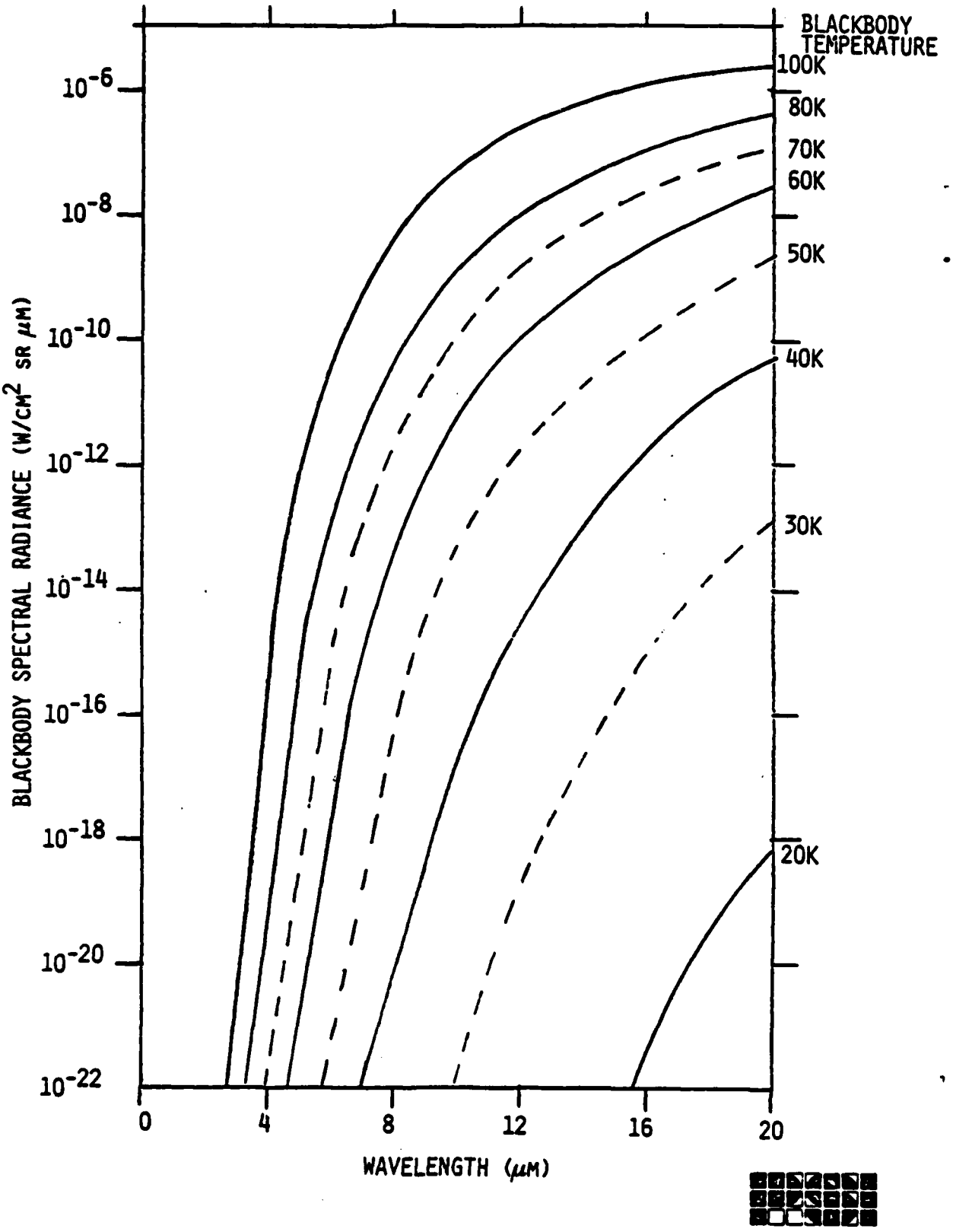

Figure 56. Blackbody Radiance as a Function of λ and T

Figure 57 is an estimate of radiation levels resulting from recombination radiation (i.e., through creation of Rydberg states) and Bremsstrahlun radiation. The low electron densities and short ion lifetimes make these processes unimportant sources of radiation.

Figure 58 gives the conclusions of the radiation analysis. Potential radiation levels due to surface interactions are difficult to assess given the limited data base. Such effects should be invetigated experimentally.

$$e + x^+ \rightarrow x^* \qquad k < 10^{-12}\ cm^{-3}s^{-1}$$

$$e + AB^+ \rightarrow A + B^* \qquad k < 10^{-7} \left(\frac{300}{T_e}\right)^{1/2}$$

$$\tau_{recomb} \gtrsim 1S$$

Ion lifetime $\sim 10^{-8}$ s

$\therefore$ Unimportant

BREMSSTRAHLUNG (STRONG UPPER BOUND)

$$I_\lambda \lesssim \frac{1.6 \times 10^{-31}\ NeN_1 \ell}{\lambda^2 T^{1/2}} \quad , \ m$$

$$I_{10\ \mu m} \lesssim 10^{-18} - 10^{-19}\ \frac{W}{cm^2\text{-}sr\text{-}\mu m}$$

$\therefore$ Unimportant

Figure 57. Recombination Radiation

1. DIRECT EXCITATION MARGINALLY IMPORTANT

2. RECOMBINATION, BREMSSTRAHLUNG UNIMPORTANT

3. SURFACE INTERACTIONS NOT ASSESSED

Figure 58. Summary

6.0 EXPERIMENTAL PLAN FOR MEASURING IR RADIATION LEVEL

The following two figures describe the proposed radiation experiment (Figures 59 and 60). The goal of this experiment is to operate a discharge similar to that to be used in the ion anti-contamination system under conditions that would be encountered during operation in space. The electrical characteristics will be simulated by using a suitably modified ion pump of the Penning discharge type. The species to be pumped will be neon because of its similarity to oxygen atoms (a species of primary interest), and its high vapor pressure under cryogenic conditions. Preconditioning of the walls will be room temperature pumpdown followed by cooling to 20K, the procedure used before launch. The radiation will be monitored using a broadband radiometer capable of measuring 10^{-11} W/cm^2-Sr-um against the background of the cooled cryoshroud. Major spectral features will be measured by a series of filters. Their dependence on macroscopic system parameters as discharge voltage, current gas pressure and species will be determined.

In order to measure these low radiative levels in the infrared it is necessary to have the background at a temperature below 40K. However, at this temperature, vapor pressures of the major air constituents, nitrogen, oxygen, etc., are above the pressure levels of prime interest and the experiment must be cooled to approximately 20K to remove (cryopump) these gases. It is expected that discharge electrons and ions will knock these gases off the chamber walls and they will contribute to the measured radiation. This is as would be expected to retain cryopumped molecules, but it does distinguish this experimental simulation from a more flexible experiment which would determine the origin of the emissions. This more detailed experiment would discriminate test gas from contaminant gas emission through use of spectral content (interferometer or spectrometer) and by having a clean, bakable vacuum system to eliminate contamination on the walls.

GOAL: BOUND RADIATION LEVELS FROM A PENNING DISCHARGE SIMILAR TO THAT TO BE USED IN THE ION ANTI-CONTAMINATION SYSTEM.

APPROACH: USE FILTERED RADIOMETER TO OBSERVE ENERGETIC ELECTRON-PARTICLE INTERACTIONS WITH TEST GASES REPRESENTATIVE OF SPACECRAFT ENVIRONMENTS.

PSI STATEMENT OF WORK

1) DESIGN AND SPECIFY RADIOMETER EXPERIMENT

2) PROVIDE A SUITABLE PENNING DISCHARGE

3) PERFORM ROOM TEMPERATURE DISCHARGE CHARACTERIZATION (AT PSI)

4) PERFORM 77°K SYSTEM CHECKOUT AND BACKGROUND MEASUREMENTS

5) PERFORM 20°K RADIOMETER MEASUREMENTS AND ANALYZE DATA

6) SUPPORT SYSTEM DEVELOPMENT

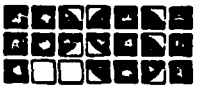

Figure 59. Radiation Experiment

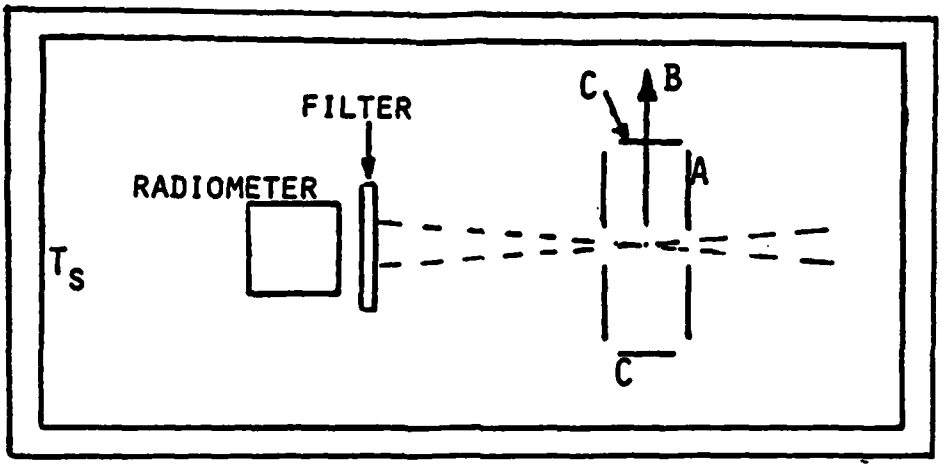

DETECT RADIATION LEVELS AT 10^{-11} W/CM^2-SR μM

λ = 2-20 μM

T_S < 40°K SET BY RADIOMETER

T_S = 20-30°K SET BY GAS PURITY-CRYOPUMPING

$n_e \sim 10^9 - 10^{10}$ CM^{-3}

V ~ 1-5 KV

$n_g \sim 5 \times 10^9 - 5 \times 10^{11}$ CM^{-3}

GASES Ne, POSSIBLY Ar, N_2, AND O_2

Figure 60. Experimental Configuration

SSG will provide the vacuum chamber and its internal cryoshroud which is capable of being cooled to 20K. There will be provisions for gas pumping and electrical feedthroughs while maintaining adequately low background radiative levels. SSG will also provide the radiometer.

PSI will provide a Penning discharge modified so that its internal radiation can be monitored. The modified Penning discharge will be characterized by PSI at room temperature before the cold measurements. It is expected that a series of measurements at 77K will be undertaken before 20K measurements are made to increase the probability of success of the low temperature test series. Besides making the emasurements and analyzing them, PSI will also support the overall system development.

APPENDIX A: KEY THEORY & DEVELOPMENT OF ION PUMP

Survey of published literature is completed. Appendix A highlights the key theory and developments of the ion pump. A full bibliography is provided in the reference. The two major commercial manufacturers of ion pumps are Perkin-Elmer and Varion. All ion pump configurations are derivatives of the Penning discharge cell or the magnetron gauge in single or array configurations.

Ion pumps normally operate below 10^{-5} torr and require a power supply of 3→5 kilovolt (dc). The starting current is less than 250 mA for pumps having capability up to 220 liter/sec. The operating current is directly proportional to the operating pressure for a given pumping capacity. For example, an 8 L/S pump draws 1 mA at 10^{-5} torr and it draws only 1 uA at 10^{-8} torr. A smaller capability pump draws less current at the same pressure. For example, a 2 L/S pump draws only 170 uA at 10^{-5} torr and 0.2 uA at 10^{-8} torr, respectively (Figure A).

APPENDIX A - KEY THEORY AND DEVELOPMENTS OF ION PUMP

1937 - Penning describes Philips Vacuum Gauge which contains two paralelel plates of zirconium as cathode and a ring as anode, and is placed between the poles of a permanent magnet with its field perpendicular to the cathode. A gas discharge takes place between cold electrodes at a pressure about 1000 times lower than is possible in a tube of similar construction without magnetic field. It has been found that the magnitude of the discharge current is a good measurement of pressure. Application pressure range of 2×10^{-3} to 10^{-5} torr.

1949 - (Ref.13) Penning and Nienhis describe a new electrode configuration: The cathode plates are round discs parallel to the axis of the magnetic field and the anode is in the form of a cylincrical jacket. Ten times more sensitive than old design and extends pressure range to 10^{-7} torr.

1959 - (Ref.14) Redhead developed a theory for the striking characteristics of the self-sustained Townsend discharge in a coaxial diode with an axial magnetic field that can be used effectively as a means for measuring extremely low gas pressure (below 10^{-10} torr). The inner cylinder was used as the anode and the outer cylinder as the cathode, the ends of the cathode cylinder were partially closed to prevent migration of electrons from the discharge in an axial direction (inverted-magnetron gauge).

1961 - (Ref.15) Jepsen developed a theory for the effects of space charge in inverted and normal magnetrons and in Penning structures. Estimates are made of current flow and its dependence on voltage, magnetic field, electrode geometry, and pressure. It was shown that discharges of much greater intensity may be expected in normal magnetron with filementary cathodes than in inverted

magnetrons with filementary anodes. It was also shown that comparable maximum discharge intensities should be obtainable in Penning structures and in normal magnetrons.

1961 - (Ref.16) Jepsen measured large space-charge depressions of potential on the axis of a Penning discharge and verified that the anode traps a very dense cloud of electrons and that space-charged fields play a dominant role in the behavior of the discharge. It was determined that a naturally collimated, very intense ion beam of well-defined energy emerged from a 1/8 in. diameter hole drilled on a 1/2 in. diameter cell. At a pressure of 10^{-6} torr a beam current of about 1 microamp is obtained and a full beamwidth of 5° to 10° as measured at the half intensity points 2 inches away from the beam aperture.

1968 - (Ref.17) Lange measured the electron density in a Penning cell over the pressure range 10^{-4} to 10^{-11} torr (Argon) at various values of the applied voltage V) and magnetic field (B). The electron density for a given value of V and B was found to be essentially constant for pressures below 10^{-6} and to increase nonlinearly from 10^{-6} to 10^{-4} torr. The charge density increases linearly with V but is much less sensitive to B. Below 10^{-6} torr densities in the range 0.5 - 5 X 10^{9} per cm^{3} were found.

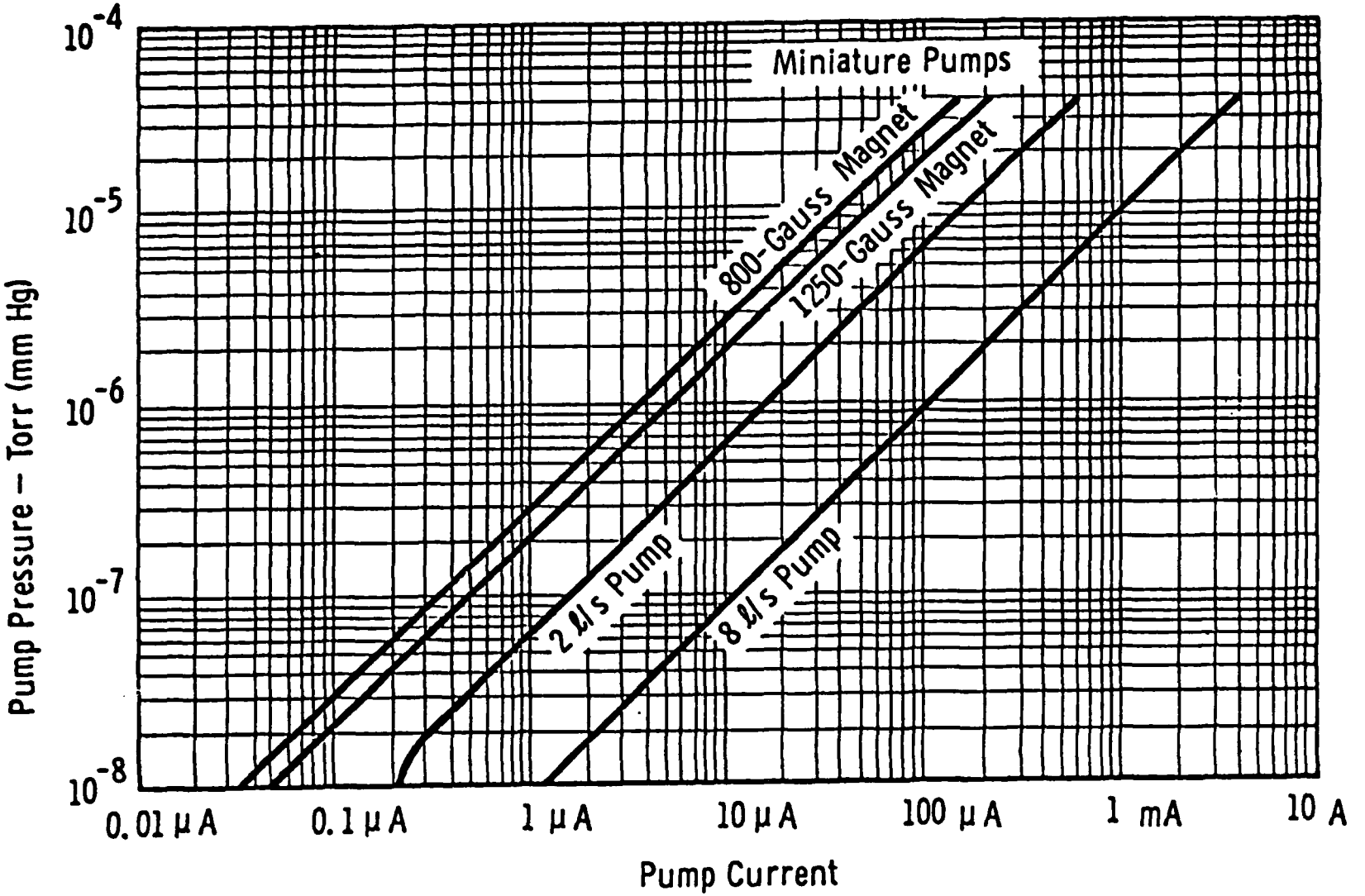

Figure A. Current vs. Pressure

REFERENCE

1. R. P. Heinish, R. P. Young. "Some Observations of Empirical Mirror Scatter," Opt. Eng. Vol. 13, No. 4. (1974)

2. R. P. Young, "Low Scatter Mirror Degradation by Particle Contamination," Opt. Eng. Vol. 15, No. 6. (1976)

3. Somers, Muscari, "Effects of Contaminants on BRDF," SPIE Vol. 338.

4. Wong, Wang, Murdock, "Out of Field of View Rejection Measurements of the ZIP Telescope #2," SPIE Vol. 384.

5. F. Arnold, "Degradation of Low-Scatter Metal Mirros by Cryodeposit Contamination," AEDC-TR-75-128, October 1975.

6. Glassford, Lin, "Outgassing Rate of Multilayer Insulation," Proc. of USAF/NASA International Spacecraft Contamination Conference, AFML,PR-78-190 (1978). WRIGHT PATTERSON AFB, AF MATERIALS LAB.

7. The 1976 U.S. Standard Atmosphere, NOAA, NASA, and USAF, Washington, D.C., (1976).

8. Roder, H. M., and L. A. Weber, "ASRDI Oxygen Technology Survey, Vol. 1: Thermophysical Properties," NASA SP-3071, National Aeronautics and Space Administration, p. 418 (1972).

9 Kelly, K. K., "Contributions to the Data on Theoretical Metallurgy III. The Free Energies of Vaporization and Vapor Pressures of Inorganic Substances," Bulletin 383, U.S. Department of the Interior, Washington (1935).

10. Zemansky, M. R., "Head and Thermodynamics." McGraw-Hill, New York (1951).

11. Dawson, J. P., and J. D. Haygood, Cryogenics, 5, 57 (1965). A. von Engel, "Ionized Gases," Oxford (1965).

12. Andreozzi, Irace, Maag, "Contamination Control of the Infrared Astronomical Satellite," SPIE, Vol. 216 (1980).

13. F. M. Penning, K. Nienhuis, "Construction and Applications of a New Design of the Philips Vacuum Gauge" Philips TEch. Rev. 11, pp. 116-122 (1949).

14. P. A. Redhead, "The Townsend Discharge in a Coaxial Diode with Axial Magnetic Field," Candian Journal of Physics 36(3) (1958).

15. R. L. Jepsen, "magnetically Confined Cold-Cathode Gas Discharge at Low Pressures." J. Appl. Phys. Vol 32, 12 (1961).

16. J. C. Helmer, R. L. Jensen, "Electrical Characteristics of a Penning Discharge," Proceedings of the IRE 49, (1961).

17. W. J. Lange, "Microwave Measurement of Electron Density in a Penning Discharge," J. Vac. Sci. Technol. 7,1 (1968).

18. T. S. Chou, D. McCafferty, "Pumping Behavior of Sputter Ion Pumps," J. Vac. Sci. Technol. 18(3) 1981.

19. J. R. Young, "Pressure Dependence of the Axial Ion Current in a Penning Discharge," J. Vac. Sci. Technol. 5, 4, pp 102.

20. P. N. Baker, L. Laurenson, "Pumping Mechanisms for the Inert Gases in Diode Penning Pumps," J. Vac. Sci. Technol. Vol. 9, No. 1, pp 375.

21, T. Snouse, "Starting Mode Difference in Triode and Diado Sputter-Ion Pumps," J. Vac. Sci. Technol., Vol. 8, No. 1, pp 283.

22. L. D. Hall, "Electronic Ultra-High Vacuum Pumps," Rev. Sci. Instr., Vol. 29, No. 5, pp 367 (1958).

23. R. H. Lewis, A. S. Divatia, "Design and Operation of Evapor-Ion Pumps," Rev. Sci. Instr., Vol. 25, No. 12, pp 1193 (1954).

24. K. M. Welch, "New Developments in Spatter-Ion Pump Configurations," J. Vac. Sci. Technol. Vol. 13, No. 1, pp 498.

25. W. J. Lange, J. H. Singleton, D. P. Eriksen, "Calibration of Low Pressure Penning Discharge Type Gauges," J. Vac. Sci. Technol., Vol. 3, No. 6, pp 338.

26. W. D. Davis, "Ultrohigh Vacuum Gauge Calibration, " J. Vac. Sci. Technol. Vol. 5, No. 1, p. 23.

27. J. P. Hobson, "Cryopumping," J. Vac. Sci. Technol., Vol. 10, No. 1, p. 73.

END

FILMED

DTIC